Hélio Fernandes Luis

Mestre

Study of nuclear reactions relevant for Astrophysics by Micro-AMS

Dissertação para obtenção do Grau de Doutor em Física

Orientador: Adelaide Pedro Jesus, Professora catedrática, FCT/UNL

Júri:

Presidente: Dr. Maria Paula Pires dos Santos Diogo

Arguentes: Dr. Rui Coelho Silva
Dr. Orlando Teodoro

Vogais: Dr. João Cruz
Dr. Daniel Redondo
Dr. Eduardo Alves

FACULDADE DE CIÊNCIAS E TECNOLOGIA
UNIVERSIDADE NOVA DE LISBOA

Study of nuclear reactions relevant for Astrophysics by Micro-AMS

Acknowledgements

I would like to thank Prof. Dr. Adelaide Jesus for the orientation of this thesis's work. I would also like to thank Dr. Soey Sie, Dr. Nuno Franco, Eng. Jorge Rocha, Dr. Eduardo Alves, Dr. Micaela Fonseca, Dr. João Cruz, Dr. Orlando Teodoro, Me. Cátia Santos, Me. Hugo Santos, Dr. Rui Coelho, Dr. Daniel Redondo, Eng. Paulo Velho, Dr. Carlos Cruz, , Me. Joana Lancastre and Me. Catarina Ramos for all the help they provided.

I would also like to thank Vanessa and all family and friends for their support.

Resumo

Esta tese tem como base a aplicação da técnica de Micro-AMS (Espectrometria de massa com acelerador usando micro-feixe) ao estudo de reações nucleares relevantes para a Astrofísica, nomeadamente através do estudo de reações envolvendo o radioisótopo ^{36}Cl.

A etapa inicial do trabalho prendeu-se com a instalação, teste e otimização do sistema de Micro-AMS que se encontra no laboratório de feixe de iões do CTN-IST. Na fase de testes foram medidos vários isótopos, nomeadamente isótopos de chumbo e platina, que revelaram o potencial desta técnica para aplicações em áreas tão diversas como a Ciência dos Materiais ou a Arqueologia. Após esta fase, deu-se o inicio do trabalho com o ^{36}Cl.

O radioisótopo ^{36}Cl é um dos isótopos de tempo de vida média curta (assim chamados por a sua vida média ser curta quando comparada com a idade da terra) cujas abundâncias no sistema solar primitivo poderão ajudar a esclarecer o seu processo de formação. Existem dois modelos geralmente aceites para a produção deste radionuclido; é originário de ejecta de supernovas vizinhas (onde o ^{36}Cl foi provavelmente produzido no processo *s* através da irradiação neutrónica de ^{35}Cl) e/ou foi produzido através da irradiação in-situ de pó nebular por partículas energéticas (principalmente p, a, ^{3}He - modelo de irradiação X-Wind).

O objectivo do presente trabalho foi a medição da secção eficaz da reação nuclear ^{35}Cl(n,γ)^{36}Cl, que abriu a possibilidade da medição futura das secções eficazes das reações nucleares ^{37}Cl(p,d)^{36}Cl e^{35}Cl(d,p)^{36}Cl. Esta medição foi efectuada através da determinação da quantidade de ^{36}Cl em amostras de AgCl, utilizando a referida técnica e tirando partido da sua alta sensibilidade para medições de cloro. Para tal, o sistema de Micro-AMS do CTN-IST teve que ser optimizado para medições de cloro uma vez que esta é a primeira vez que este tipo de medições foi executada (AMS com micro-feixe).

Esta tese apresenta os resultados destes desenvolvimentos que foram feitos comparando amostras de AgCl irradiadas no Reactor Nacional Português com amostras padrão produzidas através da diluição do material de referência NIST SRM 4943. Após a obtenção destes resultados, a secção eficaz da reacção ^{35}Cl(n,γ)^{36}Cl foi calculada.

Palavras-chave: Micro-AMS, ^{36}Cl, secção eficaz, reação nuclear, Astrofísica, formação do sistema solar, isótopos de tempo de vida média curta

Abstract

This work of this thesis was dedicated to the application of the Micro-AMS (Accelerator Mass spectrometry with micro-beam) to the study of nuclear reactions relevant to Astrophysics, namely reactions involving the radioisotope ^{36}Cl.

Before this could be done, the system had to be installed, tested and optimized. During the installation and testing phase, several isotopes were measured, principally lead and platinum isotopes, which served to show the potential of this technique for applications to Material science and archeology. After this initial stage, the work with ^{36}Cl began.

^{36}Cl is one of several short to medium lived isotopes (as compared to the earth age) whose abundances in the earlier solar system may help to clarify its formation process. There are two generally accepted possible models for the production of this radionuclide: it originated from the ejecta of a nearby supernova (where ^{36}Cl was most probably produced via the s-process by neutron irradiation of ^{35}Cl) and/or it was produced by in-situ irradiation of nebular dust by energetic particles (mostly, p, a, ^{3}He -X-wind irradiation model).

The objective of the present work was to measure the cross section of the ^{35}Cl(n,γ)^{36}Cl nuclear reaction which opened the possibility to the future study of the ^{37}Cl(p,d)^{36}Cl and ^{35}Cl(d,p)^{36}Cl nuclear reactions, by measuring the ^{36}Cl content of AgCl samples with Micro-AMS, taking advantage of the very low detection limits of this technique for chlorine measurements.

For that, the micro-AMS system of the CTN-IST laboratory had to be optimized for chlorine measurements, as to our knowledge this type of measurements had never been performed in such a system (AMS with micro-beam).

This thesis presents the results of these developments, namely the tests in terms of precision and reproducibility that were done by comparing AgCl blanks irradiated at the Portuguese National Reactor with standards produced by the dilution of the NIST SRM 4943 standard material. With these results the cross section of the ^{37}Cl(n,γ)^{36}Cl was calculated.

Keywords: Micro-AMS, ^{36}Cl, cross section, nuclear reaction, Astrophysics, solar system formation, short lived radionuclides

List of symbols

A	activity
B	magnetic field
C	capacitance
c	velocity of light
$c(A)$	fractional concentration of element A
d	distance
E	energy
$\vec{E}$	electrostatic field
f	frequency
$\vec{F}$	centripetal force
h	amount of target material
g_w	wescott factor
G	gravitational constant
G_{res}	self-protection factor
L	length
M	mass
m	mass
N	number of nuclides
N_A	Avogadro constant
$n(A)$	concentration of element A
n_{tot}	number of atoms
P	attenuation factor
q	charge
r	radius
S	linear stopping power
$S_{A,B}$	separation factor
$S_{1,M}$	sputter rate
t	time

t_{irr}	irradiation time
U_0	amplitude of AC signal
U	surface binding energy
v	velocity
V	voltage
Z	Atomic number
ξ	electrostatic field
φ	angle
$\alpha^q(P)$	Probability for ionization
ϕ	neutron flux
σ	cross-section
θ_X	Natural abundance of isotope X
σ_i	Individual uncertainty
ϕ_R	real neutron flux
Y	yield
Y_{tot}	total sputtering yield
ω	angular frequency
$r(A^N)$	relative abundance of isotope A^N
n_{tot}	number of target $atoms/cm^3$
I	electrical current
$I^q(P)$	secondary current of a molecule $P=A^N B_j^M C_k$
$I^q(A^N)$	current of isotope A^N in charge state q
I_g	branching ratio

I_R	isotopic ratio
$T_{HE}{}^{q}(A^N)$	transmission of A^N in charge state q through the HE spectometer
$T_{LE}^{-}(P)$	transmission of P through LE mass spectometer
T	half life
ε	detector efficiency
$RSF_M^{T^N}$	relative sensitivity factor
Ω_T	electron affinity
λ	decay constant

Table of Contents

List of Figures

List of Tables

1

Introduction

The work developed in this thesis started not much time after the arrival of the Australis Micro-AMS system at the then-called LFI at ITN (Laboratório de Feixe de Iões do Instituto Tecnológico e Nuclear) and now called LATR (Laboratório de Aceleradores e Tecnologias de radiação) at CTN-IST (Campus Tecnológico e Nuclear do Instituto Superior Técnico) in 2007. The Australis Micro-AMS system was developed by Dr. Soey Sie in the 1990's at one of CSIRO laboratories in Sydney, Australia. Dr. Soey Sie developed the system with the goal of using it mainly for geological applications, since the CSIRO laboratory has a tradition of geological research.

The Micro-AMS system at CTN-IST is basically a SIMS (Secondary Ion Mass Spectrometry) system connected to an AMS (Accelerator Mass Spectrometry) system. It was developed to permit the spatial analysis of samples with a highly focused cesium primary beam, as is often done in the SIMS technique, while using an accelerator, as in AMS, to resolve molecular and isobaric interferences that in some cases hinder SIMS detection limits. The history and principles of this technique will be developed in the following chapter.

The main goal of the thesis proposal was to apply the Micro-AMS technique to Nuclear Astrophysics. However, this was not immediately possible, as the system didn't perform as expected in the initial stage of the work. It had to be aligned and updated in order for it to be possible to achieve its previous benchmarks. This process was an important part of the developed work in terms of time consumption, and will be described in chapter 3,

especially in terms of the detailed description of the system. This initial stage permitted the development of skills and knowledge that were fundamental for the operation of such a big and complex system, for which there was no previous experience in the laboratory or the country. This time-prolonged learning curve caused some deviation from the main field of research as, for instance, many of the samples readily available in the testing phase permitted measurements that were useful in other fields of research. These samples came from CSIRO and had already been tested there. This made them ideal for the development and installation of the system as the testing results obtained in Lisbon could be compared with the results previously obtained in Sydney for the same samples. Some of the applications that derived from these initial measurements will be shown in chapter 5. This initial long stage explains why the Astrophysical theme of this work is only approached in the final chapter of the thesis. In the end, and because of the initial limitations of the system and of the know-how available in the laboratory, the unifying theme of this thesis is the development of the Micro-AMS system as much as it is its Astrophysical content.

The work shown in the final chapter of this thesis is related to early solar system Astrophysics, and the role of ^{36}Cl in the development of the present day knowledge about the solar system's early stages of formation. ^{36}Cl is one of several short to medium lived isotopes (as compared to the earth age) whose abundances at the earlier solar system may help to clarify its formation process. There are two generally accepted possible models for the production of this radionuclide: it originated from the ejecta of a nearby supernova (where ^{36}Cl was most probably produced in the s-process by neutron irradiation of ^{35}Cl) and/or it was produced by in-situ irradiation of nebular dust by energetic particles (mostly, p, a, ^{3}He -X-wind irradiation model). Which model explains better the origin of ^{36}Cl is still a matter of debate and research.

The objective of the work presented in the chapter 6 was to measure the cross section of the ^{35}Cl(n,γ)^{36}Cl nuclear reaction which opened the possibility to the future study of the ^{37}Cl(p,d)^{36}Cl and ^{35}Cl(d,p)^{36}Cl nuclear reactions, by measuring the ^{36}Cl content of AgCl samples, taking advantage of the very low detection limits of the Micro-AMS technique for chlorine measurements.

This goal required the adaptation of the technique to the specific requirements of chlorine AMS measurements and these developments are also described.

2

Introduction to the technique

2.1 SIMS, AMS and Micro-AMS

The micro-AMS technique is a combination of two previously existent techniques; Secondary Ion Mass Spectrometry (SIMS) and Accelerator Mass Spectrometry (AMS). The technique implemented at Sacavém is more commonly called Accelerator Secondary Ion Mass Spectrometry (ASIMS), Microbeam AMS or simply Micro-AMS as it will be called in this dissertation. It was developed with the goal of combining some of the advantages of the two techniques. In fact, most of the Micro-AMS systems around the world are just a SIMS chamber and sputter source connected to an AMS line. First then we must understand these two techniques in order to better understand the Micro-AMS technique.

2.1.1 Secondary Ion Mass spectrometry (SIMS)

2.1.1.1 History of SIMS

The first experiments in what was to be called SIMS were developed by Herzog and Viehbock in 1949 in the University of Vienna [1], where they developed the first electron impact primary ion source, which cannot be yet considered a SIMS system in the sense we employ it today. The first complete secondary ion mass spectrometers, were only developed 10 years later by Bradley, Beske, Honig and Werner [2].

In the early 1960's NASA financed the development of a SIMS instrument by Liebel and Herzog with the goal of analyzing moon rocks [3]. Also around this time, in the University of Paris-Sud in Orsay, a SIMS system was developed by Castaing [4]. Both these instruments used argon as primary beam ions and were based on a magnetic double focusing sector field mass spectrometer. In the following decade, K. Wittmack and Magee would introduce SIMS with quadropole mass analyzers [5] and Beenighoven would develop static SIMS [6]. In the following decades, numerous developments resulted in SIMS becoming a widespread technique with numerous facilities around the world [7].

2.1.1.2 SIMS principle

SIMS is usually divided into two kinds; static SIMS and dynamic SIMS. Both kinds use a primary beam to sputter the sample and analyze it. In the case of static SIMS the goal is to analyze the surface of the sample and so low beam currents have to be used (< 5 nAcm^{-2}) in order to keep the integrity of the surface for periods longer than analysis time.

In the case of dynamic SIMS much higher primary currents are used allowing the removal of several surface layers and thus enabling depth profiling. This higher primary beam intensity allows also for much higher sensitivities.

In many SIMS systems around the world, a primary beam of negative oxygen ions or a positive beam of cesium ions is accelerated onto a sample sputtering its surface. Of all the particles that are separated from the surface by sputtering, a part of these will be ionized. The negatively ionized particles (in the case of the cesium primary beam) or the positively ionized particles (in the case of the primary oxygen beam) constitute what is called the secondary beam. These elements are most commonly used as primary beams, because oxygen enhances the positive secondary beam yield for electropositive elements and cesium does the same for electronegative elements producing a higher yield for negative secondary beams. Nevertheless other elements such as argon are sometimes used as primary beams.

The secondary beam will be accelerated (usually to energies ranging from 1 keV to 10 keV) and passed through one or several electrostatic analyzers followed by a magnet that will separate the different masses present in the beam. These separated masses can then be quantified in a detector.

The electrostatic analyzer uses a radial electrostatic field ξ of constant magnitude along an arc of radius r, that deflects ions along a circular path defined by:

$$2\frac{E}{q} = \xi r$$

In the magnet, the radius of curvature r of the path of each ion traveling in a trajectory normal to a magnetic field B depends on its mass m, energy E and charge state q;

$$2\frac{m}{q}\frac{E}{q} = (Br)^2$$

By this process it is possible to analyze the constitution of the surface of the sample in various points (the primary beam can usually be focused to very small diameters, in some cases a few microns) and even do depth analysis,

because the primary beam will erode the sample layer by layer. This depth analysis is called depth profiling and is one of the main applications of the SIMS technique.

The analysis of the sample surface allows the detection of trace elements of very low concentrations in a given matrix, down to the part per billion range in some cases. The sensitivity of this technique is different for different trace elements and matrices, and can vary widely, being heavily dependent on the trace element and the matrix itself, and of course also on the characteristics of the particular SIMS system.

Despite the existence of sequential selectors of the two types described above (electrostatic and magnetic), several unwanted particles may reach the detector and limit the sensitivity of the SIMS technique. These unwanted particles can be related to mass interferences or to ions of different mass but with the same values of m/q and E/q of the ions of interest, or even with ions with different mass, energy or charge which end up following the same path to the detector as the ions of interest due to energy or charge changing collisions with residual gas or system components. The mass interferences are due to two different causes; first there can be an interference between different molecules that happen to have the same mass (e.g.:C_2H and BeO) or between a molecule and an ion with the same mass (e.g.:O_2 and ^{32}S), secondly there can be a so called isobaric interference (isobars are isotopes belonging to different elements but with the same mass; e.g.:^{10}Be and ^{10}B). The mass interference problem is usually minimized in SIMS by increasing the resolution of the mass spectrometer but only with limited success. It was partly with the intent of dealing with this problem that the AMS technique was developed.

2.1.2 Accelerator Mass Sprectrometry (AMS)

2.1.2.1 History of AMS

Mass spectrometry studies involving accelerating ions to the MeV energy range happened for the first time in 1939 at the Berkeley 88-inch cyclotron, when Alvarez and Cornog used it with the goal of detecting ^{3}He [3]. The technique was not yet called AMS. Only about thirty years later was the name used in a proposal for the study of ^{14}C dating done by Oeschger and his group in 1970. This was followed by an experimental attempt by Shnitzer and his collaborators in 1974. In 1977, Muller failed to find quarks while measuring ^{3}H in water with the same cyclotron as used by Alvarez in Berkeley. By 1977, the now historic paper by Muller et al. suggested that ^{14}C and ^{10}Be could be measured using a particle accelerator [9]. This sparked a wave of interest in AMS since radiocarbon studies had by then become widespread, and the AMS method could reduce sample size and measurement time enormously when compared to the traditional radioactive decay counting, as well as improving its sensitivity by several orders of magnitude (nowadays a standard radiocarbon measurement can achieve a $^{14}C/^{12}C = 10^{-14}$ sensitivity easily using very small samples (~1 mg) and with only few minutes of measurement time, with a precision of ~1%). The experimental realization of the possibility advanced by Muller came to fruition in 1977 by two groups working independently, one group in McMaster University led by Bennet [10] and one group in Rochester University led by Nelson [11]. Both groups used electrostatic accelerators instead of cyclotrons. Following these successes the technique started to spread and develop quickly with major contributions by Raisbeck and his coworkers using the Grenoble cyclotron (with the measurement of ^{10}Be in samples of Antarctic ice in 1978 [12] and the measurement of ^{26}Al in 1983 [13]), and Elmore and coworkers that developed ^{36}Cl AMS in 1979 with the purpose of analyzing its presence in environmental water samples [14] and ^{129}I AMS in 1980 at Purdue University [15]. Adding to these initial radioisotopes, other isotopes followed like ^{32}Si, ^{39}Ar, ^{59}Ni, ^{81}Kr, ^{236}U and ^{239}Pu.

Nowadays most AMS applications are related to long-lived cosmogenic radionuclides (usually with half-lives between 10^3 years and 10^7 years). These

are produced by cosmic rays and can be used as tracers and chronometers in geoscience, cosmic ray physics, archeology and environmental studies. AMS is especially suited for long lived cosmogenic radionuclides since it does not depend on the half-life or decay mode of the radioisotope. Other applications involve stable isotopes, artificial radioisotopes studies (produced with nuclear reactors or particle accelerators) and search for exotic particles in nature and the study of rare decay processes in geological samples.

2.1.2.2 AMS principle

It is important to describe with some detail the principles behind the AMS technique, since after the target chamber, which resembles a normal SIMS target chamber, all the rest of the LATR/CTN-ITN Micro-AMS system is identical to an ordinary 3MV AMS system.

AMS is a mass spectrometry technique that, as the name indicates, uses a particle accelerator. With an accelerator, the mass interferences that limit SIMS detection limits in some isotope studies can be resolved, and the detection limits for these isotopes drop by several orders of magnitude. This is true only for a few isotopes, mostly radioisotopes; the reason for this will be explained later.

In a conventional AMS system, the target chamber and primary ion source configuration are designed so as to maximize the secondary beam current. After this beam is analyzed in the electrostatic analyzer and magnetic analyzer like in SIMS, the mass channel where interferences are known to exist is injected into the accelerator, where all the negatively charged particles will be accelerated towards the positive terminal voltage applied at the center of the accelerator tube.

At the center of the accelerator these particles will collide against a gas medium (argon or other) or a very thin foil of carbon, called the stripper gas or foil. A significant part of the ions involved in the interaction with the stripper will lose electrons in their outer shells and thereby change polarity from negative to positive. If any of these particles are molecules, these will mostly

disintegrate. This means that after the stripper channel there will be no more molecular interferences. The now positive ions will again be accelerated towards the exit side of the accelerator. At the very high energies that these particles reach, a special detector can be used to resolve any isobaric interference if it exists. This can lead to cases where detection limits fall to 10^{-15} [16].

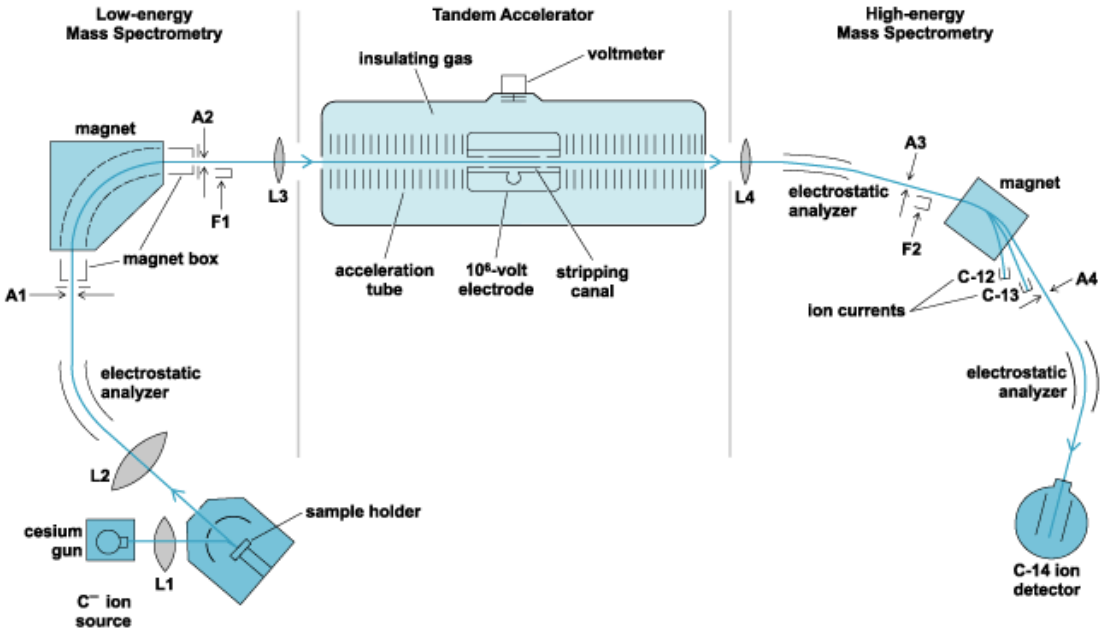

Figure 2.1: General scheme of a standard AMS beam line, using the example of ^{14}C. F means Faraday cup. A means slits. L means focusing device.

These are the reasons that led to the creation of the AMS technique. Of course, this demands a usually very big vacuum line with a lot of sophisticated elements besides the very big and complex tandem accelerator.

A standard AMS line will usually be composed of a target chamber and ion source, an electrostatic analyzer and a magnet at the low-energy side of the accelerator, and again a magnet, an electrostatic analyzer and a detector chamber at the high-energy side of the accelerator. Figure 2.1 shows a scheme

of a usual AMS line with all the components shown.

All the elements necessary for a standard AMS line will be explained in the following pages, starting in the target chamber and ending in the detector chamber.

2.1.2.2.1 Primary and secondary beams

As was mentioned, the principle of AMS consists in sputtering a sample with a primary cesium beam, thus extracting the particles from its surface, as in SIMS, and forming a negative secondary ion beam. Since in AMS the main goal is to achieve very high sensitivities, the design of the configuration of the target chamber and sputter source is done to maximize the current of the secondary beam of the isotopes being studied. This means having large diameter primary beams and targets that are chemically treated so as to maximize the sputtering yield for the desired isotopes. This means losing the ability to analyze spatially and in depth the original matrix, because the beam is too large on the one hand and the matrix is not the original one anymore.

The fact that the secondary ion beams extracted from the sample are negative is a limiting factor in the AMS technique, in terms of the number of isotopes that can be measured with tandem accelerator based AMS, because negative ions of noble gases and of a few other elements such as N, Mg, Mn, Zn, Cd or Hg, are too unstable to reach the terminal of the accelerator, disintegrating before reaching it. This can be advantageous in some cases, as in the case of radiocarbon dating, where the interfering ion $^{14}N^-$, which has the same mass as the measured radioisotope ^{14}C, will not reach the accelerator terminal. This is true as well in the case of ^{26}Al AMS which has the interfering stable $^{26}Mg^-$ ion, and in the case of the stable isobar $^{129}Xe^-$ in the studies involving the radioisotope ^{129}I. This means that in these isotopic studies AMS measurements can be performed with relatively small tandems, of 3MV terminal voltage or even less [17] (the demand for higher energies in some isotopic studies in AMS are related to isobaric interferences present in those analysis, especially for higher masses).

The limitation of AMS to electronegative elements can be surpassed in some cases if there is a prolific molecular negative ion that can be injected instead of the electropositive atomic ion. This technique is also used in cases where elemental ion currents are too weak, as is the case of Be, Ca, Sr or Ba where hydrides or other molecular compounds that include these elements can be used. In these cases, oxides or other molecular negative forms including these elements are injected into the accelerator instead of the elemental ions.

The reason for using only cesium primary ion sources and therefore negative secondary ion beams and not oxygen primary beams as well (which could produce positive secondary beams and open the possibility for a lot more elements to be studied with AMS) is that the tandem accelerator terminal voltage is positive, and so it can only accelerate negative ions at its entrance channel.

2.1.2.2.2 Low-energy beam transport system

As mentioned before, the fraction of the extracted particles from the sample that are in a negative ionization state (most of the sputtered particles will be neutrals) is accelerated by a negative potential applied to the target, forming the secondary beam. This beam passes through an electrostatic analyzer and then through a magnet just like in the SIMS technique, but after the magnet the beam is injected into an accelerator.

In order to achieve high precision measurements of isotopic ratios (results in AMS are usually presented in the form of isotopic ratio of trace element concentration to a specific abundant matrix element concentration; usually of a stable isotope of the same element of the trace isotope, e.g.:$^{10}Be/^{9}Be$, $^{14}C/^{12}C$, $^{26}Al/^{27}Al$, $^{36}Cl/^{35}Cl$) the beams of the different isotopes are injected simultaneously or in rapid sequence, so that they reach the detection system simultaneously in the first case or almost simultaneously in the second. This is important because beam instabilities in time due to the source, beam transport system and accelerator terminal voltage variations can affect the precision of the measurements.

2.1.2.2.3 Tandem accelerator

Once inside the accelerator the beam will be stripped and accelerated to higher energies. The stripping process consists of using a gas or foil to strip the outer electrons of the ions passing through it, thus changing their charge state from negative to positive. This process will also break up all the molecules in the beam (since stable molecules very rarely survive a charge state higher than 2+ [18]), producing a high-energy beam that will consist only of monatomic ions thus eliminating practically all molecular interferences.

Negative ions will enter the accelerator with energy $E_i = e.V_i$, where V_i is the total injection voltage and e the total charge of the ion. In the accelerator, they will be accelerated towards the high-voltage terminal (that is usually at voltages that can range anywhere from +500 kV to +20 MV, depending on the system and type of analysis being performed) where the stripping channel or foil are situated. Once in the stripping channel, their polarity will become positive and they will be accelerated towards the high-energy side of the accelerator. Their final energy E_f will be:

$$E_f = E_i + (q + 1).e.V_t$$

where V_t is the terminal voltage of the accelerator and q the positive charge state that a particular ion achieves in the stripping channel. The chosen terminal voltage will depend on the kind of isotope being measured, and whether or not there is an interfering stable isotope.

Even though tandem accelerators are by far the most used in AMS in laboratories around the world, several others can be used, such as Van der Graff accelerators, cyclotrons or linear accelerators.

2.1.2.2.4 High-energy beam transport system

After the accelerator, there will be a high-energy beam with monatomic ions in different charge states. This beam will be again passed through a mass spectrometer and one or more electrostatic analyzers ending in a detector chamber where the beam will be analyzed and measured. The combination of electrostatic analyzers and magnet will allow for the selection of a particular mass and charge-state/energy so as to minimize ambiguities in particle identification in the detector. The more basic AMS systems will have for this effect an ESA (electrostatic analyzer) after the accelerator, as well as one before the accelerator. They are usually called LE ESA (low-energy ESA) and HE ESA (high-energy ESA).

The ESA's will act as energy separators. Having a mono-energetic beam reaching the detector chamber is crucial because different charge state and different masses can have the same magnetic rigidity.

In more sophisticated AMS systems there can be, besides the ESA´s, wien-filters that will act as velocity selectors and gas filled magnets where isobaric separation can be achieved.

2.1.2.2.5 Particle identification

At the very high-energies (in some cases several tenths or even hundreds of MeVs) that the beams reach the detection chamber, it is possible to use special detectors, like gas ionization chamber, gas-filled magnets or Time Of Flight detectors to resolve isobaric interferences if they exist. Of these, the most commonly used, when there are isobaric interferences, are the ionization chamber type detectors. These are usually called E, ΔE detectors and will be explained in detail in chapter 3.

The high-energies available to AMS systems are also useful in improving the backgrounds of the detectors used, because at these high energies the cross sections of scattering processes off residual gas atoms are smaller.

2.1.2.2.6 Detection limits and other limitations

Using these techniques the detection limits for certain trace elements drop by several orders of magnitude (when compared to SIMS detection limits); in some cases 10^{-15} relative concentration of trace element to matrix. This kind of sensitivity makes the technique applicable mostly to radioisotope studies, since at this kind of element concentrations, contaminations in the primary beam, residual gas of the system and in the electrodes around the sample make stable isotope study almost impossible. Table 2.1 shows the detection limits of the new 6 MV AMS system at Helmholtz-Zentrum Dresden-Rossendorf, Dresden for several radioisotopes.

This limits the number of applications of AMS greatly. Because of these limitations, AMS development through the years evolved to a stage where the great majority of AMS based research around the world is focused on a small number of radioisotopes, namely ^{10}Be, ^{14}C, ^{26}Al, ^{36}Cl, ^{41}Ca, ^{55}Fe and ^{129}I. These constitute more than 90% of all AMS research. Nevertheless many other isotopes have been and are being studied like ^{2}H, ^{7}Be, ^{22,24}Na,^{32}Si, ^{53}Mn, ^{59}Ni, ^{60}Fe, ^{138}Ba, ^{205}Pb, ^{244}Pu, amongst others.

Even if few in number, AMS measurement of these isotopes provides important and many times groundbreaking work in a large number of different scientific research fields, such as archeology, where radiocarbon dating was fundamental, biomedicine, advanced material science, industrial science, geology, atomic, nuclear and particle physics, as well as astrophysics, astronomy and others.

Another important limitation of this technique is its complexity and cost, involving sometimes very big accelerators and beam transport systems that require large teams for operation and maintenance. In recent years, some very small AMS systems were developed, based around 500 kV accelerators, that, although limited in the range of applications because of the small available energy, are much simpler to operate and its acquisition and running costs are much lower than traditional AMS systems.

Rare nuclide	Injected ion	Injected current (μA)	Terminal voltage (MV)	Charge state after stripping	Charge state after absorber	Total transmission (%)[a]	Background	Precisionat isotope ratio
^{10}Be	BeO^-	2–7	4.5	2+	4+	21	4.5×10^{-16}	0.3% at 10^{-12}
^{14}C	C^-	30–45	3.0	3+	–	40	1.2×10^{-15}	0.4% at 10^{-12}
^{26}Al	Al^-	0.2–0.5	2.7	3+	–	35	8×10^{-16}	1.5% at 10^{-11}
	AlO^-	3–6	6.0	4+	8+	~2	1×10^{-14}	~2% at 10^{-11}
^{36}Cl	Cl^-	20–30	6.0	5+	11+	3	3×10^{-15} ($^{36}Cl/^{35}Cl$)	2.0% at 10^{-12}
^{41}Ca	CaF_3^-	0.2–0.35	5.8	4+	–	16	8×10^{-15}	2.5% at 10^{-11}
^{129}I	I^-	3–5	5.0	5+	–	9	2×10^{-13}	1.2% at 10^{-11}

a Defined as the ratio between the number of ions detected in the ionisation chamber and the number of ions injected into the accelerator.

Table 2.1: Table with the performance for several radioisotopes at the new 6MV AMS system at Helmholtz-Zentrum Dresden-Rossendorf, Dresden. The elements shown are the most common radioisotopes measured in AMS. The stripper used is argon gas. The background column can be read as the detection limits for the measurement of an isotope, because the background of the detector for a certain mass will define that mass' detection limit. The charge state after absorber column shows the charge state the ions reach after passing the absorber foil put in front of the ionization chamber detector. This will severely decrease the current of the interfering isobar that enters the chamber [19].

2.1.2.2.7 Chemical preparation of samples

In order to achieve very low sensitivities the samples used in AMS must be chemically prepared so as to remove the trace element from the original sample and dissolve it in an appropriate matrix that maximizes the sputtering efficiency and minimizes known isobaric interferences [20]. This chemical

treatment also usually involves the addition of a certain amount of one or more stable isotopes (of the same element of the radioisotope element in study) in the cases where these stable isotopes are not already the matrix main elements. These stable isotopes of the same element of the trace radioisotope will be used as the pilot beam for the optical optimization of the beam through the various elements along the beam line, and will usually be used in the end to calculate the isotopic ratios. In order to obtain isotopic ratios with reasonable precision (<10%) standards are usually used. These are prepared by diluting a known concentration standard solution in a matrix identical to the samples in study. Blanks are also used in order to measure the background of the system. The chemical treatments of the samples are often complex and demand a dedicated chemical lab, and are one of the most cumbersome parts of the AMS process. Besides the complexity, the chemical treatment will invalidate any kind of spatial analysis or depth profiling since the matrix is not the original one anymore, since, as was mentioned before, the primary beam in AMS is usually optimized for sputtering efficiency alone, and its diameter and intensity are mush higher than in the case of SIMS.

2.1.3 Micro-AMS

2.1.3.1 Micro-AMS history

The idea of using AMS to study stable isotopes, a concept associated with accelerator SIMS, came about soon after AMS itself being patented by K. Purser in 1977 [21]. Soon after, Rucklidge and his group at the University of Toronto, modified an ion source with the goal of analyzing individual mineral grains with a cesium microbeam. Their results were published in 1982 [22].

In the 1980's, the rapid development of the semiconductor industries led to a development of ASIMS. A collaboration between Texas Instruments and the University of Arizona yielded the first measurements of trace elements in semiconductors, improving the detection limits of the SIMS technique by two orders of magnitude. After this initial success a new system was built specifically for the purpose of analyzing semiconductors.

In the following decade, more ASIMS systems were developed. In Munich's AMS facility, a SIMS source was added to the AMS system [23]. Around 1997, Sie developed Australis with the goal of analyzing geological samples with a microbeam [24]. This is the system now installed at the CTN-ITN laboratory.

2.1.3.2 Micro-AMS specificity

Micro-AMS evolved out of the necessity to combine some of the advantages of both of previously mentioned techniques; AMS and SIMS. On the one side, to be able to analyze spatially the original sample with little or no chemical treatment, and on the other side to be able to resolve the interferences that spoil the detection limits of the SIMS technique when mass interferences are present in a specific analysis.

The technique can sometimes be used for radioisotopic studies (just like in conventional AMS) where the loss in sensitivity can be compensated by the possibility of analyzing spatially and in depth the original matrix. On the other hand it can be used in stable isotope studies that demand spatial analysis and even depth profiling in studies where the gain in sensitivity (when compared to SIMS) justifies the added complexity and cost of running and maintaining the large facilities that Micro-AMS requires.

The loss in sensitivity is of course a consequence of the microbeam, the primary and secondary beams' currents are usually about 3 orders of magnitude lower than in conventional AMS and its detection limits are usually 3 orders of magnitude or more higher. Also, the fact that in most cases the matrix is the original matrix means that the sputtering yields are much lower than in the case of AMS where the matrix was built for that analysis and is made to maximize sputtering yield.

2.1.3.3 Micro-AMS comparison with other techniques

The comparison of Micro-AMS with other techniques has to have in mind the fact that Micro-AMS is limited to a negative secondary beam, which means that some elements are impossible to analyze. For the elements that it can analyze, it can bring several advantages in terms of sensitivity when compared to SIMS but also to other techniques. The next figure presents a simple comparison of Micro-AMS to several other techniques. This figure was taken from the dissertation of Dr. Collin Maden [25].

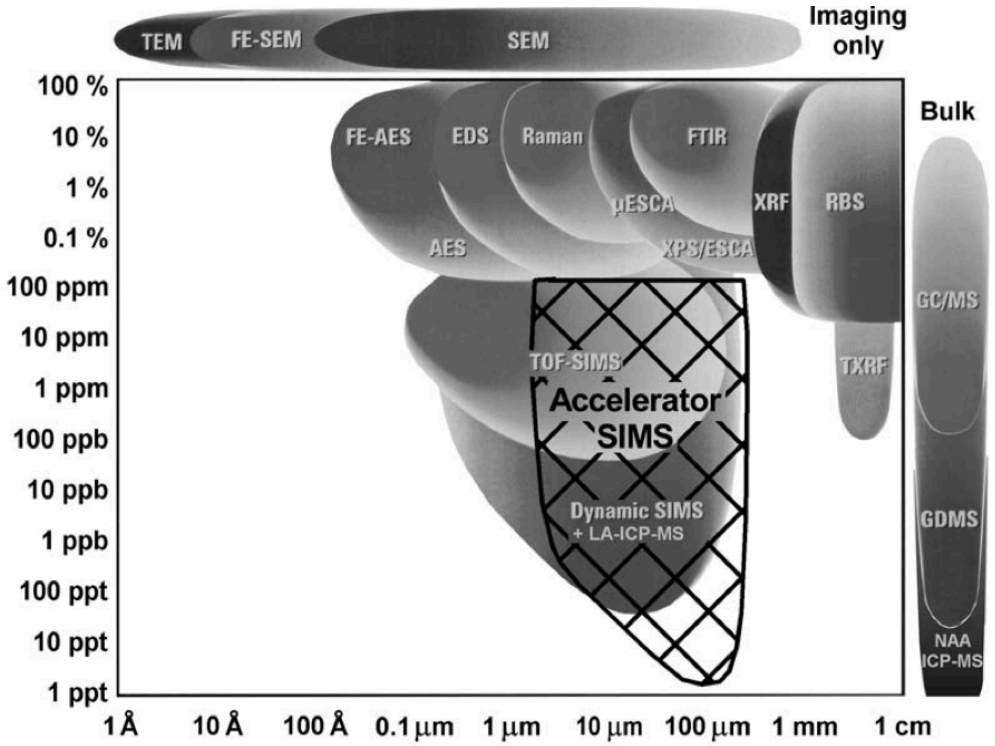

Figure 2.2: Atomic Force Microscopy (AFM), Scanning Electron Microscopy (SEM), Field Emission Scanning Electron Microscopy (FE-SEM), Transmission Electron Microscopy (TEM), Auger Electron Spectrometry (AES), Focussed Electron Beam Auger Electron Spectrometry (FE- AES), Energy Dispersive X-ray Spectrometry (EDS), µ-Raman Spectroscopy (Raman), X-Ray Photoelectron Spectroscopy (XPS), Electron Spectroscopy for Chemical Analysis (ESCA), Fourier Transform Infrared Spectrometry (FTIR), X-Ray Fluorescence (XRF), Rutherford Backscattering Spectrometry (RBS), Total Reflection X-Ray Fluorescence (TXRF), Time-of-Flight Secondary Ion Mass Spectrometry (TOF-SIMS), Secondary Ion Mass Spectrometry (Dynamic-SIMS), Inductively Coupled Plasma Mass Spectrometry (ICP-MS), Laser Ablation ICP-MS (LA-ICP-MS), Gas Chromatography/Mass Spectrometry (GCMS), Glow Discharge Mass Spectrometry (GDMS), Neutron Activation Analysis (NAA)

References

[1] Herzog, R. F. K., Viehboeck, F (1949). *Phys. Rev.* **76** (6): 855–856

[2] Honig, R. E. (1958). *J. Appl. Phys.* **29**: 549-555.

[3] Liebl, H. J (1967). *J. Appl. Phys.* **38** (13): 5277–5280

[4] Castaing, R. & Slodzian, G. J (1962). *Microscopie* **1**: 395–399.

[5] Magee, C. W. et al. (1978). *Rev. Scient. Instrum.* **49** (4): 477–485

[6] Benninghoven, A (1969). *Physica Status Solidi* **34** (2): K169–171.

[7] Honig, R. E. International Journal of Mass Spectrometry and Ion Processes Volume 66, Issue 1, 25 June 1985, Pages 31–54

[8] Alvarez L.W., Cornog R. Phys. Rev. 56, 613–613 (1939)

[9] Muller, R. A. (1977). Science **196** (4289): 489–494.

[10] Bennett C L, Beukens R P, Clover M R, Gove H E, Liebert R B, Litherland A E, Purser K H and Sondheim W E 1977

[11] Nelson D E, Korteling R G and Stott W R, 1977 Science 198 507

[12] Raisbeck, G. M.; Yiou; [et al.] Nature 1978

[13] Raisbeck, G. M.; Yiou, F.; Klein, J.; [et al.] Nature (1983)

[14] Elmore, D.; Fulton, B. R.; Clover, M. R.; Marsden, J. R.; Gove, H. E. Nature, Volume 277, Issue 5691, pp. 22-25 (1979).

[15] D. Elmore, H. E. GOVE et al. *Nature* 286, 138 - 140 (1980)

[16] Hotchkisa M. et al, Applied Radiation and Isotopes Volume 53, Issues 1–2, 15 July 2000, Pages 31–37

[17] Synal H.A. et al Nuclear Instruments and Methods in Physics Research Section B: Beam Interactions with Materials and Atoms Volume 259, Issue 1, June 2007, Pages 7–13

[18] Litherland A.E., Annual Review of Nuclear and Particle Science Vol. 30: 437-473 (December 1980)

[19] Akhmadaliev et al. ,Nuclear Instruments and Methods in Physics Research Section B 294 (2013) 5–10

[20] Hajdasa et al. , Nuclear Instruments and Methods in Physics Research Section B: Beam Interactions with Materials and Atoms, Volumes 223–224, August 2004, Pages 267–271

[21] Purser, K.H., 1977. U.S. Patent 4037100.

[22] Rucklidge, J.C., M.P. Gorton, G.C. Wilson, L.R. Kilius, A.E. Litherland, D. Elmore, and H.E. Gove, 1982. Canadian Mineralogist 20: 111-119.

[23] Matteson, S., J.L. Duggan, D. Marble, F.D. McDaniel, D.L. Weathers, D.K. Wilson, J.M. Anthony, and R.L. Beavers, 1990, Nucl. Instr. and Meth. B 52: 327-333.

[24] Sie, S. H.; Niklaus, T. R.; Suter, G. F. Nuclear Instruments and Methods in Physics Research Section B, v. 123, p. 112-121.

[25] Maden C., dissertation Swiss Federal Institute of Technnology, 2003

3

Experimental setup

3.1 The micro AMS system at CTN-ITN

In this chapter, the experimental setup of the micro AMS system at LATR/CTN-ITN will be explained with some detail, since the assemblage of the system was a central part of this thesis. Due to the system's complexity and large number of elements, the chapter was divided in several subchapters, concerning each section of the system, namely: the target chamber (3.1.1), the beam transport system (3.1.2), the accelerator (shown in figure 3.1) (3.1.3), the detector chamber (3.1.4), the bouncing system (3.1.5) and the computer control system (3.1.6). Each is in turn divided into its main constituents. Whenever

necessary, simplified drawings of the section being described will be shown, with numbers referring to each component. These numbers will be referred to in the text when the component in question is named.

The final subchapter refers to the assemblage work, and describes briefly the steps taken in the mounting of the system.

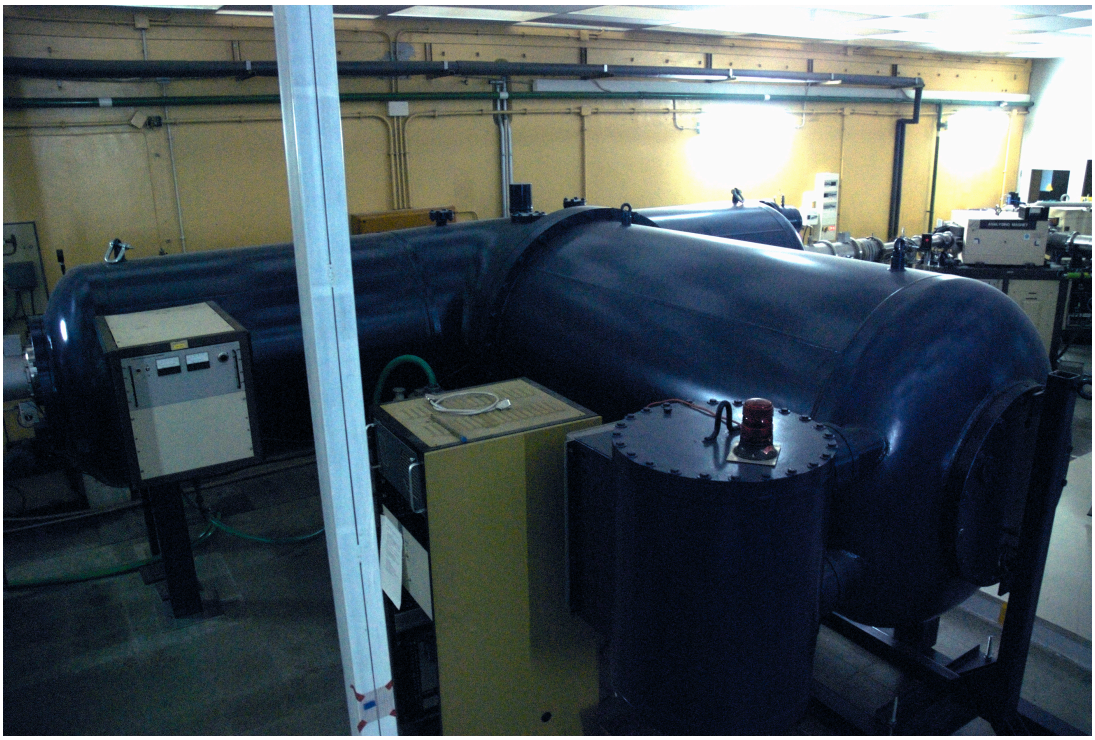

Figure 3.1: 3 MV tandem accelerator at LATR/CTN-ITN.

3.1.1 The target chamber

Figure 3.2 shows a photograph of the target chamber where its main parts are visible. The numbers seen in the photograph identify each main component:

(1) modified HICONEX ion source
(2) the extraction block and the target holder
(3) 3D sample stage
(4) target exchange vacuum lock

3.1.1.1 Ion source

The general Ionex Model 834 HICONEX cesium ion source was modified to allow for the production of a positively charged cesium microbeam.

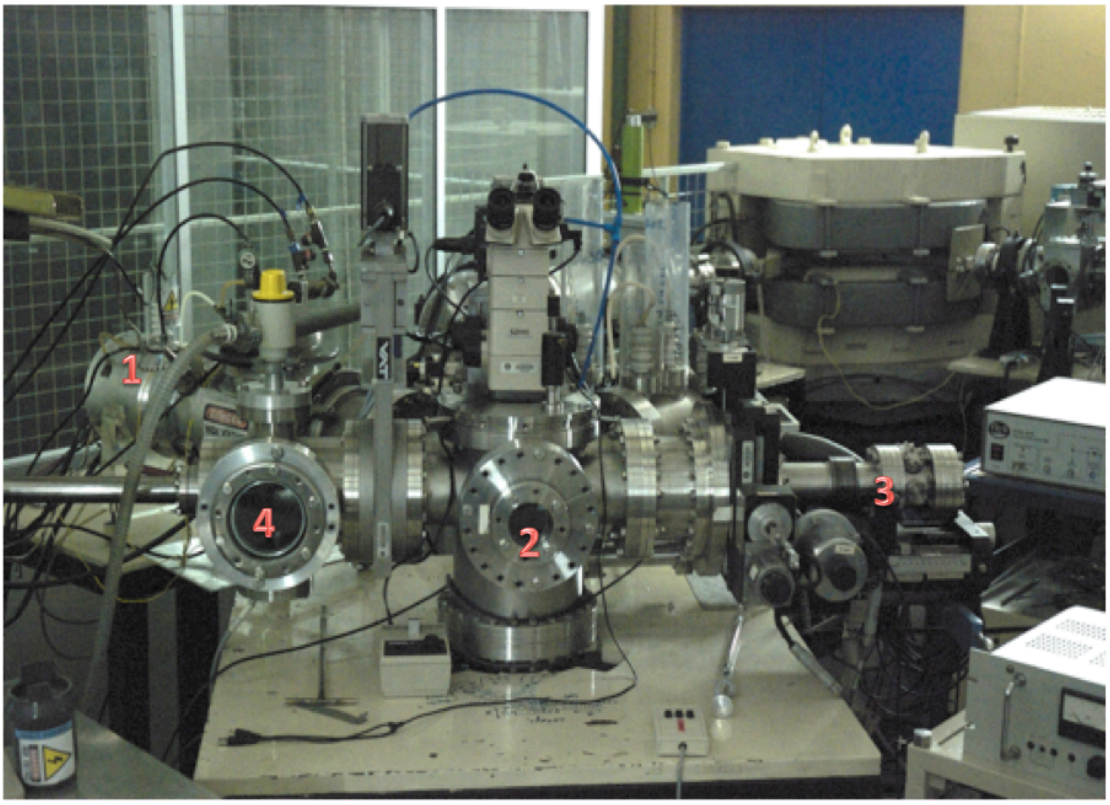

Figure 3.2: Micro-AMS chamber at LATR/CTN-ITN. In this image it is visible the ion source on the left side behind the vacuum lock system, the microscope on top of the chamber. The smaller circular glass window on the main chamber allows the operator to view the target holder.

In figure 3.3b a drawing of the ion source main components is shown, with numbers associated to each component.

The ion source works as follows. Metallic cesium is stored inside a reservoir (1). When heated, usually to slightly less than 220ºC, the cesium will evaporate onto

the ionizer tube (2) that can be heated up to 1100 ºC, where it will ionize. The positively ionized cesium will be injected into the extraction zone (3) that is polarized at around -5600 V. After this area there are four semi-cylindrical plates (each a 1/4 of a cylinder) that can be polarized up to 1000 V. These are called the focus lens (4). They can adjust the trajectory of the positively ionized cesium beam. In a normal Hiconex 834 source the cesium beam would, after the focus lens, hit the target, which would be mounted on a 12-position revolver (5) and polarized at -5 kV.

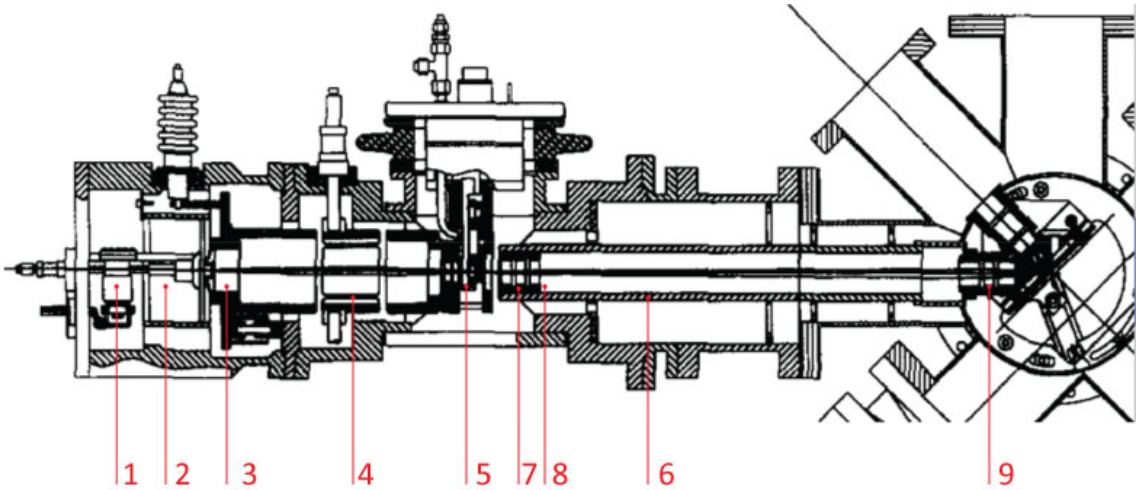

Figure 3.3: b) Scheme of the interior of the modified hiconex ion source.

This original target revolver was loaded with apertures of different diameters, in the place where the targets used to be, and after them a metal tube was installed. This tube (6) connects directly to the extraction block in the target chamber and is at the same -5 kV voltage as the revolver. Inside the tube are installed one einzel lens (7) and x and y deflector plates (8) that can be used to steer the beam, but are currently at -5 kV. At the end of this tube a primary einzel lens (9) allows further decrease in the diameter of the primary beam down to a minimum of 30 micrometers, if an aperture of 150 micrometers is

used. At this beam size, the primary beam intensity is about 16 nA, and 120 nA at 100 μm beam diameter, corresponding to a 1.6 mA/cm^2 [1].

3.1.1.2 Main chamber

In figure 3.4 a general scheme of the center of the target chamber is shown, where the target is located. The number is brackets in the following text refer to the numbers shown in this figure.

The ion source is connected to the main chamber also called target chamber, where the extractor block and the target holder are located. The extraction block is at -5 kV voltage potential and consists of three short cylinders, one that accommodates the primary einzel (1) lens and functions as a continuation of the focusing tube of the ion source, another one at 45º with the latter that functions as the secondary beam exit channel, and a third tube that accommodates the electron gun and is also at 45º with the secondary beam tube. The electron flood gun (2) is only used if the target samples are insulators. At the geometrical point where all the central axis of these tubes intersect, is the target itself (3). Before the beam hits the target it passes through the screen plate (4), polarized at a voltage usually between -4.5 kV to -5.5 kV, and the target plate (5), polarized at about -10 kV. This -10 kV voltage is also applied to the target itself and has the double function of accelerating the positive primary cesium beam towards it while also accelerating the negative secondary beam away from it. The screen plate (and also the target plate) is a plate with a hole in its middle where the beam passes through. Its main function is to screen the primary beam from the target area so that its trajectory is not affected by the secondary beam extraction. The voltage applied to the screen plate corrects the trajectory of the primary beam back to the geometrical center of the target area. After the secondary beam exits the secondary beam extraction tube in the extractor block, it is focused in the secondary einzel lens (6) at the very end of the target chamber.

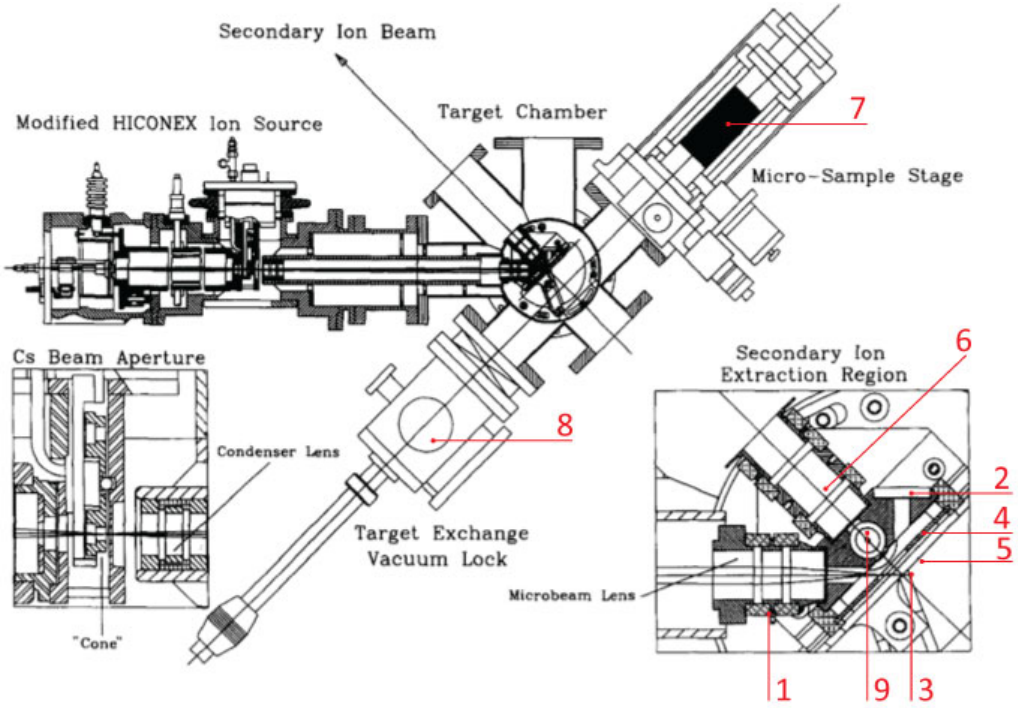

Figure 3.4: General scheme of the target chamber.

The target holder is supported in place by a rod that is connected to a Vacuum Generator OMNIAX 3 axis microstage (7), that allows for the sample holder to move in all three spatial dimensions in steps as small as half a micrometer. This of course is a very important feature because it allows the user to analyze the sample in the x and y directions and to analyze different spots of the target even if they are very near each other. Also connected to the target chamber is the vacuum lock system (8) that allows for the quick exchange of targets without a severe loss of the vacuum quality. With this system it is possible to recuperate the initial vacuum conditions after only about fifteen minutes of a target exchange. The target chamber is usually at a pressure of 3 $x10^{-7}$ mbar. When the ion source is operating the pressure in the target chamber rises to about 1 x 10^{-6} mbar.

A prism (9) is located in front of the target, at a 25 mm distance, in the secondary beam extraction tube. It is shaped in a way that its highly reflective surface is at a 45º angle with the beam axis. This prism reflects the image of the

target into an Olympus SZHIO zoom microscope with a 71 mm working distance situated outside and above the chamber, as can be seen in figure 3.2. Since the prism or mirror is located in front of the target, it was designed with a cylindrical aperture in its center so that the secondary beam can pass through it.

The microscope is connected to a camera that captures the image of the target in real time and sends it to the control computer. With a x10 ocular, a total maximum magnification of 70 is obtained. This is further magnified using a web camera, approximately by a factor of 2, resulting in a 1 μm pixel resolution on the computer screen.

The computer also controls all the different electrostatic focusing and deflecting devices in the chamber and along the beam line, besides the low and high-energy magnets. It also controls the bouncing system that will be described later, and the several faraday cups along the line as well as the detectors in the detector chamber. The control program was developed in Labview software. The control hardware consists of an OMRON PLC system and a few other devices that will also be described later.

3.1.2 The beam transport system

After exiting the target chamber, the particles of interest for the analysis (which are a part of the secondary beam exiting the target chamber) must be injected in to the accelerator and, after stripped and accelerated to high energies, taken to the detector chamber to be counted. This is done by a combination of two magnets and several electrostatic focusing and deflecting devices placed throughout the more than 30 m long vacuum line that constitute the beam transport system. The beam transport system is divided into the low energy (LE) side (sometimes called the injector system, as it injects the secondary beam into the accelerator) before the accelerator and the high-energy side (HE) after the accelerator. Figure 3.5 is a photograph showing the low-energy transport system. Figure 3.7 is a photograph of the high-energy transport system.

The LE and HE beam transport systems will be described, following the path of the beam from the target chamber to the detector chamber in the end of the system.

3.1.2.1 The Low-energy (LE) beam transport system or injection system

The LE beam transport system is shown in figure 3.5. In figure 3.6 a general scheme, showing all the main components of this part of the micro AMS system is shown. The numbers in brackets in the following text refer to the numbers shown in this figure.

Figure 3.5: General view of the injection system at LATR/CTN-ITN.

The injection system transports the beam from the target chamber (at the forefront of the image) to the accelerator (near the top right side in the image). It is composed of all the elements seen in this image except the target chamber itself. It is also called the low energy beam transport system because the beam's

energy before the accelerator is 10 keV, which is a low energy compared with the beam's energy after the accelerator.

As was described before, the secondary einzel lens focuses the secondary beam exiting the extractor block in the target chamber. This lens was specially dimensioned so that its image is located in the same point as the object of the LE ESA (low energy electrostatic analyzer). At this point there is the first set of slits and faraday cup (FC) (1). Using these slits and FC it is possible to optimize all the devices in the target chamber, before feeding the beam through the LE ESA. After this first set of slits there is another set (2) that reduces beam halo. When all the electrostatic devices in the target chamber are optimized, the first FC is lowered and the beam proceeds to the LE ESA (3).

The image of the LE ESA is the object of the LE magnet, and again at this point a set of slits and a retractable Faraday Cup (4) are located. All the FC's in the system are preceded by a set of four slits so this will not be mentioned again when indicating a FC. Between the LE ESA and this FC are a set of X and Y deflector plates (5). When the FC is retracted, the beam is mass analyzed in the LE magnet (6). The LE magnet is a double focusing 90º magnet corrected to the second order, with a 30 cm mean radius and 2.5 cm gap. By operating the ESA and the LE magnet with narrow slits, taking advantage of the low intensity secondary beams produced by the primary microbeam, a energy resolution ($E/\Delta E$) of 600 for the ESA and a mass resolution of 600 ($M/\Delta M$) for the magnet can be achieved [2].

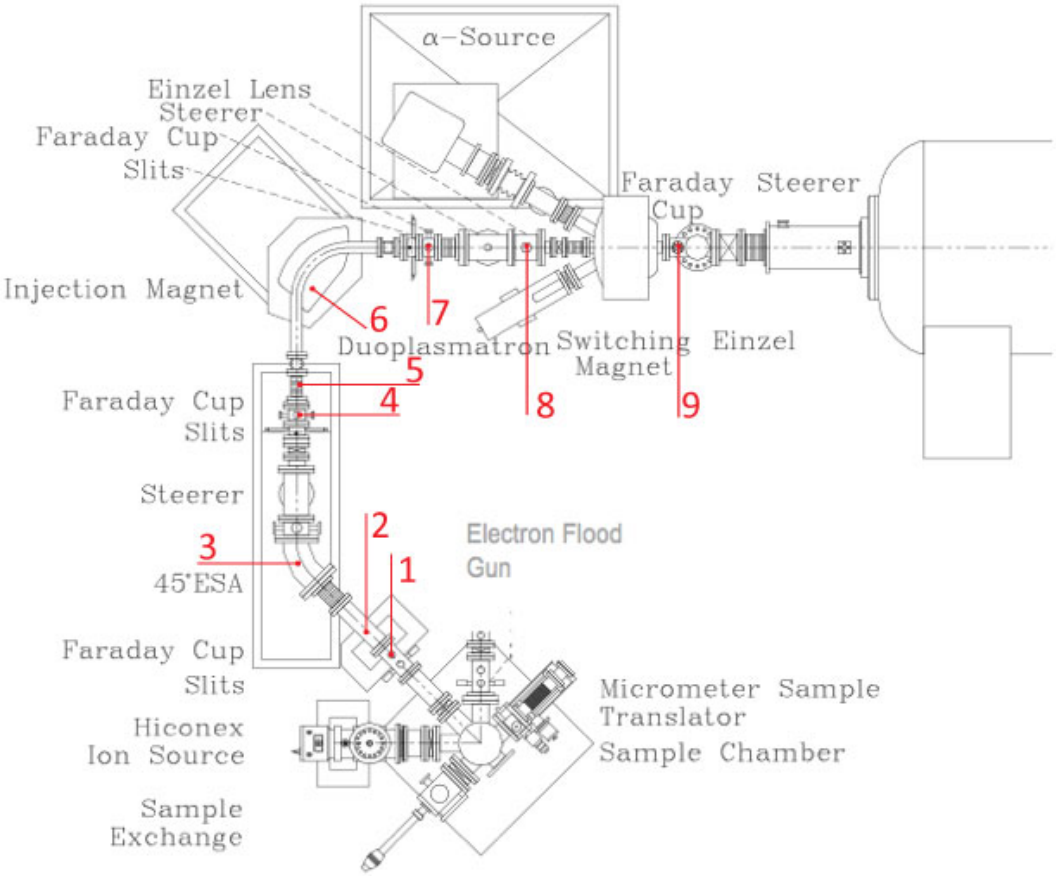

Figure 3.6: General scheme of the injection system, with all its different elements.

The mass scan will be measured in a FC (7) after the magnet. If the electrical current corresponding to an isotope of interest is too weak to be measured with the Keithley Pico ammeter (that is used to measured the electrical current in all the FCs), an ETP ion counter is used instead. This required a system that somehow permitted switching between the three different positions (FC, ETP and beam through) and for it a special small chamber had to be designed. The chamber encloses an axis that holds the ETP and the FC at a 90º angle from each other. The axis is connected to the outside by a feed thru and is attached to a step-by-step motor that is controlled by the computer's labview program. It can rotate between three positions; FC (0º), beam thru (45º) and ETP (90º).

After this chamber the selected mass will proceed through the so-called image einzel (8). This einzel lens focuses the beam in the last FC (9) before the beam enters the accelerator. When this LE FC is lowered the beam enters the accelerator and is measured in the FC after the accelerator (HE FC). Between these two faraday cups there are a few electrostatic elements that have to be optimized, both at the entrance and at the exit of the accelerator. On the low energy side, there are two sets of lenses; the matching lenses and the tube lenses and a set of x and y deflector plates. On the high-energy side there are a set of x and y deflector plates and a set of X and Y focusing electrostatic quadropoles.

The stripping system is controlled at the accelerator's main console and consists of a step-by-step motor that controls the valve of an argon gas bottle located inside the accelerator tank. This valve is connected to a tube that feeds the argon gas to the accelerator tube.

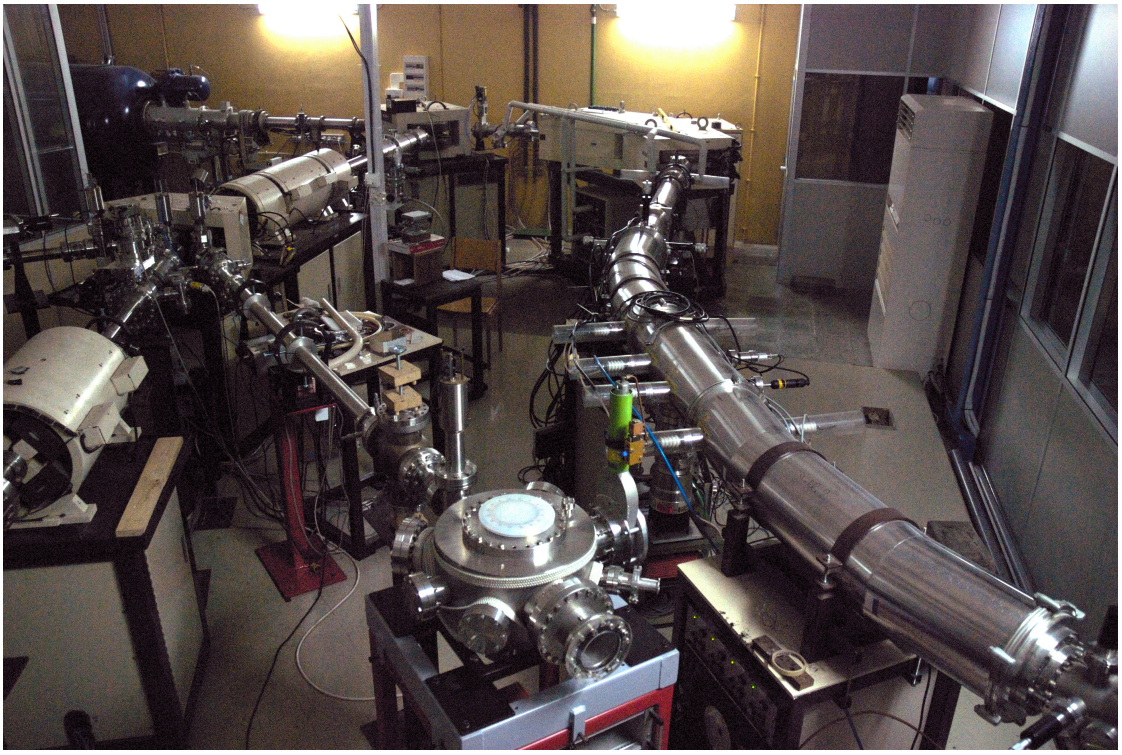

Figure 3.7: High-energy beam transport system. So-called because the ions it transports are usually in the MeV energy range. It comprises all the elements in the line that connects the accelerator (on the top left side of the image) with the detector chamber, which is located after the slits still visible at the low right corner of the image. The larger diameter tubes that connect to these slits enclose the HE ESA's. A notable feature of this line is the

Danfysik magnet (visible below the second light counting from the left on the top of the image). Also visible in this image are two other beam lines that do not belong to the high-energy beam transport line branching from the second switching magnet that appears just below the accelerator in the image. The first switching magnet is the first magnet after the accelerator.

3.1.2.2 The High-energy (HE) beam transport system

The HE beam transport system can be seen in figure 3.7. In figure 3.8 a general scheme shows all the main components of this part of the micro AMS system. The numbers in brackets in the following text refer to the numbers shown in this figure.

As mentioned previously, there will be a predominantly mono-atomic beam after the accelerator, with several positive charge states. After the HE FC (1) is lowered, the beam proceeds to the 1.3 m radius HE magnet (2), which was built by Danfysik, and is corrected to the second order with a nominal maximum beam product (mE/q^2) of 140 MeV/amu, although it can work up to 10% above the specifications, which allows for analysis of mass 240 at 15 MeV (5+ charge state at 2.5 MV terminal voltage) [3]. The pole tips have a 3 cm gap and are 15 cm wide and have between them a 10 cm wide by 2.5 cm high stainless steel beam box, which allows at least ± 10 amu latitude in transmission at mass 240. The magnet power supply is provided by a Danfysik model 858 current supply regulated to 1 ppm.

After the Danfysik magnet there is a special set of FCs (3). The main FC is a normal retractable FC situated along the beam axis in the center of the tube. Close to it however, another off-axis FC was installed. This FC was built at CTN-ITN and was designed to minimize the loss of secondary electrons when a beam impinges upon it. It was designed to be used in the measurement of isotope ratios lower than 10^{-4}, as in such cases the more intense isotope current cannot be measured by the particle detector. This means that the current measured in this FC will be used to calculate the final isotopic ratio, and so it needs to be reliable.

After the Danfysik cups the beam passes thru a pair of 3 m radius ESAs (4), each with a 22,5º bend, that will work as energy filters as in the LE side.

In order to correct possible misalignments of the beam between the exit channel of the magnet and the detector chamber, a set of X and Y electrostatic quadrupoles (5) is located after the magnet and again between the two ESAs (6). The quadupole between the ESAs has the double purpose of maintaining the beam envelope bellow 25 mm and keeping the ESA voltages below 50 kV thus avoiding hazardous X-ray background.

3.1.2.3 The Electrostatic Analyzers (ESA´s)

The LE ESA is a 45º curved tube, which encloses two curved plates (they are curved both horizontally and vertically) which are polarized with opposite fixed voltages (usually around 1000 V). The spherical shape of the plates will focus the beam both horizontally and vertically, making the ESA a double focusing device.

In the high energy side of the system two more ESA´s are used. All ESA's are used for the same goal and work using the same principle, that will be briefly explained.

An electrostatic field $\vec{\varepsilon}$ is created between the two plates, separated by distance d, via the application of opposite polarity voltages on each of its plates, thus creating a potential difference ΔV. An ion passing through this electrostatic field will have a centripetal force $\vec{F}$ acting upon it:

$$F=q\xi$$

$$q\xi=2E/r$$

the circular trajectory of an ion inside the ESA will have a radius r given by:

$$r = \frac{2Ed}{q\Delta V}$$

For a cylindrical analyzer, ions with the same E/q value will follow concentric paths inside the ESA, while unwanted ions with different E/q values will undergo trajectories with a different r, exiting the ESA with a deflection Δy from the central radius r :

$$\Delta y \sim \frac{q\mathcal{E}L^2}{4E}$$

where L is the length of the plates.

Since it is important to maximize Δy, the size of the ESA, L, should be as large as possible, depending on the beam energy and charge state selected.

The ESA will permit a control of the energy distribution. A 45° bend spherical electrostatic analyzer operating in the double focusing mode has a dispersion of $2r$. If operated at unity magnification, with object and image distance of $(\sqrt{2}+1)r$, a 30 cm ESA can achieve an energy resolution of 600 with 1 mm slits.

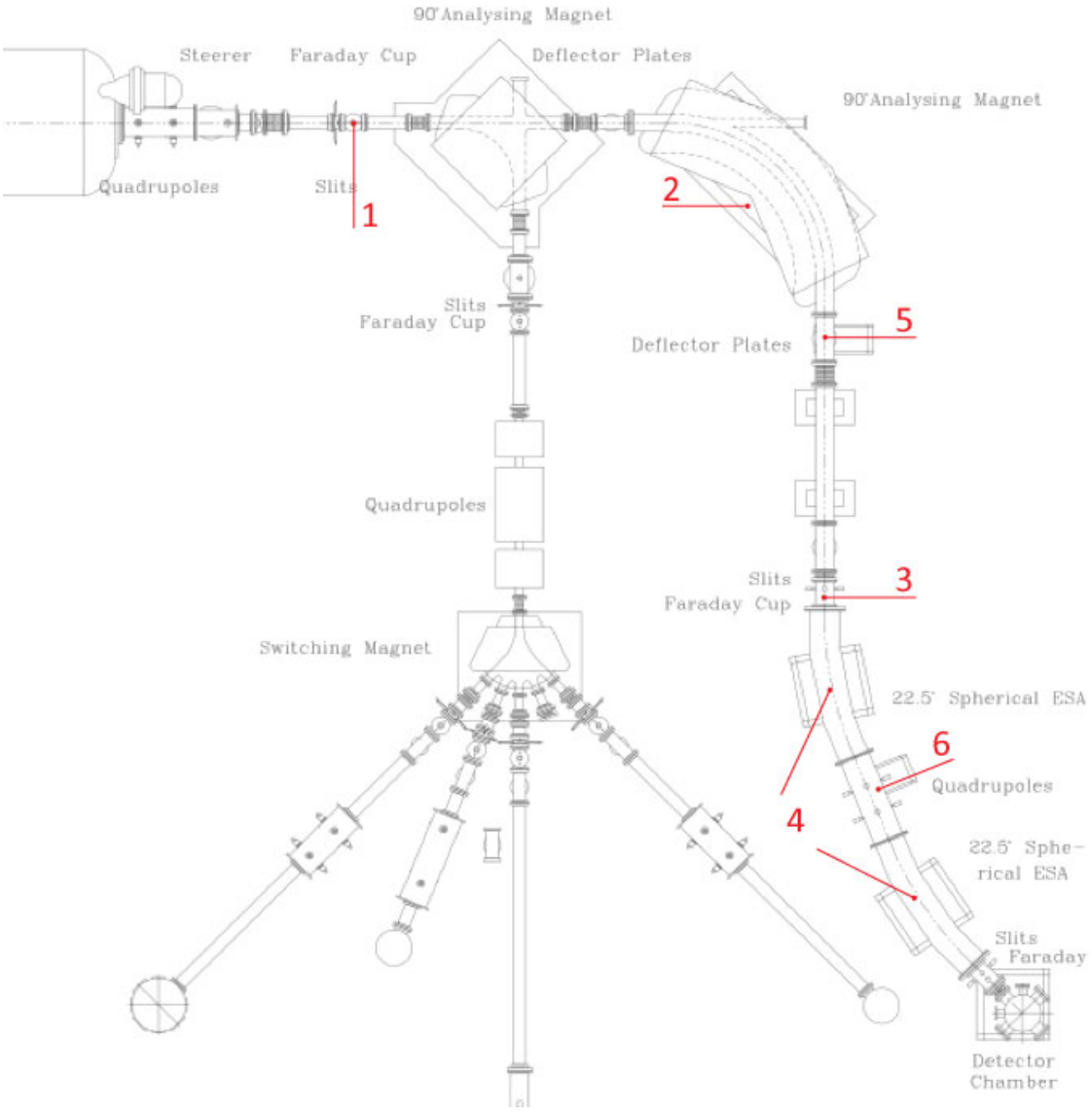

Figure 3.8: General scheme of the High-energy beam transport system with all its different elements.

3.1.2.4 The stripper

The stripping process in the context of tandem based AMS constitutes the physical process by which the electrons of the outer shells of an incoming

mono-negative ion are removed when the ion interacts with a gas at a certain pressure inside a tube in the center of the accelerator (called stripper channel), thereby changing the ion's polarity. This change in polarity allows for achieving particle final energies $E_f = E_i + (q+1).e.V_t$, as a particle will be accelerated towards the center of the accelerator while entering the accelerator tube at charge state -1 and then again pushed towards the exit channel of the accelerator, by the same terminal voltage $+V$, after changing its polarity to $+n$ in the stripping channel. This means that a tandem of 3 MV terminal voltage (TV) as the one in LATR will be able to accelerate heavy ions to several MeV of energy (ex: $^{110}Ag^{7+}$ ions will achieve a final energy of 24 MeV at $TV =$ 3 MV).

Another feature that is of crucial importance to AMS is that molecules become unstable in the stripper channel and molecules in charge states above 2+ will dissociate into their atomic counterparts. This resolves the molecular interferences that plague other mass spectrometry techniques like SIMS and is one of the main advantages of the AMS technique. The other is that the very high energies attainable with relatively low terminal voltages allow for isobar separation using ionization chambers as will be explained further down the text.

The ion charge state after exiting the stripper channel depends on a number of factors that affect the stripper efficiency, such as the gas itself, it's pressure and the terminal voltage of the accelerator. Besides gas stripping, sometimes a solid stripper is used, usually a thin foil of carbon or other material. This usually allows for reaching higher final charge states for the same terminal voltage when compared with gas stripping but also increases beam energy straggling.

The stripping apparatus keeps around 1 to 2 $\mu g/cm^2$ of gas in the central part of the tandem accelerator as the beam passes through it, while keeping the rest of the accelerator tube at the lowest possible pressure. In the case of the LATR system, gas is introduced into the middle of a 8 mm diameter and 1 m long canal. The gas exiting from the ends of the canal is restricted in the low-energy side part by a tighter lower conductance area so that the gas will be pumped mainly through the high-energy side of the tube. This is important

because it will minimize the influence of the gas on the slow moving ions of the low energy side of the accelerator tube.

3.1.3 The Cockcroft-Walton 3 MV Tandem accelerator

The 3MV tandem accelerator, in which the Micro-AMS system is based, was built by High Voltage Engineering, and is based on a Cockcroft-Walton voltage generator. This generator uses a ladder of capacitor-rectifier circuits, where a transformer provides alternate current at a certain voltage into a cascade generator that works as a rectifier and multiplier device.

This type of accelerator was developed by J.D. Cockcroft and E.T. Walton, who built the first prototype in 1932 [4]. It had a maximum voltage of 700 kV, and was instrumental in the beginning of the study of nuclear reactions with accelerators. In their first experiment 400 keV protons hit lithium targets, producing the nuclear reactions ^{7}Li+p → ^{4}He + ^{4}He and ^{7}Li +p→^{7}Be + n. For these important developments they were awarded the Nobel prize in physics in 1951.

A voltage multiplier circuit, also called cascade generator, invented by H. Greinacher in 1919, provides the high voltage of the Cockcroft-Walton accelerator. In figure 3.9, in which a four-stage voltage multiplier is shown, the two columns P and S (pushing and smoothing) are composed of high voltage capacitors, and connected to each other by high voltage diodes. A high voltage transformer feeds a high frequency signal to the columns, which charges the capacitors in the pushing column in the positive half period of the wave and the smoothing column in the negative part of the period.

If U_0 is the amplitude of the AC signal fed to the system by the HV transformer, then the voltages at the points between each capacitors will be, for the P column and starting from the bottom of the column,

$$U_0 + U_0 \sin(\omega t)\,, U_0 + 3U_0 \sin(\omega t)\,, U_0 + 5U_0 \sin(\omega t)\,, U_0 + 7U_0 \sin(\omega t),$$

and for the S column (again starting from its bottom);

$$2U_0,\ 4U_0,\ 6U_0,\ 8U_0.$$

This means that the achievable terminal voltage (U) depends only on the number of stages, $U = 2nU_0$, with n being the number of stages. However, since the terminal voltage is DC, there will be a mean voltage drop ΔU and a ripple δU in the final signal, proportional to the signals DC current, I;

$$U = 2nU_0 - \Delta U \pm \delta U,$$

with;

$$\Delta U = \frac{I}{fC}\left(\frac{2}{3}n^3 + \frac{3}{4}n^2 + \frac{1}{12}n\right),$$

And:

$$\delta U = \frac{I}{fC}\left(\frac{n(n+1)}{2}\right)$$

where f is the frequency of the AC signal and C is the capacitance of the capacitors. This drop can be kept to a minimum by maximizing the frequency f and the capacitance C of the capacitors, while keeping the number of cascade units low.

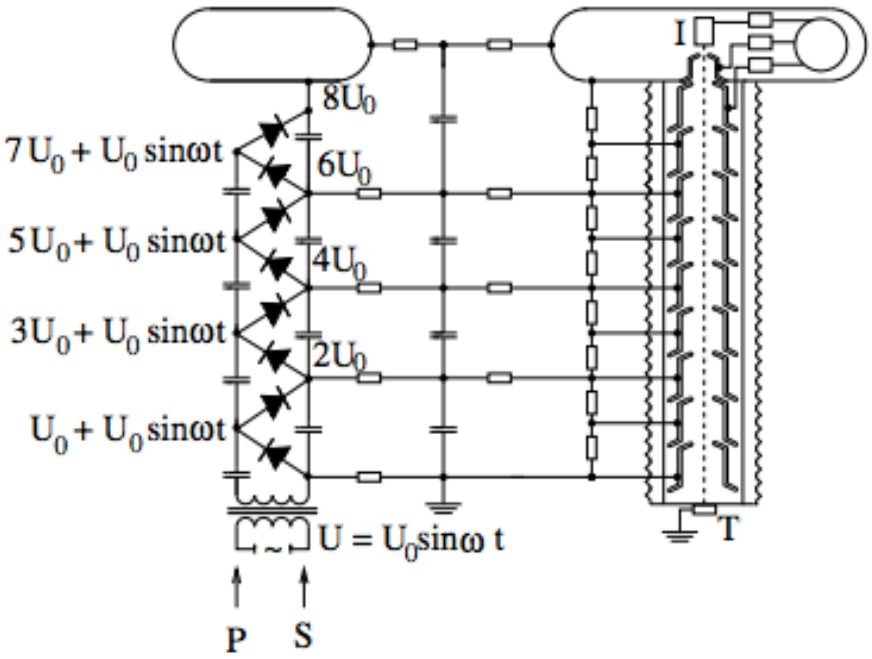

Figure 3.9: Scheme of a Cockcroft-Walton generator.

3.1.4 The detector chamber

The so-called detector chamber is actually composed of two chambers. The first chamber includes a FC, an ETP and a PIPS (*Passive implanted Planar Silicon*) particle detector and the second chamber is the *E,ΔE* detector. In the first chamber there is a rotating axis perpendicular to the beam axis that can switch between four positions; FC, ETP, particle detector and beam through. If the beam goes thru it passes a 300 nm silicon nitride window and enters the *E,ΔE* detector. When no isobaric interference is involved only the first chamber is used. If the ion current is higher than 1 pA the FC and its Keithley pico ammeter are used. If it is below this value the ETP or the particle detector are used instead. The particle detector has the advantage of providing energy information besides ion count. If there is an isobaric interference the *E,ΔE* detector is normally used. The *E,ΔE* detector can also achieve higher energy resolution than a PIPS detector if very thin silicon nitride windows are used as is the case in LATR. This can be useful for separating interfering molecules in

the very high mass range (even if most molecules are destroyed in the stripper channel some fragments can still reach the detector chamber in very small counting rates).

3.1.4.1 The *E,ΔE* detector at LATR

The *E,ΔE* detector at LATR is a ionization chamber. The whole detector chamber can be seen in figure 3.10. It has three anode plates and one cathode plate with a Frisch grid. This grid ensures that the size of the induced pulses is independent of the lateral position of the ionization event across the chamber. Besides the plates, there is a PIPS particle detector at the chamber where the ions are stopped, and where additional ion energy information can be obtained.

It is equipped with a silicon nitride window, with a thickness of 100 nm. The pressure of the gas, a mixture of argon and methane, can be adjusted depending on the ions being separated. The system that allows the injection of the gas into the chamber and the fine control of its pressure had to be developed as a part of the work for this thesis. It uses a rotary pump to circulate the gas. Since all four signals (anodes 1-3 and particle detector) or a combination of these have to be taken in coincidence, a special DAC system has to be used.

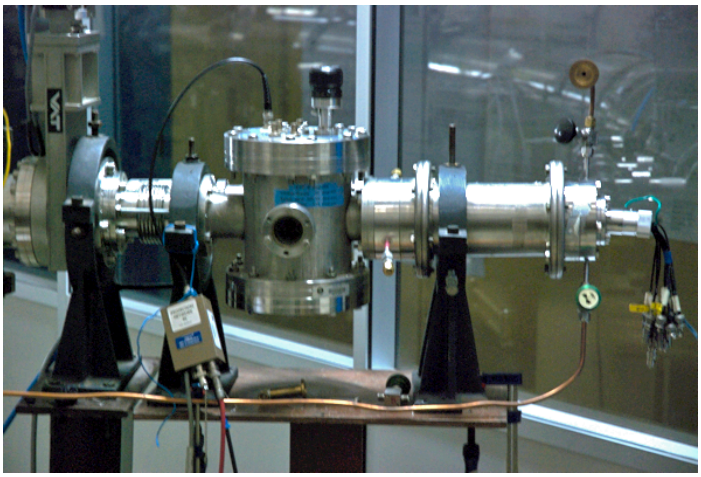

Figure 3.10: Detector chamber at LATR/CTN-ITN. The particle detectors and the FC are at the center of the chamber with the circular glass window. On its top it is visible the black handle that allows for the rotation of the rod that holds the detectors and FC. By rotating it is possible to select one of these or let the beam enter the

ionization chamber that is the tube on the left side of the central chamber. It is also visible in this image a part of the gas circulation system connected to the ionization chamber.

This detector is used mainly to resolve isobaric interferences. An isobaric interference is said to exist when two isotopes of different elements but equal mass exist in the sample, and both form negative ions in the sputtering process. Since they have the same mass and the same charge state, they will follow the same path along the system, including in the magnets and ESAs, and arrive at the detectors with the same energy, being therefore indistinguishable in a normal PIPS detector. In order to understand how it is possible to separate these kind of interferences it is important to introduce some physical concepts related with the interaction of heavy charged particles with an absorber, in the particular case of the E, E,ΔE detector used in AMS, a gas absorber.

3.1.4.1.1 Interaction of heavy charged particles with an absorber gas

When heavy charge particles moving with kinetic energy in the MeV energy range interact with matter, in this case a gas, they will mostly interact with the absorber gas through coulomb forces between their positive charge and the negative charge of the orbital electrons of the absorber gas atoms, although they can also, very rarely, interact directly with the nuclei.

As the heavy positively charged particles penetrate the gas, the electrons in the gas, through coulomb attraction, will be brought to higher-lying shells of the gas atom, exciting it, or they will be removed altogether from the atom, that becomes an ion. The energy that the electrons receive will be subtracted to the charged particle resulting in its slowing down. Since the maximum energy that an electron receives in such an interaction is about 1/500 of the particle energy/nucleon, a great number of such interactions must occur for the incoming charged particle to stop completely. They will occur simultaneously and in several directions, and will result in the heavy charged particle losing its energy along a more or less straight path, until it stops.

The stopping power S for a charged particle in a given absorber translates the rate of energy loss of a charged particle along a path x, and, for particle energies E, is given by:

$$S = -\frac{dE}{dx} = \frac{4\pi e^4 z^2}{m_0 v^2} NB \qquad (1)$$

where

$$B = Z\left[\ln\left(\frac{2m_0 v^2}{I}\right) - \ln\left(1 - \frac{v^2}{c^2}\right) - \frac{v^2}{c^2}\right]$$

with m_0 being the rest mass of an electron and e its charge, z the atomic number of the stopping particle, and v its velocity, N the number density of the gas atoms and Z its atomic number, I represents the average excitation and ionization potential of the gas. For $v<<c$ only the first term of B is taken into account.

The dependency of S with the atomic number z of the stopping ion means that, for the same stopping medium, particles with larger z will be stopped in a smaller x. This of course holds only if we assume that the incoming ions are fully stripped of their electrons when they start interacting with the absorber gas. This is achieved by the interaction of the ions with the detector silicon nitride window, so that this dependency of S on z may be assumed for the gas inside the detector.

Hence $S(E)$ increases proportionally to $1/E$ up to the point where the particle starts to pick up electrons until it eventually becomes neutral at which point the curve fall to 0. Due to this maximum of $S(E)$ vs E at very low energies, the charged particles will deposit most of their energy at transversed distances near the particle range (being range the average depth at which the particles stop).

The $E,\Delta E$ detector functioning principle is based on the concept of stopping power and the Bragg peak.

Since isobars have different proton number they will be stopped differently along the gas, accordingly to the dependency of S on z. As they are stopped, they will ionize the surrounding gas, and thus create an electron

discharge along its path, that is proportional to the energy lost by that ion in that periphery. The discharges will be picked up by the 3 plates (anodes) along the way of the stopping ion. So there will be an electric current in each plate that is proportional to the energy deposited by a particular particle beam in the vicinity of that plate. By using coincidence electronics it is possible to associate the three plate signals and the final detector signal to each single ion. Since different elements have different stopping powers, they will produced electric signals with different intensity and will be therefore distinguishable. It may not be necessary to use the four signals. The number of signals used depends on the degree of separation needed. By controlling the constitution and density of the detector window and the type and pressure of the gas it is possible to determine the length x of each element's Bragg curve and so maximize the separation of the isobars. However, there will be many uncontrollable factors affecting the achievable separation. One of the most important is the energy straggling. There can also be some inhomogeneity in the detector window, causing energy spread and low energy tails, and detector properties that will affect the efficiency of the separation such as electronics noise and incomplete charge collection.

The separation factor $S_{A,B}$ [5] of isobars of element A and B in a $E,\Delta E$ detector is defined as;

$$S_{A,B} = \frac{|E_A(x) - E_B(x)|}{\sqrt{\frac{1}{2}\left[\sigma_A^2(x) + \sigma_B^2(x)\right]}}$$

where $E_A(x)$ and $E_B(x)$ are the residual energies of ion A and B, after passing through a layer of silicon nitride of thickness x and a gas layer at a certain pressure, and $\sigma_A(x)$ and $\sigma_B(x)$ are the distribution widths due to energy straggling. This is a usual concept as it allows for rapid comparison between the isobar separation capabilities of different AMS systems. The possibility of separation of isobars with gas ionization chambers was of central importance to the development of the AMS technique. However, there are important limitations to this technique that have to do with the available energy for

separation. This limitation has to do with the fact that the separation factor $S_{A,B}$ becomes smaller for a given energy as the mass of the isobars becomes larger, and can only be increased if the energy increases. So, the higher the terminal voltage in the accelerator, the heavier isobars the AMS system will be able to separate in its $E,\Delta E$ detector.

For AMS systems based on 3 MV tandems like the one in CTN-ITN, which constitute around half of the present AMS systems working around the world, the gross of their AMS analysis will be based on the radioisotopes ^{10}Be, ^{14}C, ^{26}Al and ^{129}I (that has no interfering isobar), which have a large number of successful applications, as other commonly measured isotopes are out of their separation range, like ^{36}Cl (because of the interfering stable ^{36}S), ^{41}Ca (^{41}K) or ^{60}Fe (^{60}Ni) due to insufficient energies.

3.1.5 The Bouncing system

The bouncing system was developed to allow for very fast switching between different isotopes when measuring isotopic ratios. It was based on a technique pioneered by Amsel and coworkers [6]. The fast switching of isotopes is very important because it allows for collecting counting rates for up to eight isotopes almost simultaneously, therefore reducing errors associated with beam instability in time. This beam instability is related with fluctuations in the primary beam, magnetic field drift, instabilities in the power supplies of the different lenses and deflector devices along the system and voltage drifts in the accelerator terminal. The accelerator's terminal voltage stability should be around 10^{-4} in a Tandetron accelerator, corresponding to a 250 V ripple at 2.5 MV terminal voltage, but in practice, with only a Generating Voltmeter (GVM) stabilization of the kind operating at LATR, the difficulty in obtaining a stable reference voltage results in instabilities superior to twice that value.

The bouncing system avoids the magnetic hysteresis that would make isotopic ratio measurements very difficult if the switching between isotopes were to be made using the magnetic field.

The bouncing system is divided in two sections; the low-energy bouncing system and the high-energy bouncing system. They both use the principle of imposing a variable electric field over a static magnetic field, thus avoiding having to deal with the slowness and the hysteresis inherent to the magnetic field. The way the electric field is applied is different in both cases; in the low-energy bouncing system, the electric field is applied by connecting a TREK HV amplifier with a slew rate of 600V/ms directly to the magnet beam box. This box is of course insulated from the rest of the system by two ceramic tube sections. During analysis, the magnetic field is chosen to be slightly higher than necessary to pass the heaviest isotope of the ones in study. With this fixed magnetic field applied, we start slowly increasing the electric voltage applied to the beam box. By increasing this electric field the incoming beam will be slowed down, and since its energy has changed it will be deflected thru a different path inside the beam box's magnetic field. When exiting its energy will be the same again as when entering the beam box. By this procedure we can select the different isotopes of interest by applying different voltages, always with a fixed magnetic field.

In the case of the HE bouncing system, the electric field is applied to two pairs of vertical plates (20 cm long by 5 cm wide separated by a 2.5 cm gap), at the entrance and exit of the HE magnet beam box. The electric field is also provided by, in this case, two TREK HV amplifiers with a 10 kV/30ms slew rate. Both the LE HV amplifier and the two HE HV amplifiers are controlled in sync by a Iotech pulse generator.

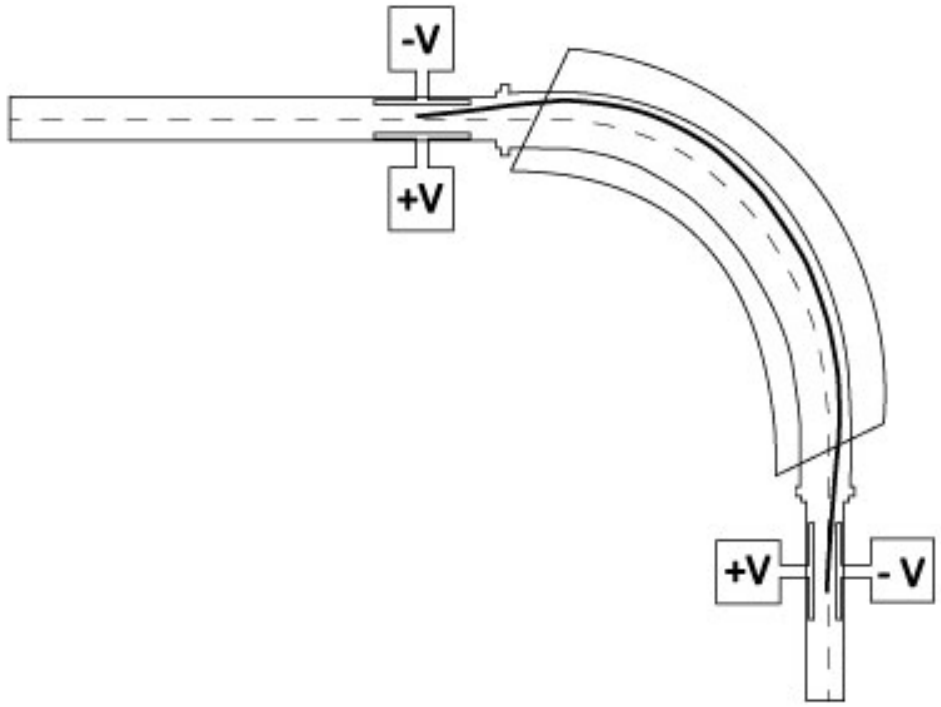

Figure 3.11: Scheme of the High-energy bouncing system.

By adjusting the voltages of the entrance and exit pair of deflector plates visible in the image, it is possible to switch between neighbor isotopes at great speed while maintaining a fixed magnetic field.

The Bouncer system is operated through a labview program that can calculate the isotopic ratios in real time. It allows for the selection of the number of isotopes in a particular analysis, the time per cycle (each cycle accumulates the count rate of incoming ions of each isotope in the chosen time window), the number of cycles in each run and the number of runs. It plots the accumulated counts of each isotope in a run, while automatically calculating the isotopic ratios and the associated standard deviation per run.

The precision of isotopic measurements can be increased dramatically by reducing the time of acquisition in each cycle, while increasing the number of

cycles per run so that each run has a sufficient number of counts per isotope to minimize the statistical uncertainty.

In the lead isotopic measurements that will be described in chapter 5, a precision in the permil range was achieved in the lead isotopic measurements by using a 10 ms collection time per isotope per cycle.

3.1.6 Labview Computer control program

The labview control program is essential in the operation of the Micro-AMS system at CTN-ITN. It was developed in Australia when the system was first installed. It was modernized when it arrived at the LATR.

The main program, called Tandem control program is made up of several smaller programs. The most important are: Scan device, scan iotech, scan sample stage, scan mass, scan bouncer.

3.1.6.1 Scan device

The scan device program controls all the HV power supplies that feed the different electrostatic devices, both in the low-energy and high-energy side of the accelerator. It has a 12 bit resolution that in most of the HV power supplies translates into a 0-10 V control signal. In the program, the operator can choose which device will be the detector, and the program will plot the count rate per chosen time unit, or ampere if the keithley pico ammmeter is selected (which will be connected to a FC) vs DAC value in the x axis. The DAC value corresponds to a voltage. The plot of beam intensity vs device voltage is very helpful in tuning the beam since it provides information about the alignment of the beam and its symmetry.

When the pico ammeter is selected, the plotted current will be the one measured in the selected FC that is nearest to the target chamber. The beam transport system is then tuned by maximizing the current in the nearest FC by scanning all the devices before it. Once the beam is maximized, the set of

devices between this FC and the next is optimized using its feedback. This continues along the whole beam transport system until the detector chamber.

The scan device program controls not only the beam transport devices but also all the electrodes in the target chamber and ion source, namely the source's focus lens, focus steerer X and Y, and the target chamber's primary einzel, target potential, screen lens and secondary einzel lens.

3.1.6.2 Scan sample stage

This program allows for the control of the sample stage that moves the sample holder in 3D. It can memorize up to 10 positions.

3.1.6.3 Scan Mass

The Scan Mass program controls both the low and the high-energy magnets. In the case of the low energy magnet it controls the magnet 40 A current supply with a 10 V signal divided into 4096 steps. In the case of the high energy magnet the DAC resolution is much higher; 10^5 steps. This program allows for the calibration of the magnets and it too plots current or counts per time unit (depending on the detector) vs DAC steps, that in this case represents magnet current.

3.1.6.4 Scan Iotech

The Iotech is a 16-bit resolution DAC that controls the bouncing system. The scan iotech program operates both the HE and the LE bouncer system. It can save the LE and HE DAC positions for up to eight isotopes. These correspond to the voltages applied on the LE and HE bouncing systems that allow the passage of each isotope, while the magnetic fields in each magnet are kept stationary.

3.1.6.5 Scan Bouncer

The DAC values of the LE and HE bouncer voltages corresponding to the different isotopes are then automatically uploaded to the Scan bouncer program. This program allows for the operator to set the time that each isotope will be measured in one cycle. The amount of cycles per run, and the number of runs in the measurement may also be chosen. When the program starts it will cycle through the isotopes repeatedly while plotting the isotope ratio in real time for each cycle. It also calculates the standard deviation in real time of the measurement as the number of runs increases.

References

[1] S.H. Sie , T.R. Niklaus, G.F. Suter , Nuclear Instruments and Methods in Physics Research B 123 (1997) 558-565

[2] S.H. Sie et al, Review of Scientific instruments Vol. 69, 3 1997

[3] S.H. Sie , T.R. Niklaus, G.F. Suter, Nuclear Instruments and Methods in Physics Research B 123 (1997) 112- I21

[4] Cockcroft, J.D. and Walton, E.T.S. (1932). Proc. R. Soc. London **A137**:229

[5] P. Steier et al., Nuclear Instruments and Methods in Physics Research B 240 (2005) 445–451

[6] G. Amsel, E. D'Artemare and E. Girard, Nucl. Instr. Meth. 205 (1983)5.

4

Basic concepts regarding the sputtering process

Sputtering, defined as the process by which there is an erosion of a material's surface by particle bombardment is a central phenomenon in Micro-AMS. This chapter will try to illuminate this very complex physical process by focusing on several of its characteristics, but due to its limited length, it will not be a complete account of the current knowledge of this phenomenon. It will focus on the aspects of sputtering that are more relevant to the LATR Micro-AMS system, namely sputtering with 10 keV Cs^+ primary ions.

4.1 The sputtering process

The phenomenon of sputtering in physics has been approached experimentally, theoretically and through computer simulations, and most advances in the studies regarding it come from close integration of these three approaches. As far as theory is concerned, many models trying to describe the

sputtering process have been advanced throughout the last decades, but none is yet fully successful in explaining the physical details of the sputtering process.

When we speak about ions bombarding a surface, there are two kinds of processes happening simultaneously; nuclear processes and electronic processes [1]. The first kind refers to elastic interactions between a projectile ion or atom and a target atom, the second process involves excitation, ionization and charge transfer. Which of these processes is dominant in a given interaction between incident ion and surface, depends on the energy of the incident ion; at low energies, nuclear processes are the most important and at higher energies the electronic processes begin to dominate. There is a middle point in terms of incident ion energy where both processes are important. This middle point depends on the atomic numbers of both the incident ion and the target material, increasing with the incident ion's atomic number. In the case of the 10 keV Cs^+ incident ions that are used in this work, the nuclear processes are clearly dominant, and so these will be analyzed further.

In order to better understand the phenomena involved in sputtering by nuclear processes, it is perhaps best to introduce the concept of collision cascades. This concept, has produced some of the most interesting results in terms of providing quantitative explanation to the observed data [2].

In the collision cascade model, as conceived by Sigmund, the transfer of energy and momentum from the incident particles to the target material is done by a succession of cascades of energetic binary collisions between the ion and the target particles and consequently by recoiling target atoms and its stationary neighbors. The emission of particles from the surface happens when a surface particle receives energy from a collision cascade in its vicinity that will give it enough energy, through a binary collision, to overcome the surface binding energy. A collision is considered binary when two interacting particles come so close together that they "feel" the influence of each other with such intensity (usually this intensity is enough to cause considerable deflection of the incoming ion) as to make other, more distant, particles' influence negligible. This means that in a binary collision, for all practical purposes, energy and momentum transfers involve only two particles.

The cascade multiplication will end once the energy of a recoil atom reaches its lattice binding energy. In this case, the rest of its energy will be dissipated by heat. This kind of process is called a linear cascade. Alternatively, a collision cascade can have such density that all the target atoms in a certain volume are set in motion. This process is called a spike. The process by which a spike causes ejection of surface material is by a transfer of its energy to the surface by shockwaves, that is, the energy is transferred through the material's medium as vibrations in its structure.

In the case of the linear cascade, it is important to consider two energies; E, which is the projectile energy, and U that is the surface binding energy. For sputtering to occur E must be greater than U, although sputtering thresholds, that is, the value of E for which surface particle emission begins to occur, are usually one order of magnitude or more higher than U. As an example, for sputtering with Xe primary ions on a carbon target (U = 7.42 eV for C), the threshold energy E_{th} was determined experimentally to be 24.2 eV [3].

The energy E will also determine the dimensions of a cascade, not only in terms of the depth of penetration of the projectile, which is called range, but also in terms of lateral and longitudinal dimensions of its zigzag path through the target. These lateral and longitudinal dimensions are called straggling. Cascade dimensions depend also on the projectile element and the target element.

Figure 4.1 shows a collision cascades simulated by the TRIM program, for 10 keV Cesium ions impinging at 45º angle to the surface of the target.

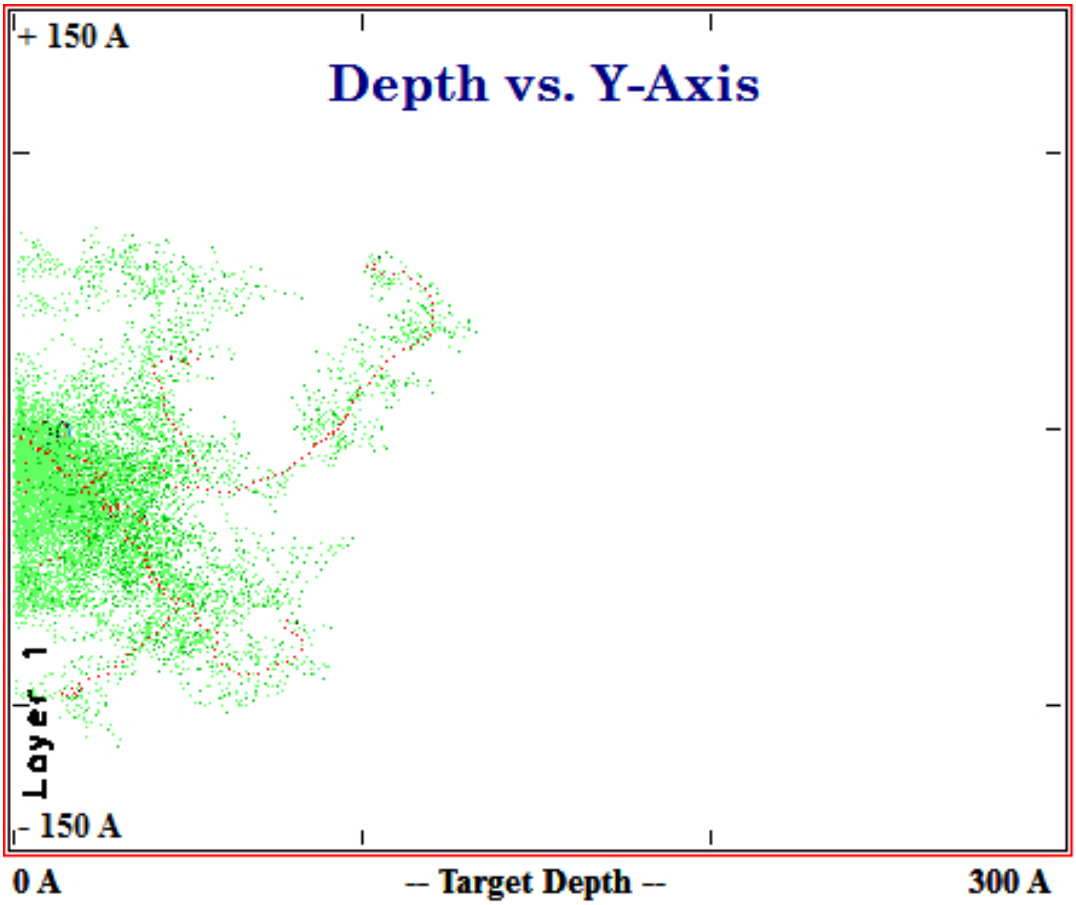

Figure 4.1: Collision cascades simulated by the TRIM program, for 10 keV Cesium ions impinging at 45° angle to the surface of the target. The plot shows the trajectory of the cesium ions in red as they are stopped in silicon. The trajectories of the atoms of the target set in motion by binary collisions with the primary cesium atom and/or subsequently with other atoms of the element are shown in green.

4.1.1 Sputtering yield formalisms

As far as the present technique is concerned, and especially due to its use of standards, it is not imperative to have a detailed model of the sputtering process as long as there is the possibility of measuring the currents of the primary and secondary beams, as well as knowing its characteristics; type of ion or molecule, charge state, current, energy and angles of incidence or emission. With this information we can introduce some useful definitions regarding the sputtering process, all deriving from the definition of sputter

yield (of a molecular or atomic particle R emitted from a target), defined as the average number of particles R leaving the sample for each ion of the primary beam hitting it.

As stated in Benninghoven [3], for a primary beam of ions R^q_p, in charge state q and energy E_p, at φ_P azimuthal angle and with an angle ψ_P of incidence relative to the normal of the sample, impinging on a target compound R_t (with crystal orientation (hkl)) there will be a secondary ion emission, of one or several types of molecules or atoms, R^q_s (a target can be composed of several different elements $A_iB_jC_k$, with different concentrations $c(A)$, $c(B)$, $c(C)$) in charge state q, energy E_s and ψ_s, φ_s angles of emission).

The specific differential sputter yield for molecule R_s in charge state q can be defined as:

$$\frac{dY^q(R_s)}{dE_s d\Omega} = \frac{1}{\dot{N}_p dE_s d\Omega} d^3\dot{N}(R_p, E_p, \varphi_p, \psi_p / R_t, (hkl) / R^q_s, E_s, \varphi_s, \psi_s) \qquad (1)$$

The above expression represents the number of secondary particles $d^3\dot{N}$ emitted for each incoming primary particle per time unit. $\dot{N}_p$ represents the number of primary ions per time unit. The secondary particles of the type R_s that are emitted from the sample at the solid angle interval $d\Omega$ are in charge state q and their energies fall in the range E_s, E_s+dE_s.

By integrating the above expression from $E_s = 0$ to E_{max}, and across the full 2π solid angle, we can calculate the specific differential directional yield and the specific differential energy yield for a molecule R_s in charge state q:

$$\frac{d^2Y^q(R_s)}{d\Omega} = \int_0^{E_{\max}} \frac{d^3Y(R_s)}{dE_s d\Omega} dE = \frac{1}{\dot{N}_p d\Omega} d^2\dot{N}(R_p, E_p, \varphi_p, \psi_p / R_t, (hkl)/, R^q_s, \varphi_s, \psi_s)$$

and

$$\frac{d^2Y^q(R_s)}{dE_s} = \int_{2\pi} \frac{d^3Y^q(R_s)}{dE_s d\Omega} = \frac{1}{\dot{N}_p dE} d\ \dot{N}(R_p, E_p, \varphi_p, \psi_p / R_t, (hkl)/, R^q_s, E_s)$$

The specific yield for particles R_s in charge state q is then obtained by integrating (1):

$$Y^q(R_s) = Y(R_p, E_p, \varphi_p, \psi_p / R_t, (hkl)/, R_s^q) \Leftrightarrow$$

$$Y^q(R_s) = \int_0^{E_{\max}} \int_{2\pi} \frac{d^3 Y^q(R_s)}{dE_s d\Omega} dE_s \, d\Omega \Leftrightarrow$$

$$Y^q(R_s) = \frac{1}{\dot{N}_p}(R_p, E_p, \varphi_p, \psi_p / M_t, (hkl)/, R_s^q)$$

The above expression will be simplified when, as is the case in our experiments, the primary beam parameters do not change in time:

$$Y^q(R) = \frac{N^q(R)}{N_p}$$

$N^q(R)$ is the number of secondary particles R in charge state q.

During the sputtering process in the target, most of the ejected secondary particles are neutrals (somewhere around 90% for most cases depending on the projectile and target). The probability for charge state q, $\alpha^q(R)$, that is the number or emitted particles in charge state q divided by all the emitted particles R, is given by:

$$\alpha^q(R) = \frac{N^q(R)}{\sum_q N^q(R)} = \frac{N^q(R)}{N(R)}$$

In the case of our system, in which only particles in which $q = -1$ are selected, $\alpha^q(R)$ is known as the degree of single negative ionization:

$$\alpha^q(R) = \frac{N^-(R)}{N(R)}$$

Both $Y_q(R)$ and $\alpha^q(R)$ are highly dependent on the characteristics of the target, such as its composition, chemical state and crystallographic orientation. This means that the same trace element present in different substrates can produce very different secondary beam intensities. This effect is called the matrix effect.

If we sum all the specific yields in charge state q, over all species in the target (atoms, molecules and clusters) $R = A_i B_j C_l$ that contain atoms of element A, we get the total yield, Y_{tot} , for atoms of element A in the target:

$$Y^{q}_{total}(A) = \sum_{l} iY^{q}(R_l) = \frac{1}{\dot{N}_p}\sum_{l} i\dot{N}^{q}(R_l) = \frac{\dot{N}^{q}_{total}(A)}{\dot{N}_p}$$ (ions/primary particle)

where

$$\dot{N}^{q}_{total}(A) = \sum_{l} i\dot{N}^{q}(R_l)$$

is the total number of emitted *A* atoms from the sample even if they are sometimes associated with other elements in the form of molecules or clusters, whereas $N^q(A)$ represents only emitted atoms of element *A* in atomic form and again charge state *q*. The *l* subscript means that all possible molecular species containing atom *A* coming from the target must be added.

If we integrate the above expression for an element *A* over all charge states *q*, we obtain the total number of atoms of element *A* leaving the sample for each impinging primary ion, which is called the total atomic yield for element *A*:

$$Y_{total}(A) = \sum_{q}\sum_{l} iY^{q}(R_l) = \sum_{q}\sum_{l} \frac{i\dot{N}^{q}(R_l)}{\dot{N}_p} = \frac{1}{\dot{N}_p}\sum_{l} i\dot{N}(R_l) = \frac{\dot{N}_{total}(A)}{\dot{N}_p}$$

(atoms/primary particle)

Figure 4.2 shows the total atomic yield for mono-elemental targets as calculated by the TRIM program, using 10 keV Cs^+ primary ions hitting the target at a 45° angle with the surface, as is the case of the LATR/CTN-ITN Micro-AMS system.

For a target composed of elements *A,B,C,* the total sputtering yield can be defined as:

$$Y_{tot} = Y_{tot}(A) + Y_{tot}(B) + Y_{tot}(C) = \frac{Y_{tot}(A)}{\alpha} = \frac{Y_{tot}(B)}{\beta} = \frac{Y_{tot}(C)}{\gamma} \quad (2)$$

where α, β, γ are the mole fractions of elements *A*, *B*, *C* contained stoichiometrically in the sample, such that $\alpha + \beta + \gamma = 1$.

If the elements being studied have more than one isotope, as is the case of all the studies presented in this thesis, the total yield for element *A* can be written as:

$$Y_{tot}(A) = \sum_N Y_{tot}(A^N) = \frac{Y_{tot}(A^N)}{r(A^N)} \qquad (3)$$

where $r(A^N)$ is the relative abundance of isotope A^N of element A so that:

$$\sum_N r(A^N) = 1$$

In both (2) and (3) it is assumed that the sputter yields of the different elements or isotopes in the sample are correlated linearly to their respective concentrations in the sample. When this condition is met, sputtering is called stoichiometric sputtering, and the fractional concentration $c(A)$ of element A in the target is described by:

$$c(A) = \frac{n(A)}{n_{tot}} = \frac{Y_{tot}(A)}{Y_{tot}}$$

where $n(A)$ is the volume density of element A in the sample in *atoms/cm*^{3} and n_{tot} is the number of target *atoms/cm*^{3}.

4.2 Secondary ion currents

Sputtering yields can be measured in the laboratory, by measuring the secondary beam intensity of a given isotope or isotopes, in a given charge state, along with the primary beam intensity. Besides these currents it is also necessary to determine the volume of the sputter crater and the weight of the sample before and after bombardment, in order to determine the amount of target material removed.

In most Micro-AMS analysis all the data collected during measurement is in the form of beam intensity, in ampere or counts per second, and all other physical quantities, such as the concentration of a given trace element in a particular sample, have to be calculated from this measured beam intensities. If these are measured after the low energy magnet (in the LE magnet FC or LE FC, see chapter 3) they can be currents of beams of secondary molecules or of single atoms in a selected negative charge state, usually mono-negative. It can be useful to measure molecular currents instead of individual atom currents at this stage (before their injection in the accelerator) because some elements do not

form negative ions in the sputter process but can be transported through the *LE* beam transport system as negative molecular ions.

The secondary current of a molecule $P=A^N B_j^M C_k^L$, $I^q(P)$, measured in the LE magnet FC or LE FC, between the Le magnet and the entrance channel of the accelerator, can be represented as the product of the following equation:

$$I^q(P) = I_P . c(A) . Y_{tot} . \alpha^q(P) . q . T_{LE}^-(P) . \varepsilon(P) \qquad (4)$$

where I_p is the primary ion current, $\alpha^q(P)$ is the probability for ionization of molecule P to charge state q, $T_{LE}^-(P)$ is the transmission through the low energy mass spectrometer (it takes into account all the losses in the electrostatic lenses, ESAs and magnet that conduct the beam to the detector), and $\varepsilon(P)$ the efficiency of the detector.

Expression (4) is valid also for SIMS since it does not take into account the high-energy section of micro-AMS.

If the beam currents are measured after the accelerator (in the HE FC, see chapter 3) the beam will be composed of positive atomic ions in several charge states (there may still be molecules in $q= +1$ charge state, as these can sometimes survive the stripping channel). By selecting the appropriate magnetic field, a specific charge state can be chosen, so that the current measured in the HE magnet FC is mainly, but not completely in some cases, composed of isotopes of the same charge state. At the HE magnet FC some ambiguities can still occur in some cases; for instance $^{32}S^{4+}$ will travel the same path in the magnet beam box as $^{16}O^{2+}$, for the same magnetic field and energy. However, these will have a different path along the electric fields in the HE ESAs between this FC and the detector chamber, and so these ambiguities will be resolved before reaching the detector chamber.

The electrostatic and magnetic beam transport elements in the HE side of the accelerator will have to be taken into account in order to expand (4) to the whole AMS system. The current of isotope A^N measured in the detector at the end of the micro-AMS line, $I^q(A^N)$, depends on the transmission through the accelerator's stripper channel, where there will be a probability $\beta_E^q(A^N)$ of isotope A^N populating charge state q after having passed the stripper at energy E, and also on the transmission of the beam of A^N thru the high energy mass

spectrometer (that takes into account all the beam deflection and focusing devices, the *HE magnet* and the *HE ESAs*), given by $T_{HE}{}^{q}(A^N)$;

$$I^q(A^N) = I_P . c(A) . Y_{tot} . \alpha^-(P) . T_{LE}^-(P) . \beta_E^q(A^N) . q . T_{HE}^q(A^N) . \varepsilon(A^N) \quad (5)$$

Equation (5) is very useful in planning a measurement since it describes which beam intensity to expect for a trace isotope A^N present in a given matrix, in the detector chamber at the end of the AMS line.

4.3 Quantification

Precise quantification can be a very difficult problem to solve in both SIMS and accelerator SIMS or Micro-AMS. There are several factors in a measurement that can have an important effect on relative and absolute secondary ion yields. Some of these factors are the matrix effect, the surface coverage of reactive elements, the sample chamber pressure and the orientation of the crystallographic axes with respect to primary and secondary ion beams, the transmissions of the several focusing and deflection elements that take the secondary ions to the detector and the transmission through the accelerator itself. Because of this, most measurements made with AMS and Micro-AMS use standards. This is a limitation in many cases, however, since it is not always possible to get reliable standards.

Since measurements with standards are the norm in Micro-AMS, the quantification formalisms that will be introduced here presume the existence of such standards, that is, a sample identical to the sample to be analyzed, but with a known concentration of the trace isotope under study. It is important to refer that, for standard samples to be used as a quantification method, the standard sample has to be analyzed in the exact same conditions that the unknown sample.

Isotopic ratios, I_R, are many times used as final quantification results in AMS and Micro-AMS. They are dimensionless quantities that are very simple to calculate. They are very practical due to their simplicity and became the most used method for presenting results in AMS because, although they don't have units that can be easily translated into other physical quantities without further information from the particular experiment, most results presented in AMS come from a very small variety of type of sample and trace isotope in study. This means that when a AMS result of $I_R(^{36}Cl/^{35}Cl) = 3 \times 10^{-15}$ is presented to the AMS community, it is already assumed that it refers to a measurement of a high purity AgCl matrix (treated chemically as presented in chapter 5) with a trace amount of radioisotope ^{36}Cl, as is the case with routine AMS chlorine measurements, regardless of the scientific purpose of the measurement. This is true of the other small amount of routinely measured trace radioisotopes in AMS that compose more than 90% of all AMS measurements around the world (^{10}Be, ^{14}C, ^{27}Al, ^{36}Cl, ^{41}Ca, ^{129}I). So in most cases, AMS results are presented as:

$$I_R = \frac{I(T^N)}{I(T^K)}$$

where T^N is a trace radioisotope of matrix element T.

Of course, the isotopic ratio quantification method also presumes the use of standards. The "real" isotopic ratio in the unknown sample will be given by:

$$I_R = \frac{I_{Runknown} \cdot I_{RSTD}}{I_{R\ measuredSTD}}$$

where $I_{Runknown}$ is the measured isotopic ratio in the unknown sample, $I_{R\ measuredSTD}$ is the isotopic ratio measured in the standard sample and I_{RSTD} is the isotopic ratio known to exist in the standard sample previously to the measurement itself.

However, the scope of measurements made in Micro-AMS is expected to be bigger than the small amount of radioisotopes routinely measured in AMS. It will be usual to find in a Micro-AMS measurement a much wider range of matrices and trace elements, not only radioisotopes but also stable isotopes. Therefore, it is useful to introduce a method of quantification that provides a

final result in *atoms/cm*^{3}. This method that will be presented is a method usually used in SIMS and recurs to the so-called relative sensitivity factors.

If the three conditions previously presented for measurement with standards are met, then it is sufficient to measure the current of trace isotope T^N, belonging to trace element *T* present in the sample matrix, and the current of one of the isotopes of the sample's matrix, here called A^k belonging to sample matrix *M* ($M=A_iB_jC_k$), in order to determine the concentration of *T* in the sample, *n(T)*:

$$n(T) = \frac{I^q(T^N)}{I^q(A^K)} RSF_M^{T^N}(T^N)$$

n(T) is the concentration of *T* in the sample in *atoms/cm*^{3}. $RSF_M^{T^N}$ is called the relative sensitivity factor and its units are *atoms/cm*^{3}. It can be obtained using this equation and measuring the standard, where *n(T)* is known.

4.4 Primary beam's influence on the secondary ion currents

Several elements have been used as primary beam in SIMS since its beginnings, namely O^-, O_2^+, Cs^+, Xe^+, Ar^+, Ga^+ and many others [3]. This is due to the fact that different elements offer different advantages depending on the characteristics of the target sample and also on the purpose of the SIMS measurement itself. Two of the most used are oxygen and cesium, because both these elements tend to promote intense secondary ion currents in many elements and compounds: O^- and O_2^+ mostly in the case of targets composed of electropositive elements and Cs^+ in the case of electronegative elements. Noble gas elements are also used because they don´t react chemically with the sample material and are therefore preferable in cases where qualitative surface analysis is required [4]. Ga^+ is another frequently used primary ion since it can provide an increase in lateral resolution in certain measurements involving depth profiling [5].

In Micro-AMS, as in AMS, it is only possible to use negatively charged secondary ion beams, because of the accelerator´s positively charged terminal.

Therefore, all the different versions of Micro-AMS developed so far have used Cs^+ ions as primary beam, because these tend to produce higher negatively charged secondary ion currents.

The increase in the negative ionization probability, α^-, of sputtered atoms in the presence of cesium is related to the decrease in the target material work function, Φ (which is the energy necessary to remove an electron from a solid). There is not yet a model that can fully explain the difference in secondary ion currents of a given trace element in a given matrix produced experimentally, when that matrix is bombarded by cesium (or any other primary beam). There are several semi-empirical models, based on experimental data, that are successful in predicting the behavior of certain trace elements being sputtered with positive cesium from certain types of matrices. In 1978, Deline and coworkers [6,7] established that, for some matrices bombarded with positive cesium:

$$\alpha^-(S) \propto e^{-\Omega_T}$$

where Ω_T is the electron affinity of negative secondary ions. They also stipulated, based on experimental data, that, again for some matrices:

$$\alpha^-(S) \propto \left[\frac{1}{S_{1,M}}\right]^{x_S^-} \propto [n(Cs)]^{x_S^-} \qquad (7)$$

with

$$S_{1,M} = \frac{h}{t} \qquad (\mathrm{nm/s})$$

$S_{1,M}$ is called the sputter rate, defined as the amount of target material h being removed in nanometers per time unit. The exponent x_S^- is determined experimentally and varies from trace element to trace element. Relation (7) implies that the negative ionization probability and hence the secondary ion yield of negative ions produced by the Cs^+ bombardment, is proportional to the inverse of the sputter rate, which in turn is proportional to the concentration of cesium, $n(Cs)$ in the sputtering area. Table 4.1 shows some experimentally determined values for x_S^-.

element	B	C	P	As	Sb
x_S^-	2.1 ± 0.1	2.0 ± 0.1	2.4 ± 0.2	2.6 ± 0.1	3.4 ± 0.2

Table 4.1: Values of x_S^- for different trace elements in a Si matrix [3].

In tables 4.2a) and 4.2b) all elements (except rare earths) are shown along with their ionization potential, electron affinity and relative secondary mono-negative, mono-atomic beam intensities. These relative intensities are a normalization of the negative ion currents that Middleton and coworkers [8] obtained with a SIMS system, using a high intensity Cs^+ primary beam at energies close to the 10 keV used in this thesis. It is important to stress that their objective was to test several cathodes in order to maximize secondary ion negative currents for each element. This means that many of these values are not intensities produced from elemental targets but from target matrices composed of one or more elements besides the element in study. This use of multi-element matrices has two purposes; in certain cases, an elemental negative secondary beam is more intense when coming from a multi-element matrix than from a pure elemental target (see the case of lead measurements in chapter 5, where elemental lead samples were transformed into PbS, because this matrix provided more intense lead secondary beams in the form of PbS^- molecular ions). In other cases, higher molecular secondary currents are achieved by using a molecular negative ion containing the element in study, instead of elemental secondary currents. In any case all the secondary negative-ion relative beam intensities shown in tables 1a) and b) are of mono-atomic, mono-negative beams. These relative intensities, despite matrix effects, illustrate the relationship between electron affinity and secondary negative ion currents. They are an important reference when planning an experiment in Micro-AMS. These values are especially important for AMS, where the measurements are made using matrices prepared chemically with the goal of obtaining the most intense negative secondary current possible for a certain

element. In the case of Micro-AMS, where sometimes samples are not prepared beforehand, there are many times cases where a trace isotope may be measured in a matrix that may not include that element as a main constituent. In these cases, it is important to remember the matrix effect mentioned before. Using the example of silver; even if an elemental silver target produces an intense silver beam, a trace silver isotope in a carbon matrix, for instance, may not produce the equivalent intensity.

IA	IIA	IIIA	IVA	VA	VIA	VIIA	VIIIA
$_{1}$**H**	element						$_{2}$**He**
13.59	ioniz.potential						24.48
0.754	Elec. Affinity						0.078*
50	Rel. Intensity						-
$_{3}$**Li**	$_{4}$**Be**	$_{5}$**B**	$_{6}$**C**	$_{7}$**N**	$_{8}$**O**	$_{9}$**F**	$_{10}$**Ne**
5.39	9.32	8.3	11.26	14.53	13.61	17.42	21.56
0.618	0.195*	0.277	1.263	-0.07	1.461	3.399	< 0
3.5	0.1	20	50	-	37.5	75	-
$_{11}$**Na**	$_{12}$**Mg**	$_{13}$**Al**	$_{14}$**Si**	$_{15}$**P**	$_{16}$**S**	$_{17}$**Cl**	$_{18}$**Ar**
5.14	7.64	5.98	8.15	10.48	10.36	13.01	15.76
0.548	< 0	0.441	1.385	0.747	2.077	3.617	< 0
1	-	0.75	100	30	75	80	-
$_{19}$**K**	$_{20}$**Ca**	$_{31}$**Ga**	$_{32}$**Ge**	$_{33}$**As**	$_{34}$**Se**	$_{35}$**Br**	$_{36}$**Kr**
4.34	6.11	6.00	7.90	9.81	9.75	11.81	14.00
0.501	0.043	0.30	1.2	0.81	2.021	3.365	< 0
0.25	-	0.25	6	10	15	12.5	-
$_{37}$**Rb**	$_{39}$**Sr**	$_{49}$**In**	$_{50}$**Sn**	$_{51}$**Sb**	$_{52}$**Te**	$_{53}$**I**	$_{54}$**Xe**
4.18	5.70	5.79	7.34	8.64	9.01	10.45	12.13
0.486	< 0	0.3	1.2	1.07	1.971	13.059	< 0
0.125	-	0.3	3.5	2.5	4.5	37.5	-
$_{55}$**Cs**	$_{56}$**Ba**	$_{81}$**Tl**	$_{82}$**Pb**	$_{83}$**Bi**	$_{84}$**Po**	$_{85}$**At**	$_{86}$**Rn**
3.89	5.21	6.11	7.42	7.29	8.42	9.5	10.75
0.472	< 0	0.2	0.364	0.946	1.9	2.8	< 0
1	-	-	0.125	1	i.n.f.	i.n.f.	-

*metastable

$_{21}$Sc	$_{22}$Ti	$_{23}$V	$_{24}$Cr	$_{26}$Mn	$_{26}$Fe	$_{27}$Co	$_{28}$Ni	$_{29}$Cu	$_{30}$Zn
6.54	6.82	6.74	6.77	7.44	7.87	7.86	7.64	7.73	9.39
0.188	0.079	0.525	0.666	< 0	0.163	0.661	1.156	1.228	< 0
~ 0	0.15	2	1.25	-	2.5	15	25	30	~ 0
$_{39}$Y	$_{40}$Zr	$_{41}$Nb	$_{42}$Mo	$_{43}$Tc	$_{44}$Ru	$_{46}$Rh	$_{46}$Pd	$_{47}$Ag	$_{49}$Cd
6.38	6.84	6.88	7.10	7.28	7.37	7.46	8.34	7.58	8.99
0.307	0.426	0.893	0.746	0.55	1.05	1.137	0.557	1.302	< 0
	0.075	0.5	0.1	0.15	1.5	2.5	0.35	12.5	~0
$_{57}$La	$_{72}$Hf	$_{55}$Ta	$_{74}$W	$_{75}$Re	$_{76}$Os	$_{77}$Ir	$_{79}$Pt	$_{79}$Au	$_{80}$Hg
5.58	7.0	7.89	7.98	7.88	8.7	9.1	9.0	9.22	10.44
0.5	~ 0	0.322	0.815	0.15	1.1	1.565	2.128	2.309	< 0
~ 0	~ 0	0.125	0.5	0.15	4.5	15	75	80	-

Table 4.2a) Each Square is filled with the name of the element and atomic number on top, followed by the ionization potential, the electron affinity of the element and the relative intensity of the elemental mono-negative secondary ion current produced by bombardment with a Cs^+ primary beam. The values presented in the tables for the relative intensities are a normalization of the experimental secondary ion intensities, produced under Cs^+ bombardment, measured by Middleton and coworkers and presented in his Negative Ion Cookbook [8], where the details of each individual measurement are described.

The ionization efficiency values presented here were also taken from Middleton's Negative Ion Cookbook, where they are defined as the percentage of negative ions of all the sputtered particles.

i.n.f. means information not found.

Table 4.2b) The same principle of construction of table 4.1a) was applied to the construction of table 4.2b) but in this case for transition elements. Rare earths were not shown here, as these tend to produce very weak elemental secondary negative ion beams.

References

[1] P. Sigmund, (2006). Particle penetration and radiation effects, Springer Series in Solid-State Sciences, Vol. 151 (Springer, Berlin).

[2] P.Sigmund, PSP Review Volume 2011

[3] Benninghoven, A., F.G. Rüdenauer, and H.W. Werner, 1989. "Secondary Ion Mass Spectrometry", John Wiley & Sons.

[4] K. Wittmaack, Surface Science Volume 90, Issue 2, 2 December 1979, Pages 557–563

5

Tests and applications

During the testing of the implementation of the system, several targets producing different beams were used in order to try to attest the quality of the measurements compared with what had been previously achieved at CSIRO. Among the several different samples used, which included beryllium oxide and nitride to produce ^{9}Be and ^{10}Be, pure gold that produced ^{197}Au, pure aluminum metal or aluminum oxide, manganese, strontium, osmiridium targets that produced Os and Ir, by far the most used were the galena targets. These produced secondary beams prolific in sulfur and lead, which was extracted from the target mainly as PbS^{-}. As a test, the sulfur isotopic ratios were measured and compared with known published values. These were also used to test the precision that could be achieved with the system.

One of the main preoccupations in the testing of any samples in the Micro-AMS system is to keep the target chamber as clean as possible, and to avoid contaminations of the chamber electrodes from any of the sample material. The chamber and ion source were cleaned several times during the duration of the work in this thesis.

5.1 Lead isotopic measurements

As mentioned before, galena crystals were the principal targets used in all the tests performed during the reassembling of the system. These were used mainly to produce sulfur isotopes but lead isotopic ratios had also been obtained for testing the system in the high mass range. This experience with galena samples was valuable when a proposal came from archeologists to try to apply the Micro-AMS system at LATR/CTN-ITN to determine provenances of lead samples from ancient anchors. The lead samples had been extracted from different ancient anchors found in several archeological sites in the Portuguese coast including Peniche, Setúbal, Sesimbra, Faro, Portimão, Sines e Cascais.

5.1.1 Lead provenance studies

The principle of lead provenance studies is based on the assumption that different geological lead deposits around the world have specific lead isotopic ratio signatures which do not change when the lead is transformed into different sorts of man made objects. This means that it is possible to know where the lead of a certain artifact came from independently of the object's age or fabrication procedure.

Lead has four isotopes; ^{204}Pb, ^{206}Pb, ^{207}Pb and ^{208}Pb. These isotopes were present at the time of the earth's formation, which would make one suppose that anywhere on earth lead would have the same relative proportion of isotopes, identical to the lead isotopic ratio present at the beginning of the earth. Instead only the ^{204}Pb isotope exists in the same amount as at the time of earth's origin. This is because besides the original amount of ^{206}Pb, additional amounts of this isotope were produced by radioactive decay of the uranium isotope ^{238}U ($t_{1/2}$= 703.8 Ma). A similar process altered the initial amount of ^{207}Pb, in this case by the decay of ^{235}U($t_{1/2}$= 4.468 Ma) and with ^{208}Pb by decay of the thorium

isotope ^{232}Th($t_{1/2}$= 14.01 Ga). As a consequence, the lead isotopic composition at any given time anywhere on earth should be the initial lead isotopic ratio plus the amounts of the three isotopes that are produced at the rate of the radioactive decays of the uranium and thorium isotopes. This present expected isotopic ratio was calculated based on the lead isotopic ratio of meteorites (which should be the same as the ones at the beginning of the earth) and the known amounts of lead, uranium and thorium present in the earth's mantle and assuming that these are homogenous reservoirs, and using the known decay rates of uranium and thorium. This calculation is part of the two-stage Stacey-Kramers model [1].

However, the earth is composed of different geologic reservoirs that emerged from the mantle at different times and that contain different amounts of U, Th and Pb. This means that different reservoirs in different locations can have very different lead isotopic ratios so that, when a mineral incorporates lead in its crystal structure, it acquires the lead isotopic signature of its parent reservoir. If the mineral incorporating lead lacks U and Th, as is the case of copper, lead and silver sulfides and their derivatives, carbonates and hydroxides, the lead isotopic ratio of its parent reservoir will be preserved in time [2]. This lead isotopic ratio is not altered by superficial chemical reactions on the mineral containing lead, nor by smelting to metal [3] or subsequent corrosion.

It is based on this assumptions that lead provenance studies were developed in the 1960's by Brill [4] with the goal of applying them to archeological studies. It assumes that ore deposits can be clearly distinguished from each other, that is, that the variation in a certain ore deposit is smaller than between two different deposits. By plotting the isotopic ratios $^{207}Pb/^{204}Pb$ vs. $^{206}Pb/^{204}Pb$ or other combinations of isotopes a unique signature for a particular reservoir can in principle be achieved. An example of such a plot is shown in figure 5.1.

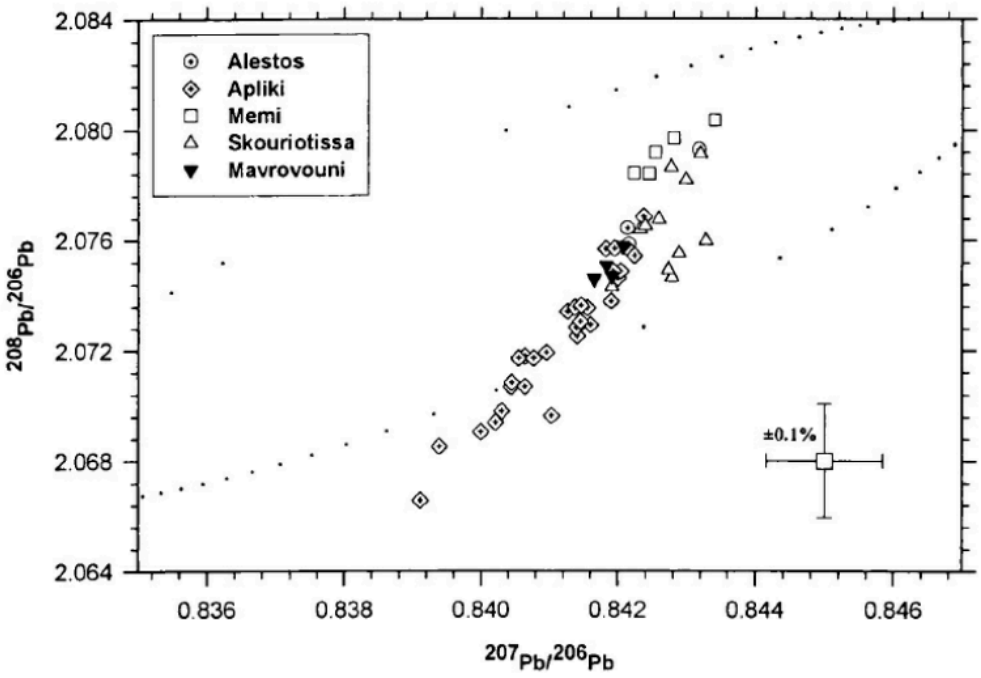

Figure 5.1: Plot of $^{208}Pb/^{206}Pb$ vs. $^{207}Pb/^{206}Pb$ for several copper ore deposits in Cyprus [5].

This approach has yielded very interesting results in the study of many ancient copper, lead and silver artifacts [6].

5.1.2 How to measure the lead isotopic ratios

The determinant factor in lead provenance studies is the achievable precision of the measuring system. This is due to the fact that lead isotope signatures belonging to different ore deposits can, in many cases, have differences only in the third or fourth decimal place.

For this reason, TIMS (thermal ionization mass spectrometry) and ICP-MS (inductive coupled plasma mass spectrometry) are the techniques commonly used for provenance studies, with ICP-MS precision in the 0.1% or better range and TIMS precision below 0.01%. Such precision values are unattainable with Micro-AMS, nor any other ion beam technique. Still, recent attempts were made to use SIMS in this kind of studies [7].

The reason for this is that the use of an ion beam technique like SIMS or Micro-AMS can widen the amount of samples that can be studied, since ICP-MS and TIMS have the disadvantage of demanding a chemical extraction of the lead from the original sample thereby destroying the sampled material. With an ion microprobe small bits of the original object, or in some cases the whole object, can be loaded directly into the chamber and analyzed both spatially and in depth. This could in some cases be useful and could justify a loss in precision.

Still it is necessary to achieve the best possible precision.

5.1.3 Considerations regarding precision and accuracy in Micro-AMS

The first consideration regarding precision has to do with statistical precision. Statistical precision is not a problem when the isotopes in study have high concentrations in the matrix and their sputtering yields for that matrix are relatively high. In such cases, the count rates in the detector will be high enough to keep statistical uncertainty low. But it can become the limiting factor in AMS trace isotope studies, in terms of achievable detection limits with a reasonable accuracy (better than 10%). It can be even more so in the case of Micro-AMS since having a micro-beam means having much less intensity of primary and consequently secondary beam on the one hand and less available material to remove from the sample on the other, since the beam spot is much smaller, and it is convenient to keep the depth of the sputter crater below the value of the beam spot diameter.

In order to understand the dependence of the statistical uncertainty on available amount of sample material, data collection time and primary beam intensity and diameter, it is useful to refer to the well-known example of ^{14}C AMS measurement as mentioned in [8].

5.1.3.1 Statistical uncertainty vs available amount of sample

The statistical uncertainty will be given by the square root of the total number of counts of the isotope being measured in the detector. If a statistical uncertainty of 1%, within 1σ, is desired, then the total number of particles reaching the detector and being counted by it has to be 10^4.

Recurring to the radiocarbon example mentioned above, it is known that, for a regular radiocarbon measurement using a tandem accelerator at 2MV terminal voltage, for a modern graphite sample containing an isotopic ratio of $^{14}C/C = \sim 10^{-12}$, there will be 2 particles per second count rate in the detector for each μA of C^- injected into the accelerator. Considering that the maximum available ionization yield for graphite is around 8%, this means that to produce these 2 counts/s in the detector, the minimum amount of carbon in the graphite sample will be around 10^{-6} mol. This amount of carbon corresponds to a sample volume of around $V_{min} \approx 5 \times 10^6\ \mu m^3$. This minimum volume of carbon necessary to achieve a 1% statistical precision determines also the minimum micro-beam diameter, $d_{microbeam}$:

$$d_{microbeam} \approx \sqrt[3]{V_{min}}$$

since the depth of the sputter crater should not be greater than its diameter.

From this example it is possible to extrapolate the amount of sample required for an analysis of an isotope, occurring at a given concentration in that sample, with a certain statistical accuracy. For higher beam diameters, higher amounts of material will be available and hence better statistical accuracy will be attainable, or better detection limits.

5.1.3.2 Statistical accuracy vs measurement time vs microbeam diameter

In the above example, only the amount of sample required for a microbeam AMS analysis with a certain statistical accuracy was calculated.

However, it is also important to take into account the time necessary for such measurements, for there is a time limit after which a measurement becomes impractical. Besides that, the beam diameter, as was seen, will also play a part in the calculations and will therefore be taken into account with more detail.

For a primary Cs^+ current of ~ 100 μA, focused to 0.3 mm of diameter, there will be a primary beam density of ~ 140 mA/cm^2 if beam aberration is kept at a minimum. If the primary current is 1 μA, then the beam diameter, again in perfect focusing conditions, where there are no beam aberrations effects, should be able to be reduced to about 30 μm.

Continuing with the example of the graphite sample; with a concentration of ^{14}C around 10^{-12}, and if we assume a ionization yield of 10%, there will be 10 times more primary beam Cs^+ current than all the negative current extracted from the sample.

This means that the 1 μA Cs^+ micro-beam will yield a secondary beam of 0.1 μA. For a 1% statistical accuracy (10^4 ^{14}C particles counted in the detector) the measurement time will be around 50000 s (almost 14 h!), which is not a reasonable measurement time for several reasons, one of which is that the depth of the crater would go far beyond the diameter of the beam. If we reduced this time to a much more realistic measurement time of 60 s, and maintaining the same beam diameter, the minimum measurable concentration of ^{14}C to C will be one of $^{14}C/C = 10^{-9}$. In order to improve the detection limit by one order of magnitude, a time of 600 s would be needed, although this would mean a crater depth higher than the beam diameter. In such a case, the beam diameter would have to be increased or, keeping the beam diameter, the beam would have to be scanned across the sample.

5.1.3.3 Standard deviation of measurements or overall accuracy of a measurement

AMS and Micro-beam AMS results are usually presented as isotopic ratios. In AMS these are usually the number of counts per second in the detector of a trace radioisotope divided by the number of counts per second in the detector of a stable isotope (usually of the same element of the radioisotope). The difference in count rate between the two isotopes is usually more than 10 orders of magnitude. In Micro-beam AMS, where stable isotope measurements are more frequent, the difference in count rate between isotopes is usually not so high.

In any case both isotope's count rate has to be measured, ideally in the exact same conditions. In order for them to be measured in the same conditions, they are injected into the accelerator simultaneously or in rapid sequence, depending on the type of injection system used. This is done because of several sources of instability in the system that can affect the count rate of each isotope differently if they are measured at different times. By injecting them simultaneously or almost so, the instabilities will affect each isotope's count rate in the same way and therefore be nullified in the isotopic ratio calculation. The instabilities come from instabilities in the source's primary current, beam transport system (where each of the HV power supply units feeding the different focusing and deflecting devices can suffer from instabilities in their current and voltage outputs), accelerator terminal voltage and magnet currents. These will affect directly the standard deviation of the isotopic ratios measured in time, as these are measured sequentially. The larger the time interval between two isotope’s count rate measurement the larger the effect of these random instabilities on the standard deviation of the isotopic ratios measured.

If, as in the case of some of the measurements in this thesis, the isotopes are to be injected sequentially into the accelerator, the computer program controlling the bouncing system, responsible for the bouncing of the different beams so that they are injected sequentially, will allow the user to reduce the time of measurement of each isotope to tenths of milisecs.

5.1.4 The problem of accuracy when measuring lead isotopic ratios in pure lead targets

From the past experience with galena targets there was confidence that a good precision could be obtained with lead isotopic measurements, provided that a reasonably pure lead secondary current could be extracted from the pure lead matrix. As mentioned before, due to the so-called matrix effects, sputtering yield depends on the constitution of the matrix. In the case of the galena targets, lead had been injected into the accelerator in the form of PbS^-, whose peaks in the Le magnet mass spectrum were much more intense than the pure lead peaks.

It rapidly became clear that the low sputtering yields of lead from metallic lead would impose a limit on the obtainable accuracy. That led to the decision to transform the lead samples into lead sulfide, and again use the lead sulfide peaks instead of the pure lead ones. Of course this meant that a spatial analysis would no longer be possible since the sample would be altered, but the microbeam would still be useful in attesting the homogeneity of the transformation of lead and sulfur to lead sulfide.

5.1.5 Chemical preparation of the lead samples.

The lead samples were transformed into lead sulfide using the following process; sulfur was added to the lead sample after being weighted so that its weigh would make the mixture stoichiometrically 1:1 (S,Pb). These were placed in a quartz tube and sealed. After sealing the tubes were introduced in an oven that was heated up to 1200ºC for 8 hours. After this, the lead sulfide was removed from the quartz and mounted on a steel disc. Overall, 5 samples from 4 different archeological locations and the NIST standard went through the same process.

5.1.6 Results

The tandem was operated at 2MV terminal voltage. Two samples were measured and a NIST standard, the SRM 981, all three of which had been transformed from pure lead to lead sulfide. The $^{207}Pb/^{206}Pb$, $^{208}Pb/^{206}Pb$, $^{204}Pb/^{206}Pb$ isotopic ratios were measured for the three samples and then normalized to the standard for absolute value.

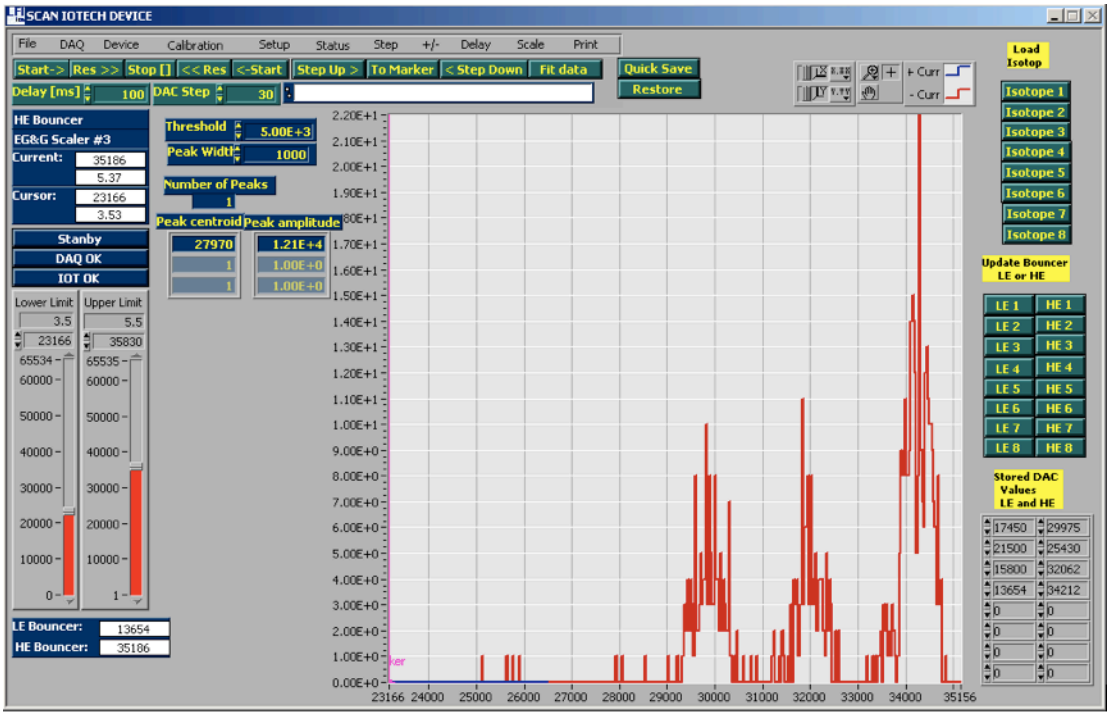

Figure 5.2: Scan Iotech device control program.

This labview program belongs to the Tandem Control Program that was designed to allow for the control of the Micro-AMS system. This particular program, called Scan Iotech (see chapter 3), controls the voltages on the bouncing system. In this plot it is visible the four lead isotopes; ^{204}Pb, ^{206}Pb, ^{207}Pb and ^{208}Pb (respectively seen from left to right). The x-axis is voltage (converted to DAC values), applied in this case to the plates of the high-energy bouncing system and the y axis represents counts/s in the particle detector.

Several tests of reproducibility were performed. This was important given the fact that it was hard to mount the PbS samples, because they tended to fragment when being removed from the silica tubes. The larger fragments were mounted on stainless steel discs with 25 mm diameter using carbon tape. In this mounting procedure it was important to make sure that the PbS fragments were mounted so that the beam would hit a plane and uniform surface. All samples were mounted so as to be at the same distance to the target plate plane.

The results presented in table 1 correspond to measurements of 20 runs with 20 cycles per run, using a count time per cycle in each isotope of 100 ms. The standard deviation presented in table 1 corresponds to the standard deviation of the average of the isotopic ratios calculated using the accumulated events of each run, that is, the scan bouncer program automatically adds the number of counts per isotope during the 20 cycles of each run and at the end of each run calculates the isotopic ratios; $^{207}Pb/^{206}Pb$, $^{208}Pb/^{206}Pb$, $^{204}Pb/^{206}Pb$. As the runs progress it plots a graph with the three isotopic ratios. Simultaneously, it calculates the average of the isotopic ratios in the runs so far and the corresponding standard deviation. The values shown in table 5.1 correspond to the average of the 20 runs and corresponding standard deviation.

	$^{207}Pb/^{206}Pb$	s.d	s.d. (%)	$^{208}Pb/^{206}Pb$	s.d	s.d. (%)	$^{204}Pb/^{206}Pb$	s.d	s.d. (%)
SRM 981	1.005	0.005	0.50	2.263	0.01	0.44	0.0350	0.0004	1.14
sample 1	0.945	0.02	2.1164	2.314	0.04	1.73	0.0279	0.0007	2.51
sample 2	0.9418	0.005	0.5309	2.179	0.02	0.92	0.0403	0.0004	0.99

Table 5.1: Results from the measurement of the SRM 981 NIST standard and two test samples beloging to two different anchors. Besides the isotopic ratios also the standard deviation is presented both in absolute value and in percentage.

The values can then be normalized to the standard in order to get an absolute value for the three isotopic ratios. These normalized values and corresponding uncertainties are presented in table 5.2.

	$^{207}Pb/^{206}Pb$	uncertainty	$^{208}Pb/^{206}Pb$	uncertainty	$^{204}Pb/^{206}Pb$	uncertainty
SRM 981 published	0.91464	0.00033	2.1681	0.0008	0.059042	0.000037
sample 1 normalised	0.860	0.001	2.22	0.04	0.0471	0.0008
sample 2 normalised	0.857	0.004	2.09	0.04	0.07	0.02

Table 5.2: The NIST standard values shown are the ones published by NIST. These values and their uncertainties were used to calculate the absolute values for the isotopic ratios of samples 1 and 2.

5.1.7 Conclusions

As can be seen from table 5.1 the standard deviation was above expected. This is probably due to problems related to the mounting of the samples and perhaps some instability in the beam transport system. At this level of accuracy it is not possible to attribute a definite location for the ore deposits in Europe or north Africa, that are the regions in antiquity where lead was extracted. It is however, if some improvements to the beam transport system are made, possible to distinguish European deposits from American ones which could be useful in studies involving more recent objects.

5.2 AMS analysis of low dose Pt implantation in Si

5.2.1 Introduction

The use of isotopic pure materials, eliminating the inhomogeneous isotope broadening observed in natural samples, has resulted in large improvements of the spectral resolution of a number of impurity and defect spectroscopies. In highly enriched ^{28}Si the no-phonon transitions can become so sharp that centers having different numbers of specific isotopes can be resolved as 'isotopic fingerprints', showing not only that a given element is involved but also how many atoms of that element are present in the binding center.[9-11]

Low-dose implantations have found a number of growing applications, namely for the optical studies, where different isotopes are implanted. Although in some previous studies Au has been used, using the stable isotope

and a radioactive one, Pt with several stable isotopes seems to be an interesting probe to study these effects. However, to be sure about the interpretation of the optical data, the isotopic ratio of the implanted isotopes must be known with high accuracy. In addition ion implantation, with its ability to do isotopic selection, has been recognized for many years as an important technique for the surface modification of materials with consequent improvement of its properties

In this study, pure ^{28}Si isotope single crystals were implanted, at an energy of 60 keV with different Pt isotopes (^{194}Pt and ^{198}Pt), being the nominal fluence for each of the isotopes around $1x10^{14}$ atms/cm^2. A natural Pt target was used for the implantation and despite the mass selection, some isotopic contamination is expected. Due to the low fluences implanted the determination of the implanted isotopic ratios requires an analytical technique with high sensitivity such as Accelerator Mass Spectrometry. In particular Microbeam AMS allows the characterization without any kind of chemical preparation of the implanted samples, measuring the implanted isotopic ratios and determining the amount of the ^{195}Pt and ^{196}Pt contamination. Furthermore the profile distribution of the isotopes was determined as function of sputtering time. This is one of the first applications where this possibility was clearly demonstrated.

5.2.2 Experimental details

The targets consisted of polished high purity ^{28}Si substrates implanted with a very low fluence ($1x10^{14}$ atm/cm^2) of ^{194}Pt and ^{198}Pt isotopes. The implantation was done by the Danfysik 1090 series high-current implanter at the CTN-ITN Lab, with a current of 1 mA at 60 keV beam energy. Care was taken, by reducing the slit apertures, to minimize contamination by the other naturally occurring platinum isotopes (^{195}Pt and ^{196}Pt) present in the platinum cathode.

For the beam optics optimization a high purity platinum powder compressed into a hole in a steel disk was used. This was done because the platinum currents extracted from the Si targets were too low to assure an

optimum beam transmission setting. Current intensities at the high energy side of around 50 pA for the +4 charge state of the different isotopes were obtained. After the beam optimization process, the Pt implanted Si target was sputtered during several hours in different points. Besides the above-mentioned target, a blank was also used to measure the platinum background in the system. The blank was a non-implanted polished Si target identical to the original one.

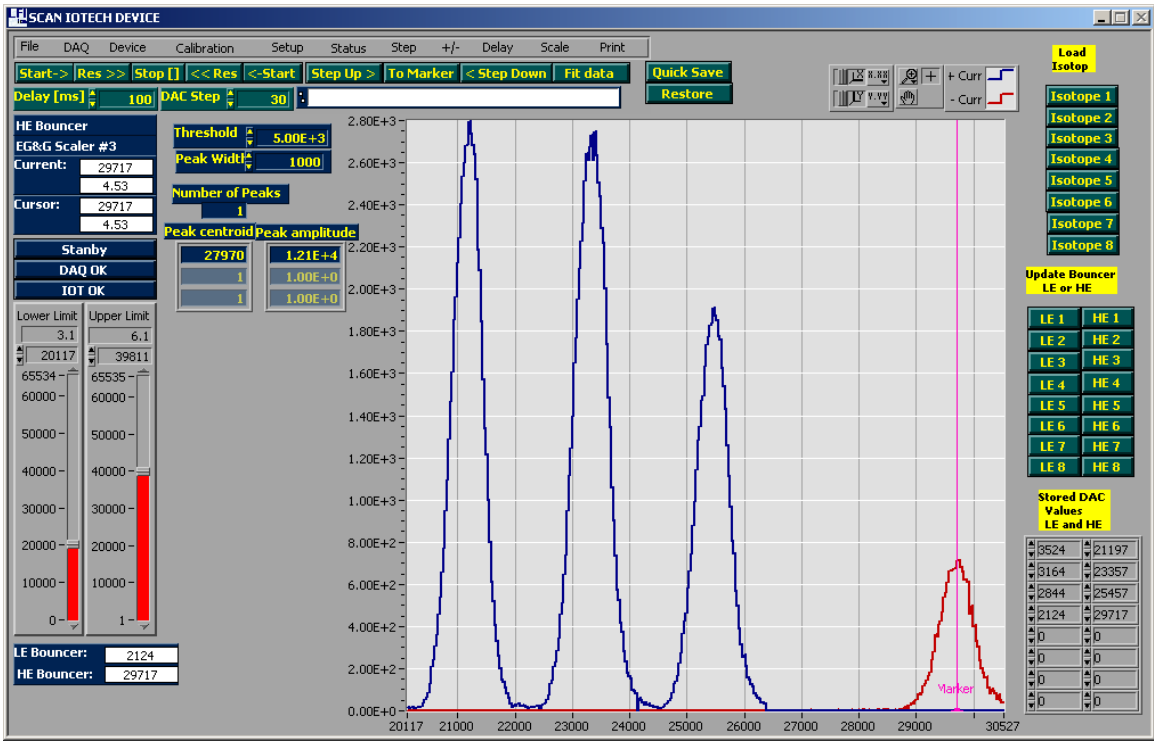

Figure 5.3: High energy bouncer scan with the four platinum isotopes; ^{194}Pt , ^{195}Pt , ^{196}Pt and ^{198}Pt as measured in the platinum powder target used to produce the pilot beam. The chosen charge state was 4+. The yy axis units are counts/s and the xx axis are DAC values.

5.2.3 Results and discussion

At the end of the beam optimization process, the bouncer scan of the four different isotopes for the platinum powder target was used to determine the isotopic ratios as measured at the end of the AMS line. The intensity of the different isotope peaks depends on the optical transport system due to beam

optics mass fractionation. Because of this, the beam was optimized using the ^{196}Pt peak since this peak occupies the central position in terms of mass thus allowing for the most balanced optimization. The high-energy mass spectrum obtained from the pilot sample is shown in figure 5.3.

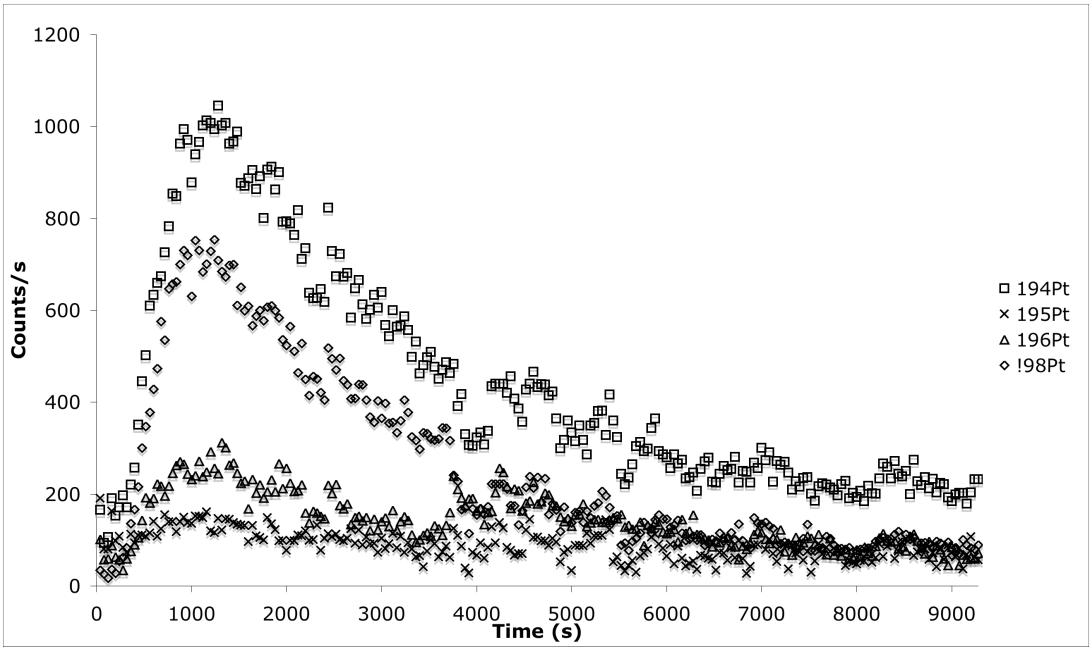

Figure 5.4: Beam intensities of the different isotopes measured in the PIPS detector as a function of erosion time of the sample.

The measured isotopic ratios were found to be 0,994±0,005 for ^{195}Pt/^{194}Pt, 0,714±0,003 for ^{196}Pt/^{194}Pt and 0,1669±0,0006 for ^{198}Pt/^{194}Pt. The correspondent natural abundance ratios are, respectively, 1.026, 0.766 and 0.217. These values were used to do the fractionation correction found in figure 5.5.

After the optimization the blank was put on the target holder, and measured for about twenty minutes. It showed there was a constant platinum contamination in the system that gave an average of 133 counts/s for ^{194}Pt, 131 counts/s of ^{195}Pt, 111 counts/s of ^{196}Pt and 26.2 counts/s of ^{198}Pt. This contamination was probably due to the Pt powder target used to produce the pilot beam as the relative intensities of the different isotopes in the blank are close to the isotopic beam intensities found in that target. As this contamination

proved to be constant in time we subtracted it to the measured values for the implanted target.

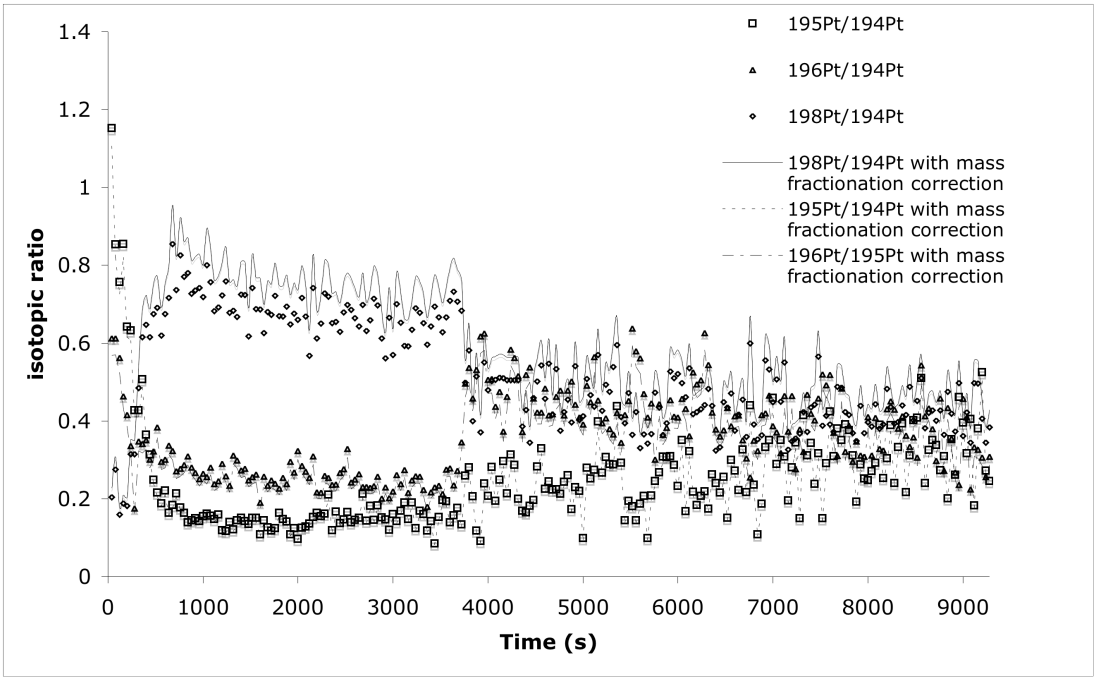

Figure 5.5: $^{195}Pt/^{194}Pt$, $^{196}Pt/^{194}Pt$ and $^{198}Pt/^{194}Pt$ isotopic ratios as a function of erosion time of the sample. The separate points correspond to the isotopic ratios calculated directly from the measured values in the detector. The lines correspond to the same ratios calculated taking in account the beam optics mass fractionation as estimated from the Pt powder target.

The implanted Si target was tested in several points and determined to be homogenous in terms of the relative amounts of the implanted isotopes. The plot in figure 5.4 shows the beam intensities in counts per second measured with the PIPS detector for the different platinum isotopes versus time of erosion of the implanted sample, which can be seen as a depth profile of the sample in one point. These values were used in figure 5.5 to plot the isotopic ratios along the same time. During the first minutes it is evident the Pt contamination with ratios close to the natural ones, but as the beam reaches the implanted depth, the ratios become quite different. Also the intensity of the ^{198}Pt beam is less than that of the ^{194}Pt beam along the implanted depth of the target; 0.76±0.06 for the $^{198}Pt/^{194}Pt$ ratio. This is unexpected since the implanted fluence was the same for both isotopes. Such a discrepancy can be only partially explained by mass

fractionation by the beam optics as can be seen by the mass fractionation corrected plot in figure 5.5.

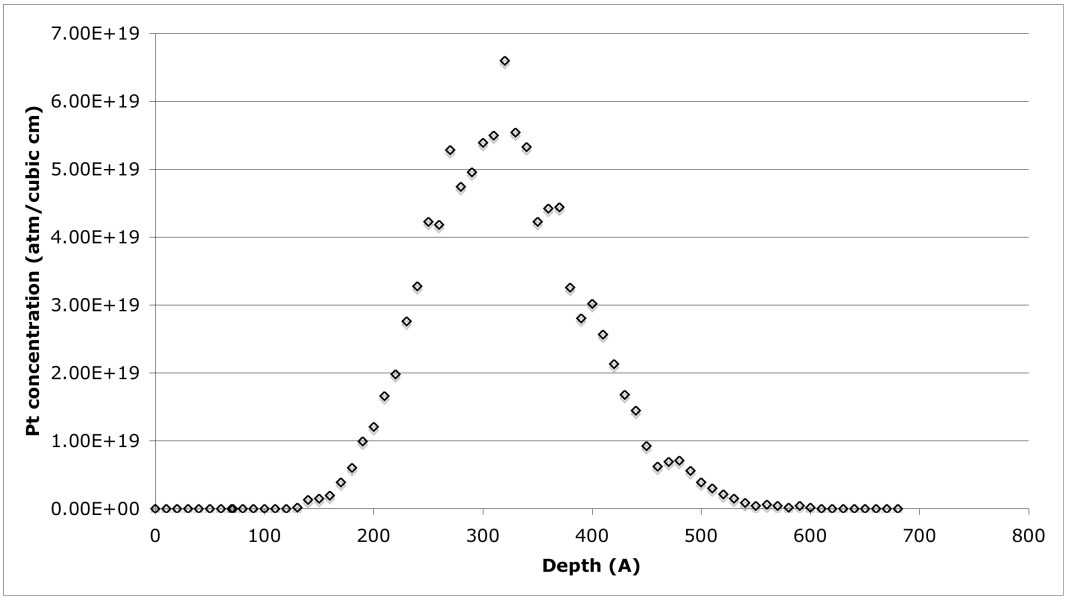

Figure 5.6: Depth profile of the implantation calculated by the TRIM program.

Furthermore the depth profile does not follow the SRIM profile shown in figure 5.6. This is due to a lack of homogeneity in the primary beam, which resulted in an uneven depth profiling. This was confirmed by the optical microscope analysis of the sample after its exposure to the beam.

Another objective of this experiment was to assess if there was some contamination by the ^{195}Pt and ^{196}Pt isotopes present in the cathode during implantation. As can be seen by both figure 5.4 and 5.5 these isotopes are present throughout the depth of the sample even when the background is subtracted, thus confirming that this contamination occurred, in ratios to ^{194}Pt equal to 0.14±0.03 for the^{195}Pt/^{194}Pt ratio and 0.24±0.03 for the ^{196}Pt/^{194}Pt ratio. The higher level of contamination of the ^{196}Pt isotope when compared to the contamination by the ^{195}Pt isotope, can also help to account for the lower than expected ^{198}Pt /^{194}Pt ratio since the ^{196}Pt isotope would have been implanted mainly alongside the ^{198}Pt isotope and the ^{195}Pt isotope would have been implanted primarily with the ^{194}Pt isotope.

It is important however to stress that there were no standards available for this measurement. As such, the values mentioned above are direct measurements and are not the absolute values for these isotopic ratios present in the sample. However, by taking information from the powder platinum target, we attempted to correct some visible beam transport optical fractionation. The platinum powder target cannot, however, be used as a standard for the reasons explained in the previous chapter (matrix effect).

References

[1] J.S. Stacey, J.D. Kramers, Earth and Planetary Science Letters Volume 26, Issue 2, June 1975, Pages 207–221

[2] Gale, N. H., and Stos-Gale, Z. A., 1982, Science, 216,11–19.

[3] Cui J., WU X., Archaeometry 53, 1 (2011) 205–214

[4] Brill, R. H., and Wampler, J. W., 1967, American Journal of Archaeology, 71, 63–77.

[5] Stos-Gale et al. Archeometry, 39, 1 1997, 83-123"

[6] Gale, N. H., and Stos-Gale, Z. A., 2000, 503–84, Chemical Analyses Series 155,

[7] Yeung C.S.L. et al, Surf. Interface Anal. 29, 487–491 (2000)

[8] S.H. Sie et al. Nuclear Instruments and Methods in Physics Research B 123 (1997) 112- I21

[9] M. L. W. Thewalt et al., Physica B 401-402 (2007) 587.

[10] A. Yang et al., Physica B 401-402 (2007) 593.

[11] M. Steger et al., Phys. Rev. Lett. 100, 177402 (2008).

6

Chlorine measurements

6.1 Introduction

This chapter is dedicated to the study of nuclear reactions that produce the radioisotope ^{36}Cl ($t_{1/2}$=3.01x10^5 a) using the LATR/CTN-ITN Micro-AMS system. The position of this radioidotope in the table of isotopes can be seen in figure 6.1. At the center of this study is the measuring of nuclear reaction cross sections by the determination of the number of ^{36}Cl (in the sample after irradiation) produced by a nuclear reaction. This method is usually called an offline measurement, as opposed to an online measurement, in which the products of the reaction are measured as it takes place (usually by measuring radiation or particles produced by the reaction, with a detector).

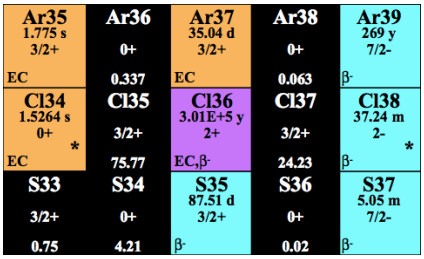

Figure 6.1: ^{36}Cl shown in the table of isotopes with its "surrounding neighbor" isotopes.

Chlorine measurements are one of the most common in AMS. They are used mainly in environmental studies but have also other applications. It is, however, at least to our knowledge, the first time that chorine measurements were performed using Micro-AMS. The main reason for its usage was to attempt to use the depth profiling capabilities of the Micro-beam to measure cross sections for a range of energies, directly in one single sample after one irradiation by protons or deuterons at a single energy. The nuclear reactions to be studied by this method are $^{37}Cl(p,d)^{36}Cl$ and $^{35}Cl(d,p)^{36}Cl$. This is in theory possible since the 10 MeV to 20 MeV protons and deuterons (which is the range of energies that are astrophysically relevant) will lose its energy along the depth of the AgCl targets, creating an "excitation function" inside the target until they stop. By doing a depth profile of the irradiated area, it should be possible to reproduce the ^{36}Cl production rate vs. energy along the depth of the sample.

This is an ambitious project that proved very hard to complete in the time of this dissertation thesis. It is nevertheless ongoing and FCT funding has been attributed to it.

In order to complete the work for this dissertation in a reasonable time span, only the results pertaining to the $^{35}Cl(n,\gamma)^{36}Cl$ and the development work that went into the preparation of the measurements of this reaction will be presented. The neutron irradiation of the AgCl samples was performed at the CTN-ITN Portuguese National Reactor.

The astrophysical motivation behind the study of the $^{37}Cl(p,d)^{36}Cl$ and $^{35}Cl(d,p)^{36}Cl$ reactions will be introduced nonetheless, because the results here presented for the $^{35}Cl(n,\gamma)^{36}Cl$ reaction are part of that research project, and were fundamental for the ongoing measurement of the two reactions. The $^{35}Cl(n,\gamma)^{36}Cl$ results were very important because they allowed for the testing of the quality of the developments, made in the context of this thesis, in the LATR/CTN-ITN Micro-AMS line in order to allow it to perform quality AMS measurements with chlorine. Also, this tests with the $^{35}Cl(n,\gamma)^{36}Cl$ are scientifically relevant in themselves as they allowed for the measurement of the cross section of neutron capture of thermal neutrons by ^{35}Cl and its comparison with previously published values.

6.2 Astrophysical motivation for the measurement of nuclear reactions producing ^{36}Cl

The motivation for measuring cross sections of nuclear reactions producing ^{36}Cl lies in the field of astrophysics that studies the origin and formation of the solar system. ^{36}Cl is one of the short-lived radionuclides (called SLR's for abbreviation), thus named because of their short half-lives (~1 Ma), whose abundances in the early stages of the formation of the solar system are much higher than expected from the galactic background. These SLR's are ^{7}Be ($t_{1/2}$ = 53 d), ^{10}Be ($t_{1/2}$ = 1.4 Ma), ^{26}Al ($t_{1/2}$ = 0.74 Ma), ^{36}Cl ($t_{1/2}$ = 0.3 Ma), ^{41}Ca ($t_{1/2}$ = 0.1 Ma), ^{53}Mn ($t_{1/2}$ = 3.5 Ma) and ^{60}Fe (2.6 Ma), and are known to have been present in the early stages of the solar system through the presence of their daughter isotopes in CAIS (calcium and aluminum rich inclusions) and chondrule present in chondrites, which are the most common form of meteorites found on earth. These structures are thought to be amongst the oldest solid material present in the solar system, and they can provide important information about its formation.

There are several hypothesis that may explain such a high presence of those SLR's in the early solar system; one hypothesis, which has been highly debated [1], attributes these high abundances to the injection of material from a nearby supernova explosion, another hypothesis claims that they could have been produced by highly energetic protons and helium atoms in the accretion disk itself. It is very important to know the mechanisms that produced these SLR's because such mechanisms and their timings can impose important constrains to the models of the formation and evolution of the early solar system and thus provide valuable insight about that period, namely early solar system chronology, planetesimal heating, the astrophysical context of our solar system birth, and irradiation processes in the protoplanetary disk.

6.2.1 The beginnings of the solar system and meteorites

The solar system is thought to have begun as a giant molecular cloud composed mostly of hydrogen, which, due to its gravitational instability, developed into smaller agglomerates of matter. These smaller, denser agglomerates, eventually collapsed gravitationally, most of them becoming stars with disks of gaseous material orbiting around them. One of these stars, and corresponding gaseous disk, eventually evolved into the present solar system.

This star-orbiting disk is called a proto-planetary disk because under certain circumstances, which are not entirely understood, some of the matter in this disk will eventually produce planets. The proto-planetary disk is an accretion disk, which means that it is made of material that orbits the star in a spiral like path where most of the material in the disk is constantly being fed to the magnetic poles of the forming star, as well as aggregating into bigger and bigger structures of matter.

This disk is initially very hot, but as some of the initial gravitational energy starts to dissipate, some of its material starts to cool and solidify and some of this solid, rocky material starts to agglomerate and form planitesimals, initially small (1 km or less) but that, gradually, accrete into bigger and bigger bodies. The accretion process eventually results, after several millions of years, in the formation of a few earth-sized bodies orbiting the star.

Some of the material that was present at these early stages of the formation of the solar system was preserved in the form of chondrules and CAIS in chondrites, present in meteorites [2].

Meteorites can be divided into three main groups; stony meteorites, which account for 94% of all the observed falls of extraterrestrial material on earth; irons, that represent 5% and are believed to be in their majority remnants of core material from planitesimals or large asteroids, and stony-iron, which represent 1% of observed falls and are thought to come from a mixture of core and mantle or core and crustal material. The stony meteorites are mostly chondrites (83%) but they can also be achondrites. The latter are magmatic

rocks, they lack chondrules as the name indicates and are believed to have come from the crust of planets and other smaller differentiated bodies.

Chondrites formed in the early stages of the solar system and they have a chemical composition that is similar to the chemical composition of the sun in terms of elements belonging to the so-called refractory group elements, that is, elements that have a condensation temperature higher that 1500 K. They formed in the proto-planetary stage, 4.57 Ga ago, and were incorporated and preserved inside geologically inactive bodies, like comets or asteroids, thereby preserving in them some of the oldest material of the solar system. They are composed of chondrules and calcium-aluminum-rich inclusions (CAIS) imbebed in a matrix, which is formed of micro-grains of iron and magnesium silicates, metal and sulfides that resemble a cement that contains the chondrules and CAIS.

Chondrules, which are small round grains usually smaller than 1 cm in diameter, are thought to have formed as molten or partly molten droplets floating in the proto-planetary disk before being accreted into asteroids. They are composed of iron and magnesium silicates and metal and sulfides, showing an igneous structure that suggests that they have melted, perhaps several times, in the proto-planetary disc. Lead isotope dating indicates that they formed around 4564 Ma to 4566 Ma ago [3].

CAIS are thought to be even older than condrules (lead isotope dating yielded ages of 4567.2 to 4568.7 million years [4]), as their chemical composition lead them to solidify at higher temperatures, when the proto-planetary disc started to cool down. They are a mixture of calcium and aluminum oxides and silicates.

Both chondrules and CAIS show evidence of having been exposed to widespread, highly energetic, transient heating events. This evidence has provided a starting point to several models developed with the goal of trying to understand the development of the proto-planetary disk.

Besides the evidence of violent temperature variations, the analysis of these structures in meteorites fallen on earth, shows that they incorporated SLR's at the time of their formation. They cannot be measured directly in the

meteorite samples due to their short half-lives, but they are known to have been present from the measurements of their daughter isotopes and of their abundances relative to the concentration of isotopes in them. The first radionuclide discovered this way was ^{129}I ($t_{1/2}$=15.7 Ma), by the measured abundance of its daughter nuclei ^{129}Xe in meteorites in 1961 by Jeffery and Reynolds [5].

6.2.2 SLRs

There are nine SLRs presently known to have existed, by analysis of meteorite samples, in the primordial solar system [6]. They are shown in table 1. Of these, ^{7}Be, ^{10}Be, ^{36}Cl, ^{41}Ca ,^{53}Mn and ^{60}Fe are specially important since their deduced abundances are too high for a galactic background origin. The galactic background incorporates radionuclides that are created and injected into the interstellar medium by various nucleosynthetic processes in stellar objects such as core-collapse supernovae, type Ia supernovae, novae, and outflows from Wolf-Rayet stars and asymptotic giant branch (AGB) stars.

There can only be injection of fresh material into a forming solar system after its gas cools down and condenses into molecular clouds. Since this process takes about 10^8 years, it means that the SLRs once present in meteorites cannot have been the ones already present (coming from the galactic background) in the material that formed the solar nebula, as their short half-lives imply that these had already decayed when the CAIS and chondrules formed. This means that they had to be formed in situ around the time of CAIS and chondrule formation or injected at that time by nearby stellar objects.

Among the various hypothesis [6,7,8] advanced to explain the overabundance of the SLRs, there are three main models that are the most debated presently, and are not mutually exclusive; the SLRs came from mass-loosing stars (supernova or pre supernova) present in the vicinity of the nascent solar system, they were generated by the trapping of galactic cosmic rays (GCR) within the presolar core (this particular model is relevant only for Be and has

been put into question recently) or they were generated in situ by irradiation of the nebular material by protosolar cosmic rays.

The first model probably accounts for most of the production of ^{26}Al and ^{60}Fe, while the third model accounts for the production of ^{6}Be and ^{10}Be, probably a small part of ^{26}Al and most of the production of ^{36}Cl and ^{41}Ca.

The first model is currently the only explanation for the presence of ^{60}Fe in the nascent solar system, if not of ^{26}Al, whose abundance can be explained by other mechanisms, although with some difficulty. If the abundance of ^{60}Fe and ^{26}Al points to a stellar origin, then it is important to know which kind (or kinds and how many) of stellar object or objects produced them and their relation to the young solar system and at which point in the solar system formation did this contribution happened.

Parent isotope	Half-life (*My*)	Daughter isotope	Solar system initial abundance
^{41}Ca	0.1	^{41}K	$^{41}Ca/^{40}Ca \approx 1.5 \times 10^{-8}$
^{36}Cl	0.3	^{36}Ar(98.1%) ^{36}S(1.9%)	$^{36}Cl/^{35}Cl \approx 1.6 \times 10^{-4}$
^{26}Al	0.72	^{26}Mg	$^{26}Al/^{27}Al \approx 5.7 \times 10^{-5}$
^{60}Fe	1.5	^{60}Ni	$^{60}Fe/^{56}Fe \approx 3 - 10 \times 10^{-7}$
^{10}Be	1.5	^{10}B	$^{10}Be/^{9}Be \approx 10^{-3}$
^{53}Mn	3.7	^{53}Cr	$^{53}Mn/^{55}Mn \approx 10^{-5}$
^{107}Pd	6.5	^{107}Ag	$^{107}Pd/^{108}Pd \approx 5 - 40 \times 10^{-5}$
^{182}Hf	8.9	^{182}W	$^{182}Hf/^{180}Hf \approx 10^{-4}$
^{129}I	15.7	^{129}Xe	$^{129}I/^{129}Xe \approx 10^{-4}$

Table 6.1: SLR's with their half-lives, daughter isotopes and respective abundance in the initial solar system [8].

In terms of the nature of the stellar object (or objects) producing these SLR, the most likely candidates are massive stars (>8 solar masses), because these lose mass as powerful winds, while still burning stellar fuel, or by supernova ejecta when they explode and die. Besides this hypothesis, there has been the

suggestion that Asymptotic Giant Branch (AGB) stars could be responsible for the injection of the SLRs, but this has been questioned recently as the presence of these stars in a star-forming region is improbable.

The hypothesis of a single supernova injection was advanced as far back as 1977 [9]. This model initially proposed the injection of the two SLRs in the prestellar core. However, this cannot account for the abundances of ^{26}Al and ^{60}Fe. To address this problem, there was a more recent suggestion [10] that the single supernova injection could have happened in the already formed disk, by a supernova close enough (~0.3 pc) to the proto-planetary disk so as to allow for enough material to reach the disk. Such proximity, however, implies that both the proto-planetary disk and the massive star formed in the same stellar cluster. This presents some problems, since the timescales of massive star evolving to supernova and proto-planetary disks photo-evaporation (in the vicinity of a massive star) don't seem to match. Besides, even this proximity has difficulties explaining the high abundance of the two SLRs. Because of this, an alternate scenario has recently been proposed that not one but several supernovae were present and contributed to the origin of the solar system, injecting ^{60}Fe into the forming nebular cloud [11] .

6.2.3 ^{36}Cl

The analysis of Cl-S systematics of sodalite in carbonaceous chondrites yielded a ratio of $^{36}Cl/^{35}Cl$ around 10^{-6}. Since sodalite is in principle a late-stage product of aqueous alteration, this ratio's initial value should have been higher, assuming that the ^{36}Cl supernova injection happened in the prestellar core stage, as it is supposed to have happened with the other SLRs. Following this principle, the expected $^{36}Cl/^{35}Cl$ ratio at the time of the SLRs injection has been estimated to be around 10^{-4}. This value is already too high for the estimated supernova injection of $^{36}Cl/^{35}Cl \sim 10^{-6}$. However, recent analysis of wadalite in the Allende carbonaceous chondrite, seem to make the SN injection of ^{36}Cl scenario even more implausible, yielding a ratio of $^{36}Cl/^{35}Cl \cong (1.72 \pm 0.25) \times 10^{-5}$, making the initial ratio even higher than 10^{-4} [12]. This seems to definitely

invalidate the possibility of ^{36}Cl injection by a supernova. There must be an alternative origin for this SLR.

The most credible hypothesis is that this SLR was formed by direct bombardment of target nuclei by energetic ions, namely protons and helium. This bombardment was advanced initially in the context of the X-wind model.

The X-wind model was proposed by Shu [13] and collaborators in the 1990's as a model of gas dynamics in protostellar systems, with the goal of explaining some observed phenomena in T Tauri stars. It gained some following for its ability to account for many observations, such as optical observations of time variable accretion/wind phenomena in T Tauri stars and also the stars slow rotation rate, protostellar X-ray activity and several observed features in known T Tauri stars such as jets and molecular outflows. It is one of the models that has received the most attention in terms of providing a possible mechanism for the production of chondrules and CAIs, namely the melting and re-melting evidenced in these structures.

In the X-wind model, the premise is that the proto-planetary disk has a inner hole where the proto-star is located. Assuming that the star is a dipole, there will be magnetic field lines flowing from one pole to the other. These magnetic field lines would, were it not for the presence of the disk, cross the protostar's equatorial field plane at a relatively long distance from the star. But, due to the presence of the proto-planetary disk, the magnetic field lines are compressed through the space between the protostar and the disk. Assuming that the disk is non-ideal, there will be some magnetic diffusivity and accretion at its inner rim and in that area the magnetic field lines will penetrate creating a ring (the inner part of the disk) where the magnetic lines are compressed. This ring is called the X-region. The X-region or ring has an inner radius, R_X, which is also the inner radius of the proto-planetary disk. It is the distance between the center of the star and the point (sometimes called X-point) where the pressure of the magnetic filed lines prevent the gas of the proto-planetary disk to further approach the proto-sun.

Since the material in the X-region is ionized, it will be forced to follow the rotating magnetic field lines generated by the protostar, and therefore rotate with it. This means that the X-region will be rotating at the same angular

velocity of the protostar. As this happens, some of the material in the X-region closer to the star, which is moving at lower speeds than the rest of the ring, may start to diffuse towards the protostar, and actually cross the X-point. This material is then heated and expanded and is channeled to the poles of the protostar in an accretion funnel by magnetic field lines. This accretion funnel flow of gas would easily spin outwards due to its angular momentum but, being ionized, it sticks to the rotating field lines and exerts a forward torque to the protostar and disk. Simultaneously, in the outer part of the X-region ring, the gas is rotating at much higher velocities than in the most inner part. At the same time, in this region the magnetic field lines are weaker and are almost parallel to the disk. This combination results in some of the gas being removed from the disk by a magneto-centrifugal force. This expanding flow of gas is called the X-wind and it carries angular momentum with it from the disk therefore compensating the added momentum to the disk due to the accretion funnel gas. The X-wind's velocity and density increase towards the polar axis.

There is then a dynamic equilibrium, where the gas in the parts of the X-region further away from the star is being driven outwards my a magneto-centrifugal outflow, and the material closest to the X-point is being pulled into the star poles, crossing the x-point. At this point, beyond R_X, the material will be heated, and will be subjected to X-rays generated by magnetic reconnection events, similar to solar flares, inside the funnel flow towards the star poles. This will heat them further. The zone interior to the funnel flow, where magnetic reconnection events can occur is called reconnection ring and is located roughly between $0{,}75R_x$ and R_x. Most of the material subject to heating in the reconnection ring will follow the path through the funnel flow. However, some of this material (around 1%) can escape the funnel flow and either fall directly towards the star or cross the X-point again and be picked up by the magnetocentrifugal outflow and eventually land in the outer regions of the planetesimal disk. This material would be the CAIS and chondrules as they cooled down in the path towards the outer regions of the planetisimal disk.

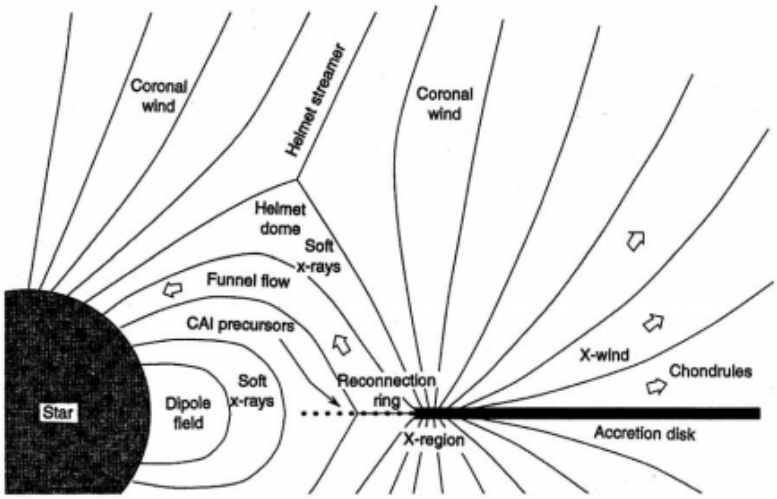

Figure 6.2: Schematics of the X-wind model.

It is also in the reconnection ring that SLRs will be formed. This is due to the solar flare like events that happen in this area. These magnetic reconnection events could accelerate hydrogen and hellium ions to energies in excess of 1 MeV per nucleon. If these reconnection events are akin to solar flares, they could produce even higher energies. Nowadays, the flux of energetic particles from the sun with energies above 10 MeV per nucleon at 1 AU is about 100 cm^{-2}/s. T Tauri stars evidence even greater fluxes, about 5 times in some cases. This means that the material in the reconnection area would be bombarded by highly energetic particles, mostly hydrogen and helium. Some of this material would in the future become the CAIS and chondrules by the process explained above.

The X-wind model is not consensual and has received some criticism [8]. However, it would be more consensual if some mechanism of producing ^{36}Cl by irradiation is found. It is therefore important to know nuclear cross sections of nuclear reactions producing ^{36}Cl in order to test and develop models that can justify the existence of ^{36}Cl at the beginnings of the solar system.

6.3 Technical developments for chlorine measurements

Having introduced the motivation to this work, all the rest of the chapter will be dedicated to the work that went into the Micro-AMS chlorine measurements of neutron irradiated AgCl samples.

Since the original AUSTRALIS system was not prepared for very low isotopic ratio measurements ($<10^{-5}$), a great deal of work went into the adaptation of this system to the requirements of this kind of measurements. All the work that was developed could be described as an attempt to maximize the precision of the chlorine measurements to the point that they could actually be useful for cross section nuclear reaction measurements, while assuring that the sulfur background in the system is minimized. This is a usual preoccupation in conventional Chlorine AMS measurements [14], since the ^{36}S isotope is an isobaric interference of ^{36}Cl. As was explained in chapter 3, the separation factor $S_{A,B}$ for isobar peaks in the ionization chamber detector spectra is inversely proportional to the atomic number *Z*. For 3 MV tandems this meant up until recently, that an effective isobar separation was only possible up until around mass 30. However, recent work developed in ETHZ Zurich and VERA in Vienna have successfully achieved separation for ^{36}Cl and ^{36}S using conventional ionization chambers [15]. Nonetheless, this requires the use of solid stripper foils (which permits higher stripping efficiencies, and therefore higher beam energies) and, in some cases [16], taking the accelerator terminal voltage up to 3.6 MV and the use of special position sensitive detectors inside the ionization chamber.

There are two main reasons that explain why this was not attempted in the CTN-ITN Micro-AMS system. First, the LATR tandem is an old machine and our group's attempts to push the terminal voltage of the accelerator to its maximum voltage proved that, in its current state, it cannot go much higher than 2.5 MV. Also, since the tandem is used by another research group, and also by our own research group for NRA and PIGE, it was impractical to experiment with foil stripping, since this kind of stripping would not present any advantage to the proton beams used in these other experiments, while being eventually disadvantageous, as foil stripping tends to increase beam energy

straggling and the stripper foils are known to break routinely, which would mean opening the accelerator much too often, with all the beam time loss that entails. Second, since the Micro-AMS uses a micro-beam, which is on average three orders of magnitude less intense than the conventional AMS beam, this means that its detection limits fall by that amount or more. Our experience in the work that went into this thesis showed that our detection limit was around $^{36}Cl/^{35}Cl \approx 10^{-10}$. The literature shows [17] that it is possible to keep the ^{36}S content in the beam reaching the detector well below this amount, by using several techniques that will be shown in the next subchapters, therefore allowing us to be confident in dispensing with isobar separation in the ionization chamber. Our measurements confirmed this.

The bulk of the work involved in the adaptation of the system to very low isotopic ratio measurements can be divided into the development of the sample holder system, with the goal of maximizing sample current output while minimizing sulfur contamination (that can come from the materials used in the sample holder and not just the sample itself), and the work that went into the beam transport system and its adaptation to measuring the several chlorine beams (^{35}Cl, ^{36}Cl and ^{37}Cl beams).

6.3.1 Sample Holder

The contamination of ^{36}S present in the sample holder (besides the one present in the sample itself which will be dealt with in the next subchapter) is a well-known problem in conventional AMS [17]. The micro-beam used in Micro-AMS is an advantage in this case, because it is easier to assure that the whole bombarded area is located strictly within the target limits, as opposed to conventional AMS where the large diameter beam, maximized for intensity, will easily impact the sample holder as well during operation. However, since there is no possibility to separate ^{36}S from he ^{36}Cl in our system, it is important to assure that no sulfur contamination may be present anywhere close to the sample. This means that the chamber has to be as clean as possible, and the sample holder must be designed so as to minimize any contamination as well.

The final version of the sample holder, the one that after some developments proved the most successful in terms of lower sulfur background is as follows; the sample holder was covered with a sheet of copper, totally covering its stainless steel structure. This means that an area of 40 cm^2 is available for sample mounting. However, since cross-contamination of samples can happen easily, the maximum number of samples per run was set at 4. This way it was possible to keep the samples at a reasonable distance (> 3 cm) from each other, and still be able to have a blank sample, a standard, and two unknown samples in each run. In each of the positions where the samples were to be installed, a round disk of two centimeters in diameter of compressed AgBr was installed. The AgCl samples were then mounted at the center of these disks. This AgBr disk was shown in the literature [17] to be the most efficient material in minimizing sulfur contamination to the chlorine beam.

At this stage, it is very important to assure that all the surfaces of the samples are at the same distance from the copper base of the sample holder, so that the primary beam hits the samples in exactly the same position, so as not to induce differences in the secondary beams, in terms of angle of exit or intensity.

The samples are compressed AgCl as already mentioned and their surface areas were always maximized within the constraints of the sample itself; for instance, the mass of the irradiated samples was limited by the produced activity (most of it coming from the silver content of the samples), for radiological security purposes, and therefore, some of them had to be smaller than the average 0.8 cm diameter, used for blanks and standards. However, every sample was always much wider in terms of surface than the beam diameter (>20 x beam diameter for all samples).

With this setup, the background of blank samples produced by the chemical method described before yielded a background well bellow $^{36}S/^{35}Cl \approx 10^{-10}$.

Besides the background induced by the sample and sample holder, another important source of background in the mass 36 channel was the one produced by memory effect. This is a well-known problem in chlorine AMS [17]. This effect is due to the fact that some of the ^{36}Cl from the sample being analyzed will be deposited in the electrodes around the sample. This ^{36}Cl may

eventually make its way into the secondary beam, even after the original sample was exchanged by a new one, therefore creating a counting rate for ^{36}Cl higher that the one coming just from the new sample.

The experience in the case of the Micro-AMS system proved however, that in this case, the memory effect was not as intense as in conventional AMS, due to the smaller intensity of the primary beam. Nonetheless, a special order of sample measurements was followed, following the common practice in AMS measurements, and the memory effect was always monitored after each sample. The order was: blank, unknown sample, blank, standard, blank. In each blank run it is possible to monitor the background in mass 36. If there is some background, the beam is kept on the blank until the background decreases to below 1 count per second.

It is also important to refer that, in keeping with all the measurements of different elements performed, the target chamber was always kept as clean as possible. The cleanliness of the target chamber is of course of paramount importance in Micro-AMS. In the particular case of chlorine, and due to this element good sputtering yield, it was clearly visible that, after a few days of beam time, the chlorine would deposit all around the sample holder. This deposit even damaged the visibility of the microscope after a few days, as the target material would deposit in the prism and the glass plate at the top of the chamber.

6.3.2 Beam transport system

One of the main problems in the chorine measurement was related to the quasi-simultaneous measurement of the ^{35}Cl, ^{36}Cl and ^{37}Cl beams. This is fundamental for the good precision of the measurement, since fluctuations in stability of the ion source, accelerator and/or any of the elements of the beam transport system, will affect each beam differently if these are not measured practically at the same time. This is the reason why the bouncing system was developed, as was seen in chapter 3 and 5. However, in the case of the chlorine

measurement this bouncing operation is not as easy to perform as the examples shown in chapter 5.

The main technical problem is the difference of beam intensity between on the one hand, both stable isotopes, ^{35}Cl and ^{37}Cl, and the radioactive one, ^{36}Cl, on the other. This difference is higher than six orders of magnitude; the $^{36}Cl^{4+}$ beam usually bellow 100 particles per second in most samples and the other two beams above 10^7 particles per second. This difference meant that, while the ^{36}Cl beam could be measured in a PIPS detector (with the additional benefit of the energy information provided by this detector), the other two beams were too intense for the particle detector, and therefore had to be measured in a faraday cup. And although 10^8 particles per second may seem a very high intensity beam, in reality it is still well below the nano-ampere, too low a current for the current integrators present at the lab, and therefore only measurable in a pico-ampmeter (the unavailability of a pico ampere current integrator in the lab was an additional problem as the Keithley pico-ampmeter is slow for the desirable frequency required by these measurements).

However, before addressing the problems related to the different beam intensities, the faraday cups themselves had to be designed and installed off-axis (axis here refers to the main axis of the beam, that is, the center of the tubes of the transport system). This off-axis position is necessary because the pneumatic system that operates the on-axis faraday cups is not fast enough to put the normal faraday cups in and out of the beam axis at the frequency required of the bouncing system for a high precision measurements (100 ms or less per beam in each cycle).

Steps were taken in the design of these three off-axis faraday cups (two after the low energy magnet and one after the high energy magnet) to maximize electron suppression, especially in the case of the HE off-axis FC, as the currents measured in it were used to calculate the final isotopic ratios, which are the main output of each measurement.

In the case of the LE FCs, they were designed in the form of a triangular box with one of the sides of the box opened. With this geometry it is easier to trap the electrons that escape the copper that forms the FC when it is hit by the 10 keV beams. So both triangular boxes have the open side facing the beam, one

on each side of the beam axis. In front of the FCc there is a grounded plate, with three slits; a central one with a width of 3 mm, in the beam axis, and two large ones, one on each side in front of each of the FCs. The FCs were built as a single piece and can be mounted in the same axis in the mini-chamber after the LE magnet, by replacing the ETP ion counter and FC that are usually in that position. This is not a problem since in chlorine measurements the ETP is of no use. The two FCs can then be removed if other measurements requiring an LE ETP are to be performed. The positions of the LE off-axis FCs are such that both $^{35}Cl^-$ and $^{37}Cl^-$ can be measured simultaneously while the $^{36}Cl^-$ beam is injected into the accelerator, without recurring to the bouncing system. This was possible because the trajectories of the 3 beams are close enough to each other after the LE magnet.

The HE off-axis FC was designed as shown in figure 6.3. The plate in front of the FC is polarized at 60 V in order to maximize electron suppression.

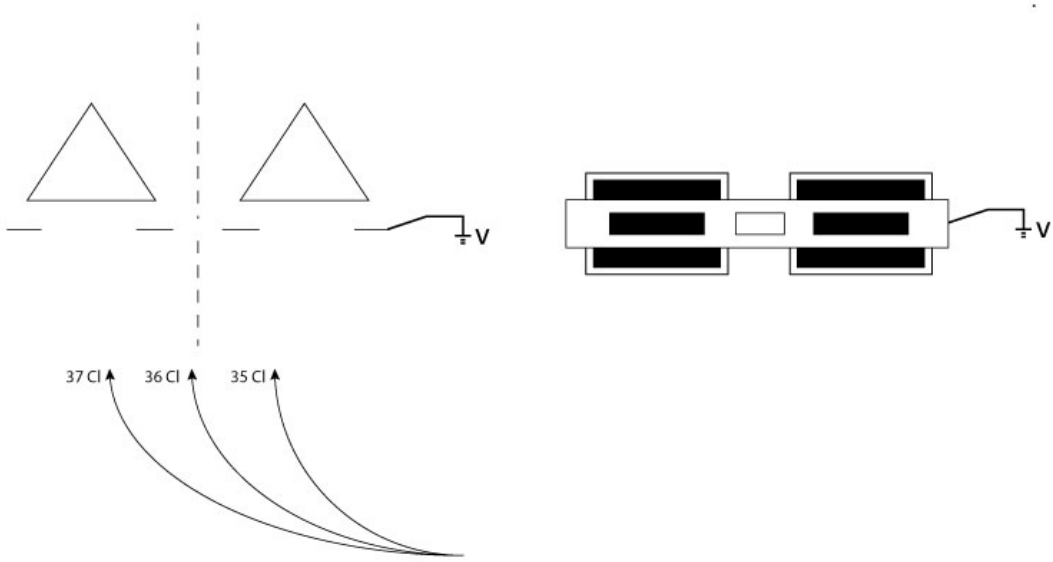

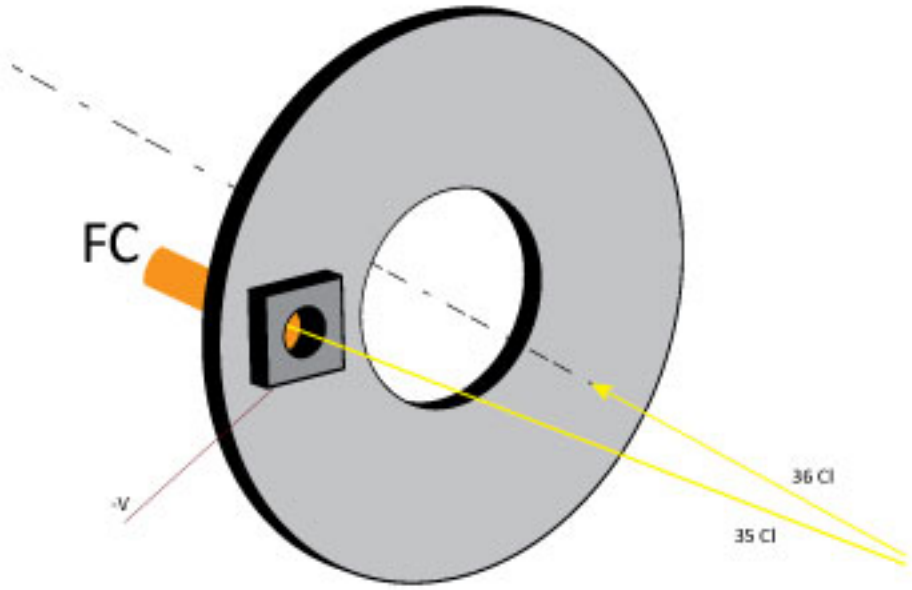

Figure 6.3: Scheme showing the design of the off-axis LE Faraday cups (previous page) and the HE off-axis Faraday cup (current page). In the top image, the three curved lines correspond to the three chlorine isotope beam as they exit the LE magnet.

6.4 Sample preparation

As previously mentioned, it is important to prevent any presence of sulfur in the AgCl samples. This requires a chemical preparation of the AgCl samples.

The chemical preparation of AgCl samples for AMS chlorine measurements is a very well known process [18]. It was developed with the goal of extracting ^{36}Cl from the material of interest, for instance ground water, mix it with a certain amount of (the so-called carrier) ^{35}Cl, to produce a final sample material in the form of AgCl. This particular chemical formulation, which is a white powder sensitive to light, has been used since the beginning of

chlorine AMS measurements because it can easily be compressed into a pellet, and in this compacted form and under cesium bombardment, it produces a high intensity, stable secondary beam of chlorine.

In the particular case of this work, since the goal was to irradiate chlorine with a neutron beam to produce ^{36}Cl, and since AgCl is a suitable chemical form for this irradiation (for reasons explained earlier), the chemical procedure is much simplified; it is only necessary to produce AgCl with as little sulfur as possible, and therefore the steps necessary for the extraction of ^{36}Cl from the original material are ignored. Besides the production of extra pure AgCl blank material for irradiation, it was also necessary to produce some AgCl with a known isotopic ratio of $^{36}Cl/^{35}Cl$, for reference material, that is, to produce some standard samples.

So, special steps were taken during the process of producing the AgCl pellets, to make sure that the final sulfur content in the sample is as low as possible, which means special cleaning procedures of all material involved in the process and chemical removal of any sulfur that may be present in the sample. The problem with sulfur contamination in the AgCl samples is the existence of ^{36}S, which is a stable isotope of sulfur, and an isobaric interference of ^{36}Cl. Even though its natural abundance is only 0,02%, this means that it will be counted in the detector even if only few ppb of sulfur are present in the sample. And since, for reasons already explained, the separation of ^{36}Cl and ^{36}S in the detector will not be performed in this work, it is very important to keep the sulfur content in the produced samples at a minimum. It is nonetheless important to refer that the lower detection limits of Micro-AMS when compared to AMS will mean that the sulfur content of the samples in the case of the present work will not be such a big problem as in a conventional AMS measurement. Other labs have shown that, using the steps in sample preparation shown bellow, the sulfur background was reduced to $^{36}S/^{35}Cl=10^{-12}$ [17], which is well bellow the micro-AMS system detection limits for chlorine.

6.4.1 Chemical procedure

In order to produce AgCl, a solution of NaCl was mixed with a solution of $AgN0_3$, resulting in the immediate precipitation of AgCl.

All the material used in the procedures described below were washed with bi-distilled water, followed by an ultrasonic bath with isopropane alcohol for around 10 minutes, followed by a ultrasonic bath with 1.4 M HNO_3 for another 10 minutes.

- The solution of NaCl was produced by diluting NaCl from Alfa Aesar (Sodium chloride, Puratronic®, with a purity of 99.999 %, Art# 10862) in bi-distilled water, to a concentration of 12.5 - 125 g/l depending on the amount of AgCl desired per sample.

- The solution of $AgNO_3$ was produced by diluting $AgNO_3$ from Sigma-Aldrich in 0,5 M nitric acid to a concentration of 70 - 350 g/l.

- In order to chemically remove possible sulfur contaminations, a solution of $Ba(NO_3)_2$ was added to each solution. Each solution was left untouched for 24 hours in order that all sulfur in the solution could precipitate in the form of $BaSO_4$.

-After the 24 hour period, each of the solutions was filtered using a quartz filter with vacuum suction.

-Both solutions were then mixed in several falcon tubes, resulting in the immediate formation of a white powder which precipitated after a few seconds.

- The tubes were loaded into a centrifuge and centrifuged for a few minutes.

- After the centrifugation, the AgCl powder and the water were visibly separated, with the powder forming a pellet at the bottom of each tube. The water was removed, and the pellet again dispersed into bi-distilled water (treated previously for sulfur removal using the $Ba(NO_3)_2$ method).

- After this last wash the powder was left to dry in an oven overnight at 40 ^oC.

6.4.2 Production of standards

For the production of standards, the exact procedure described above was used, with only one additional step; a drop of the NIST standard solution SRM 4943, measured with a high precision pipette, was added to the initial NaCl solution. The calculations for the volume of this drop and the content of NaCl in the solution were made so as to produce the pretended final isotopic ratio.

6.5 Neutron irradiation of blank AgCl samples

In order to measure the thermal neutron capture cross section for the $^{35}Cl(n,\gamma)^{36}Cl$ nuclear reaction, four AgCl samples were irradiated at the RPI (Reactor Português de Investigação) at CTN-ITN. The RPI is a 1 MW pool-type nuclear reactor, active since 1961 and dedicated exclusively to scientific research [19].

The irradiation times and neutron fluxes were calculated to produce the following isotopic ratios;

sample 1: $^{36}Cl/^{35}Cl = 4 \times 10^{-6}$

sample 2: $^{36}Cl/^{35}Cl = 4 \times 10^{-7}$

sample 3: $^{36}Cl/^{35}Cl = 4 \times 10^{-8}$

This procedure had other purposes besides the goal of measuring the $^{35}Cl(n,\gamma)^{36}Cl$ cross section, namely to test the quality of the AMS system, by comparing the irradiated samples with the previously produced standards (consisting of the dilution of the NIST SRM 4943 chlorine standard), and if this proved successful, to eventually use irradiated AgCl samples as AMS standards themselves.

The ^{36}Cl radionuclide has a half-life of 3,05 $x10^5$ years, which yields a low radioactive activity (for samples with low isotopic ratios such as the ones in these experiments;$^{36}Cl/^{35}Cl < 10^{-6}$), that is, relatively small number of particles emitted as ^{36}Cl nuclides decay into their final stable form. Besides the low activity, its main emission products are electrons (beta decay), which are difficult to measure. This makes it difficult to measure the amount of ^{36}Cl generated by the irradiation by direct measurement of decay products, and therefore a good test to the micro-AMS capabilities.

However, it is very important to monitor the reactor's neutron flux during irradiation since the flux used in the calculations of the irradiation time and sample mass, is an approximate value. The fact that AgCl is the chemical form used in AMS samples for chlorine AMS measurements (due to its high sputtering yield) could be helpful in this regard, since the silver content in the samples could be used to monitor the reactor's neutron flux in the sample during the irradiation, by measuring the gamma rays emitted by the radioisotope ^{110m}Ag ($t_{1/2}$ =249.79 d), produced by the $^{109}Ag(n,\gamma)^{110m}Ag$ nuclear reaction. As an additional control, a gold monitor was also used with each sample, since this is the standard procedure for neutron flux monitoring, as the $^{197}Au(n,\gamma)^{198}Au$ (^{198}Au has a $t_{1/2}$=2.695 d) cross-section is very well known.

The gamma radiation measurements were done two days after the irradiation, using a HPGe detector in the LATR lab at CTN-IST.

Before advancing further into the results obtained with the irradiations, a brief introduction to the physical mechanisms of neutron irradiation of samples will be made in the following pages.

6.5.1 Brief introduction to neutron activation of samples using nuclear reactors

By placing a sample in the path of a neutron flux produced by a nuclear reactor such as the RPI, a nuclear reaction will occur, by which a nuclide *X* present in the sample will be transformed into the radioactive nuclide, or

radionuclide, Y, which, being unstable, will decay into a stable isotope Z. This nuclear reaction can be represented as:

$$X(n,x)Y \rightarrow Z$$

where n stands for neutron, x can be one or more of several kinds of radiation, which are emitted by Y when it decays into Z, the final stable product of the cycle. The rate of decay is given by the decay constant, λ, which relates to the half life, T, of the radio-nuclide (which is the time it takes for half of the population of Y nuclides in the sample to decay to Z) as follows:

$$\lambda = \frac{\ln(2)}{T}$$

The rate of formation of radionuclide Y is given by the following differential equation:

$$\frac{dN}{dt} = N_{0X}\sigma\phi - \lambda N$$

where:

N_{0X} = initial number of X nuclides in the sample

ϕ = average neutron flux irradiating the sample, expressed in neutrons per square centimeter per second (*neutrons.cm*$^{-2}$*.s*$^{-1}$)

σ = neutron capture cross-section (usually presented in barns, b)

N = number of nuclides Y

If N_{0X} is constant in time and $N=0$ at $t=0$, then the solution to (X) is:

$$N = \frac{1}{\lambda} N_{0X} \phi \sigma . (1 - e^{-\lambda t}) \qquad (2)$$

The activity, *A*, of the sample is the rate of decay of *Y* products. It is given by:

$$A = \lambda N$$

It is usually presented in *Becquerel* (*Bq*) or *Curie* (*Ci*); 1 Ci = 3,7x10^{10} Bq.

This means that at the end of the irradiation time, t_{irr}, the activity of the sample will be given by:

$$A = N_{0X} \sigma \phi . (1 - e^{-\lambda t_{irr}}) \qquad (3)$$

where N_{0X} can be determined by using the following:

$$N_{0X} = m \frac{N_A}{M} \theta_X$$

with

M = molar mass of element *X*

N_A = Avogadro constant

m = mass of element *X* in the sample

θ_X = natural abundance of isotope *X* in the *X* element

It may be useful in some cases to use the specific activity of the sample after irradiation, A_{esp}, which is independent of the mass of the sample. Since:

$\lambda T = \ln(2) \approx 0.693$

$N_A = 6.02\times10^{-23}\ mol^{-1}$

$1\ barn = 10^{-24}\ cm^2$

The specific activity can be written thus:

$$A_{esp} = 0{,}602\frac{1}{M}\theta_X\sigma\phi.(1 - e^{\frac{-0{,}693t_{irr}}{T}}) \qquad (4)$$

whose units are *Bq/g* or *Ci/g*.

6.5.1.1 Neutron flux and neutron capture cross section

As can be seen by (3), it is relatively easy to predict the activity of a given sample irradiated by a neutron flux, after a certain irradiation time, if the neutron flux and nuclear reaction cross section are known.

The neutron flux of a nuclear reactor like the RPI is composed of neutrons with a wide range of energies. These neutrons are divided into three main groups according to their energies:

thermal neutrons: 5×10^{-5} eV < E_N < 0,025 eV

epithermal neutrons: 1 eV < E_N < 10 keV

fast neutrons: $E_N \approx 1$ MeV

So the average neutron flux ϕ that will activate the sample will be composed of three fluxes; thermal neutrons flux ϕ_{th}, epithermal neutrons flux ϕ_{epi} and fast neutron flux ϕ_f. In table 6.2, the calculated percentages of thermal, epithermal and fast neutron fluxes that constitute the overall neutron flux in several sample positions in the RPI reactor core is shown.

Position	ϕ_{th}		ϕ_{epi} 0.5 eV-10 keV		ϕ_f	
	C (10^{12} cm^{-2} s^{-1}) (%)	C/M	C (10^{11} cm^{-2} s^{-1}) (%)	C/M	C (10^{11} cm^{-2} s^{-1}) (%)	C/M
55	10.2±0.3	1.04±0.05	9.59±0.9	0.86±0.05	4.94±0.9	0.94±0.05
57	0.313±2	0.90±0.08	0.232±6	0.87±0.08	0.214±4	0.90±0.07

Table 6.2: Calculated neutron fluxes (C) for thermal, epithermal and fast neutrons for all the RPI sample positions. C/M is the calculated value divided by the measured value [19].

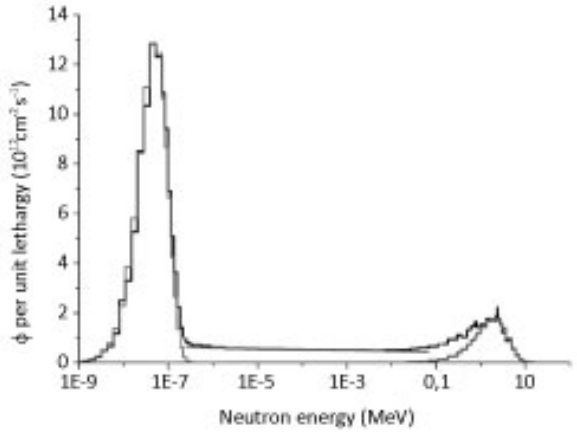

Figure 6.4: Plot of neutron flux vs. neutron energy in position 54 of the RPI nuclear reactor [19].

As can be seen in table 6.2, in the positions used to irradiate the three AgCl samples (positions 55 and 57) the greatest percentage of neutrons in the overall neutron flux is in the thermal energy region (notice that the units of *C* for thermal neutron flux are 10^{12} cm^{-2} s^{-1}, while the other two fluxes are 10^{11} cm^{-2} s^{-1}). It is important to know this because the nuclear reaction cross section is highly dependent on neutron energy. Figure 6.4 shows a plot for one of the

reactor core positions (54 in this case) where it can be seen how the thermal flux has a near Gaussian peak shape centered around E_N = 0,0253 eV.

Figure 6.5 shows a plot of the neutron capture cross-section dependence on neutron energy, $\sigma(E_N)$, for the $^{35}Cl(n,\gamma)^{36}Cl$ and $^{197}Au(n,\gamma)^{198}Au$ neutron capture reactions, that are central to this thesis study.

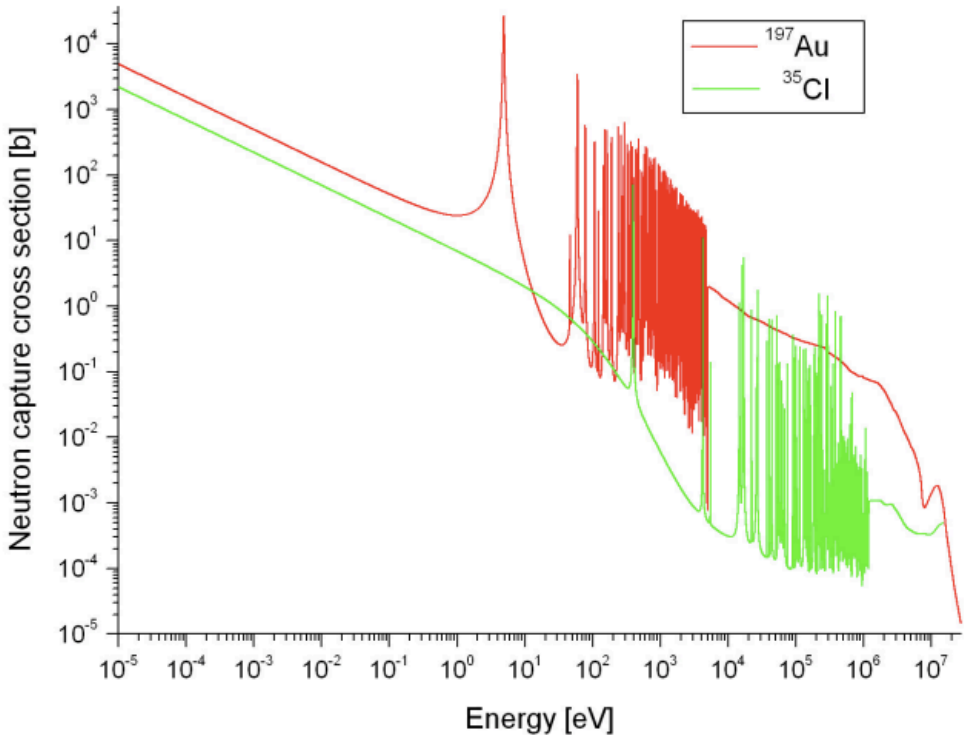

Figure 6.5: Neutron capture cross section dependence on neutron energy ,σ (E_N), for the $^{197}Au(n,\gamma)^{198}Au$ (left) and $^{35}Cl(n,\gamma)^{36}Cl$ (right) nuclear reactions. The data was taken from the ENDF/B-VII.1 library

The value used for the thermal neutron cross section in the calculation of the activity using (3) is usually the cross section at neutron velocity of v_0 = 2200 m/s (corresponding to a neutron energy of E_0=0,0253 eV at 293.6 K), usually represented in the literature by σ_0, and also called thermal neutron capture cross section. This value is used because the convolution between $\sigma(E_N)$ and $\phi(E_N)$ will yield a very sharp peak for E_0, which intensity is much higher than for all the rest of the energies combined. Therefore it is a valid

simplification to use σ_0 as the value for the cross section in (3). This simplifies an otherwise complicated calculation, involving a more accurate determination of $\sigma(E_N)$ and $\phi(E_N)$, across the whole range of E_N.

Nevertheless, there are methods which were developed so as to yield a better approximation to the whole energy range of the neutron flux and excitation function for $\sigma(E_N)$, and provide a more accurate value for the final activity of the irradiated sample.

6.5.1.2 Wescott formalism

In the previous pages, a simplified method for the calculation of the activity of a sample irradiated in a nuclear reactor was introduced. This definition assumes an average overall neutron flux and σ_0. It also assumes that the neutron flux is constant over all the volume of the sample, and is not attenuated by it.

A more accurate description of the total activity would be the following:

$$A_{tot} \propto \int_0^\infty \sigma(E)\varphi(E)P(E)dE$$

where $P(E)$ reflects the local attenuation of the neutron flux by the sample itself or by a nearby sample.

This integral is difficult to solve, because, as was mentioned, demands the accurate determination of $\sigma(E_N)$ and $\phi(E_N)$, across the whole range of E_N.

The Wescott convention [20] was developed to simplify the calculations of the overall activity, by recurring to experimentally determined neutron fluxes, reaction cross sections and global neutron flux attenuation factors.

The basic concept of the Wescott convention is the effective cross section:

$$\hat{\sigma} = \sigma_0(g_w + rs)$$

where g_w characterizes the cross section $\sigma(E_N)$ in the low energy region, being equal to one whenever the cross section has a $1/v$ dependence in this region, which happens for most nuclides.

The spectra index r reflects the proportion of epithermal neutrons in the neutron flux, which is zero whenever the neutron flux is composed only of thermal neutrons, and $r \approx \Phi_{epi}/\Phi_0$ (Φ_{epi} *is* ϕ_{epi} *at* $E = 1eV$, Φ_0 *is* ϕ_{th} *at* E_0) whenever the epithermal flux is low.

$$s = \frac{2}{\sqrt{\pi}} \frac{I - 0{,}45\sigma_0}{\sigma_0}$$

with

$$I = \int_0^{\infty} \sigma(E) \frac{dE}{E}$$

I is the resonance integral of Y for $X(n,x)Y$.

If $\frac{\Phi_0}{\Phi_{epi}} \gg 1$ equation (4) becomes:

$$\hat{\sigma} = \sigma_0 [g_w + \frac{\Phi_{epi}}{\Phi_0} \left(\frac{2}{\sqrt{\pi}} \frac{I - 0{,}45\sigma_0}{\sigma_0} \right)]$$

The reaction rate *per nuclei of* Y is given by $R = \Phi_0 \hat{\sigma}$, which means:

$$R = \Phi_0 g_w \sigma_0 + \Phi_{epi} \frac{2}{\sqrt{\pi}} (I - 0{,}45\sigma_0)$$

The first parcel of R refers to thermal neutrons, the second to epithermal. Taking the first parcel and (4) one arrives at the specific activity for thermal neutrons, according to the Wescott formalism:

$$A_{esp,th} = 0{,}602 \frac{1}{M} \theta_X \Phi_0 \sigma_0 g_w P. (1 - e^{\frac{-0{,}693 t_{irr}}{T}}) \qquad (5)$$

and taking the second parcel, the specific activity for epithermal neutrons according to the Wescott formalism:

$$A_{esp,epi} = 0{,}602\frac{1}{M}\theta_X\Phi_{epi}(G_{res}I - 0{,}45\sigma_0).(1 - e^{\frac{-0{,}693t_{irr}}{T}})$$

with G_{res} being the self-protection factor of the activation cross section resonance of Y, and θ_x the natural abundance of the target nuclide.

In the case of the RPI's positions 55 and 57 where the four AgCl samples in this thesis experiment were irradiated, only equation (5) was used in the calculations shown in the next pages, as the thermal neutron flux is much higher than the epithermal flux. Also in the case of the present calculations, P can be considered to be 1 as the low density AgCl powder will not cause significant neutron flux attenuation, nor will the 5 mg gold foils. So, in practical terms, the only contribution of the wescott formalism to the RPI irradiations calculation is the Wescott factor, g_w, which is 1,005 for both the ^{197}Au(n,γ)^{198}Au and ^{109}Ag(n,γ)^{110m}Ag nuclear reactions [21].

6.5.2 Sample irradiation

In table 6.3, several irradiation parameters (irradiation time, neutron flux and sample weight and final expected activity for the each of the elements of the sample) for the different samples are shown. The presented activities are calculated values, using equation (5).

Sample Nr.	mass (mg)	Irradiation Time (s)	Neutron flux ($cm^{-2}s^{-1}$)	A(^{36}Cl) (Bq)	A(^{110m}Ag) (Bq)
1	29.3	10020	1E+13	29.7	3.88E+05
2	75	1020	1E+13	7.75	1.01E+05
3	157	3180	3.13E+11	1.58	2.07E+04

Table 6.3: Calculated irradiation time and neutron fluxes and predicted activities resulting from the activation of the ^{35}Cl and ^{109}Ag content in the samples.

The smaller weight of the two first samples was due to security restrictions, as the silver content in the samples produced levels of activity close to the maximum permitted by safety regulations.

After the irradiations, the three samples and the corresponding three gold monitors were taken to the LATR lab so that its gamma activity could be measured. The gamma radiation was measured using a HPGe detector. A ^{152}Eu ($t_{1/2}$=13.537 a) radioactive source was used to calibrate the gamma energy spectra.

Figure 6.6 shows the gamma spectra obtained for sample number 2. The several peaks visible can be identified with the help of figure 6.7, where a partial decay scheme of ^{110m}Ag is shown.

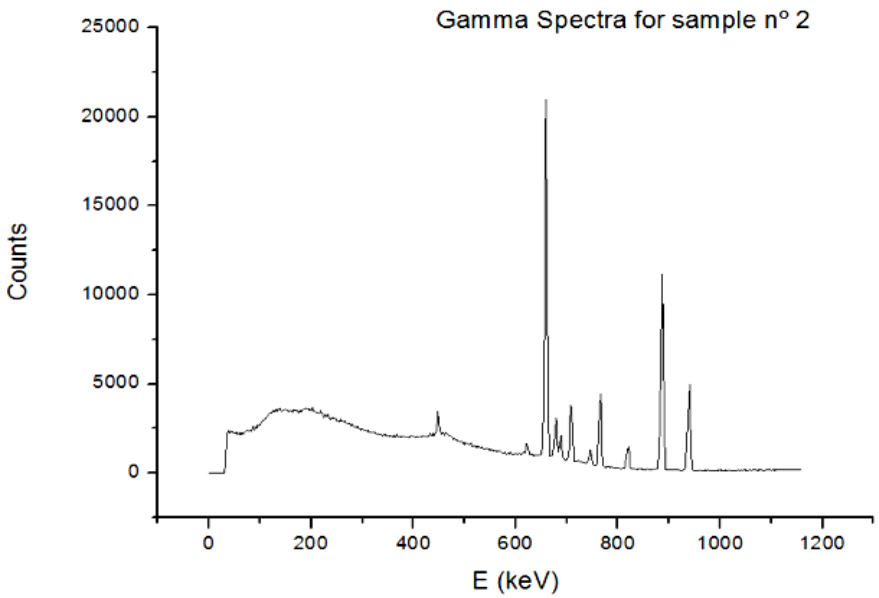

Figure 6.6: Gamma emission spectra of sample nº 2 measured with a HP Ge detector. The peak with the highest intensity is the 658 keV peak that was used in the flux monitor calculations. The other peaks can be identified with the help of figure 6.7.

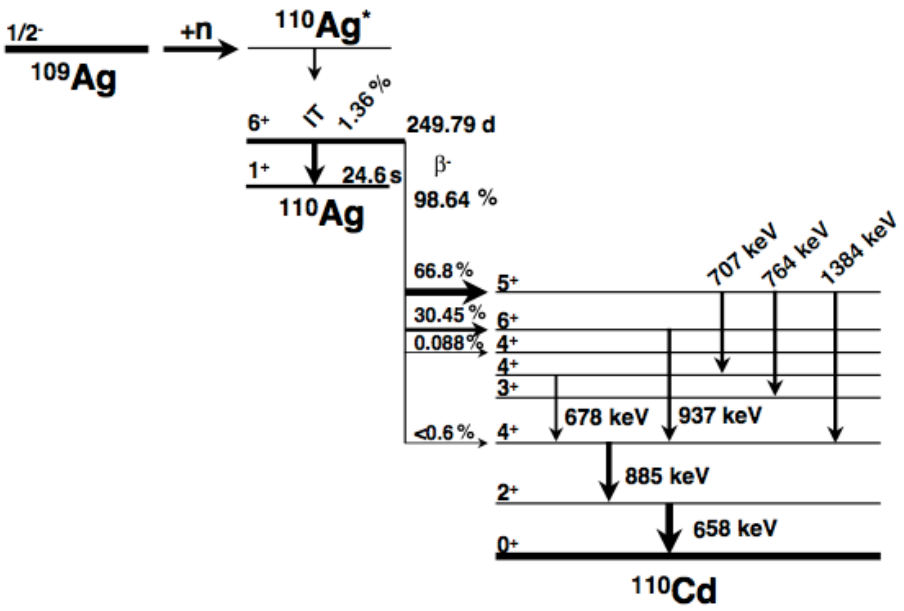

Figure 6.7: Partial decay scheme of ^{110m}Ag.

Table 2 shows the gamma measurement results for the silver content in samples 1-3.

Sample Nr.	D.T. corr.	Peak area	Y	Activity (Bq)
1	1.096	49474	225.9	1.4×10^5
2	1.025	17024	92.3	5.7×10^4
3	1.007	16176	21.3	1.32×10^4

Table 6.4: gamma measurement results: from left to right; sample number, dead time correction, area of the 658 keV gamma peak, Yield and activity in Becquerel.

Table 6.4 was constructed using the following definitions:

Dead time correction: The MCA does not analyze electronic pulses reaching it if it is occupied with the analysis of a previous pulse. Hence, there is an amount of time during which it is "dead". It implies that the number of pulses analyzed and collected is smaller than the real number of pulses. This deficit has to be corrected. One way to do it is to pass the same pulse generator signal through the detector electronics while counting it directly in an electronic counter. The pulse generator allows the choice of the correct amplitude of the signal (that will place it a position in the MCA spectra away from the region of interest so as to not interfere with the measurement data) and its frequency. The ratio between the number of counts in the counter and the area of the corresponding peak in the MCA (that is the result of the signal being processed through the same electronics as all the other measurement information) corresponds to the dead time correction.

Peak area is the number of counts in the peak corresponding to the 658 keV gamma radiation which is emitted by the ^{110m}Ag radionuclide, already corrected for background and dead time.

Yield is the peak area divided by the corresponding collection time, which translates to the number of 658 keV gammas recorded per second.

Ig is the intensity of the 658 keV gamma. The ^{110m}Ag ($t_{1/2}$=249.79 d) radionuclide de-excites to the ground state of ^{110}Ag ($t_{1/2}$=24.42 s) which in turn depopulates by β^- decay to the levels of ^{110}Cd [22]. There are several combinations of different gamma transitions by which the ^{110m}Ag nuclide can decay to the ground state of ^{110}Ag. The 658 keV gamma is the one with the highest intensity, that is, the most intense gamma line emitted in this decay. The value of the intensity for the 658 keV gamma used in this calculation was 0.9437 [22]. In the case of the 411.8 keV gamma used in the gold monitor calculations, the branching ratio used was 0.955 [22] (the gammas detected in the gamma emission spectra of ^{198}Au are shown in table 6.5 below.

Eγ (keV)	Iγ (%)
411.8	96
675.9	0.8
1087.7	0.16

Table 6.5: Gamma emissions of ^{198}Au, with respective branching ratio.

Absolute efficiency of the HPGe is the efficiency of the detector for the 658 keV gamma energy. The absolute efficiency was calculated using a ^{152}Eu radioactive source (^{152}Eu is a very useful radioactive source because it emits gammas at several energies), placed in two different positions, one close to the detector, and another at the same position of the measured AgCl and Au samples. An experimental calibration curve and a simulated one have been obtained in previous work for the close position. However, due to the high counting rate, the AgCl and Au samples had to be measured at a larger distance. In order to obtain a correcting factor, the distance coefficient, is not enough to calculate the ratios of the solid angles; the paths of gamma-rays inside the detector are very different for the two positions yielding a different intrinsic efficiency for the same gamma-line. Hence, the ratio of the absolute efficiency of the gamma-ray detector at two different positions depends on the energy of the gamma; which means that the distance coefficient is not the same for the 658 keV gamma of ^{110m}Ag and for the 411 keV gamma of ^{198}Au. This is why it is important that the radioactive source used in the calibration has a wide range of gamma energies.

For the calculation of the distance coefficient for the AgCl sample, the E_γ=779 keV was chosen, as it was close to the E_γ = 658 keV. For the gold monitors, the ^{152}Eu gamma chosen was the E_γ = 344 keV. The distance coefficient is calculated for each energy using the following :

$$C = \frac{Y(position\ 2)}{Y(position\ 1)}$$

Y is yield of the gamma peak of the energy of interest as described above. Position 1 is the closest to the detector and 2 the one further away.

Activity of the sample was calculated using the following equation:

$$A = \frac{Y(E_\gamma)}{\epsilon I_g C} \qquad (5)$$

In table 6.6 the results of the activity measurement of the gold monitors are presented:

Sample Nr.	DT Corr.	Peak area (411.8 keV)	Yield	Activity (Bq) in td
1	1.007	34909	174	1.08E+05
2	1.001	10137	24	1.54E+04
3	1.005	3920	4	2.49E+03

Table 6.6: Gamma measurement results: from left to right; sample number, dead time correction, area of the 411 keV gamma peak, Yield.

The uncertainties in the activities shown in tables 6.4 and 6.6 are in the order of 3%. By using the gold monitor data, and comparing the activity calculated using the gamma measurement information with the one calculated using the Wescott formalism for thermal neutrons, it is possible to determine the real neutron flux ϕ_R:

$$\phi_R = \frac{A_{tirr}}{N(^{197}Au)\sigma_0 g_w(1 - e^{-\lambda t_{irr}})}$$

where A_{tirr} is the activity of the gold monitor related to the gamma emission of energy E = 411 keV, by the radionuclide ^{198}Au, at t_{irr}, that is, at the time of the end of the irradiation. It is related to the activity, A_{tgm} , calculated using equation (5), that is the activity of the sample at the time of the gamma emission measurement (about two days after the end of the irradiation), by the following:

$$A_{tirr} = \frac{A_{tgm}}{e^{-\lambda t_{tmg}}}$$

In table 6.6, the results for the real neutron fluxes in each of the irradiations are shown.

Sample Nr.	Neutron flux ($cm^{-2}s^{-1}$)	$^{36}Cl/^{35}Cl$
1	(4.8±0.1)E+12	(2.13±0.06)E-06
2	(6.6±0.2)E+12	(2.95±0.08)E-07
3	(2.74±0.08)E+11	(3.8±0.1)E-08

Table 6.7: Real neutron fluxes calculated using the information gathered from the gold monitor and shown in table 3, and corresponding "real" isotopic ratios present in the samples.

Table 6.7 shows the real neutron fluxes calculated using the gold monitor data. The data of the silver content in the sample also confirms these results although there are some variations in the published σ_0 for the $^{109}Ag(n,\gamma)^{110m}Ag$ nuclear reaction which makes the silver results less reliable than the gold monitor results [22]. With the real flux values for each samples determined by its gold monitors, it is easy to predict the amount of ^{36}Cl in each sample. These values are shown in table 6.7 as well. These values were determined using the value of σ_0 = 43,89 b for the thermal capture cross section of the $^{35}Cl(n,\gamma)^{36}Cl$ nuclear reaction taken from the ENDF/B-VII.1 library that was also used to make figure 6.5.

The isotopic ratios in table 6.7 will then be compared with the ones present in the standard samples that were described in the section 5.4.2 of this chapter.

The results of this comparison will be used to test the quality of the chlorine measurements of the system. These measurements will be described in the next section.

6.6 Measurements

The chlorine beams are setup using the computer control program, already described in chapter 2. During system setup, a blank AgCl sample is used in order to minimize chamber contamination and the subsequent memory effect. The micro-beam control parameters are setup in order to maximize primary beam current at the cost of higher beam diameter; the collimator revolver is put in a position with no collimator, and the primary einzel lens is setup so as to maximize the chlorine beam intensity. This is done because, in this case, the $^{36}Cl/^{35}Cl$ isotopic ratio is in principle constant throughout the whole sample, whether the sample is an irradiated sample or a standard. Therefore there is no real gain in having a very focused, micrometer diameter beam. On the other hand, a wider and more intense primary beam will produce a more intense secondary beam. The resulting higher intensities of the produced chlorine beams will improve the detection limits, and the overall precision of the measurement; higher beams result in higher count rates in the detector, and therefore the possibility of having shorter time windows per cycle in each measurement (while keeping a good statistical precision), which directly results in higher precision of the measurement. Also, higher count rate means that it is possible to measure samples with lower ^{36}Cl content within a reasonable timespan. Having stated the above, it is nonetheless important to refer that there are additional advantages to having the possibility of a smaller beam, as opposed to the traditional macro AMS beam; the still much smaller diameter of the beam will hit only the sample area and not parts of the sample holder as is the case in AMS, which is an advantage in terms of keeping sample holder contamination at a minimum. Also, the micro-beam (even if only in the sub-millimeter range) will still be useful in checking the homogeneity of samples, even in terms of the ^{36}Cl content.

In a regular measurement day, the ionizer is heated first to around 900ºC, while keeping the air refrigeration system running (besides the oil refrigeration system which is on during the whole measurement) to keep the reservoir at a low temperature. This is done to remove all cesium that still remains from the

last session in the ionizer, before injecting new one from the reservoir. The reservoir is then heated to around 200 ºC.

After the heating of the ion source, the beam parameters from last session are loaded into the control program. After this, the magnet current is set at 13.4 A, and a Scan LE Bouncer is performed, which is a program than plots the beam intensity (at this stage the current is measured in the LE FC) vs the voltage applied to the magnet beam box (see Bouncer system in chapter 3). The two stable chlorine isotope peaks will immediately appear in the plot. Figure 6.7 shows a LE Bouncer scan where the two chlorine peaks, $^{35}Cl^-$ and $^{37}Cl^-$ are shown. By setting the bouncer for the $^{35}Cl^-$ to go through the magnet, all the beam parameters before the LE FC are finely tuned, which will usually result in a large increase in both peaks intensities. As can be seen in the figures below, the $^{35}Cl^-$ peak intensity increased from 600 pA to 2,6 nA, after the fine tune was performed (which includes, as shown in chapter 3, all the chamber parameters plus the LE ESA and LE Object steerer Y). This is about the usual current for the ^{35}Cl beam at the present time, although efforts should be made in the future to increase this current since, as mentioned before, it impacts the detection limits and precision obtainable with the system (a great part of the effort put into the work on this thesis was to extract as much current as possible from the ion source).

It is important that all the other targets, besides the blank target, produce similar beam intensities, as this can affect the measured final isotopic ratio. Keeping with what was stated in chapter 4, in order to use standards in a measurement, all the conditions of measurement have to be exactly the same for standard and unknown sample.

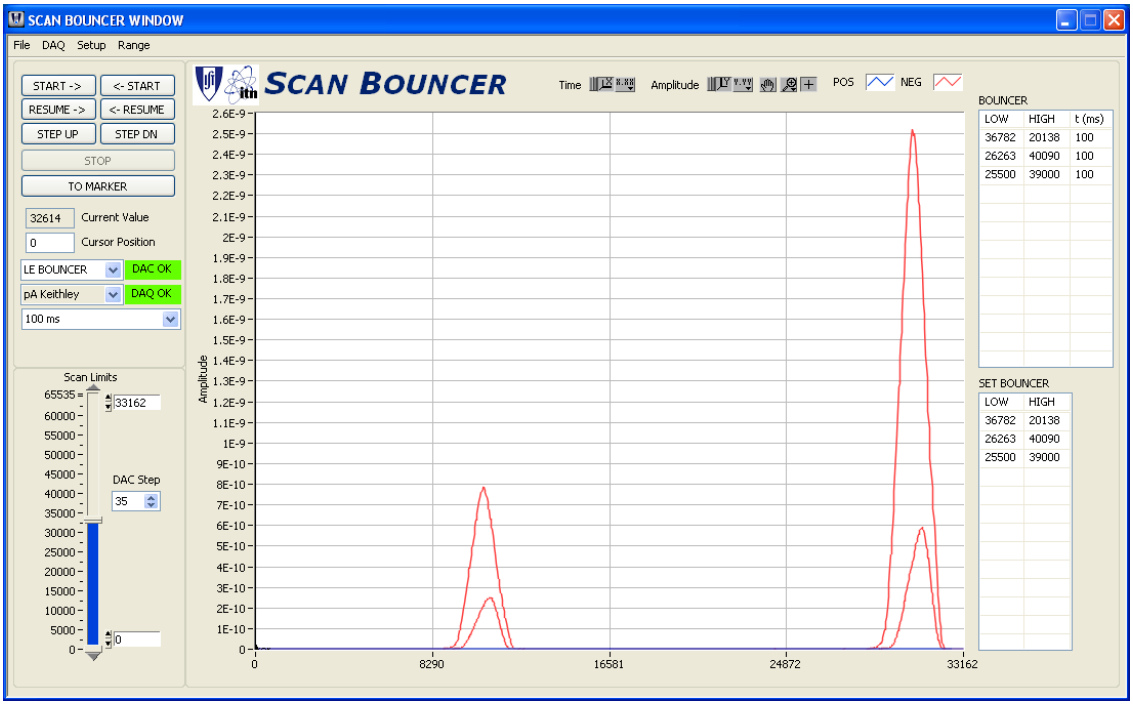

Figure 6.8: LE BOUNCER SCAN in the LE FC. This figure shows the $^{37}Cl^-$ and $^{35}Cl^-$ peaks (by this order) appearing immediately after the source heating is complete and using the beam parameters saved from last session, and using a blank sample. In each peak there are really two peaks. The higher intensity peaks shown correspond to the intensities achieved after optimization of the beam parameters before the LE magnet. As can be seen, there is a gain in terms of intensity (600 pA to 2.6 nA in the case of $^{35}Cl^-$) in both peaks. It is also visible that the relative intensity of the two peaks remains the same in both scans and corresponds to their natural abundances in the sample.

After the setting up of the beam in the LE FC, one of the beams is injected into the accelerator. By doing a magnetic field scan in the HE magnet vs beam intensity measured in the HE magnet FC, it is possible so see the different charge states that constitute the beam after the stripper channel, since particles with different charge states will be deflected along different paths in the magnetic field; lower charge states will be much less deflected than higher charge states, for the same magnetic field. This is clearly visible in figure 6.9, where one of this magnet field scans is shown.

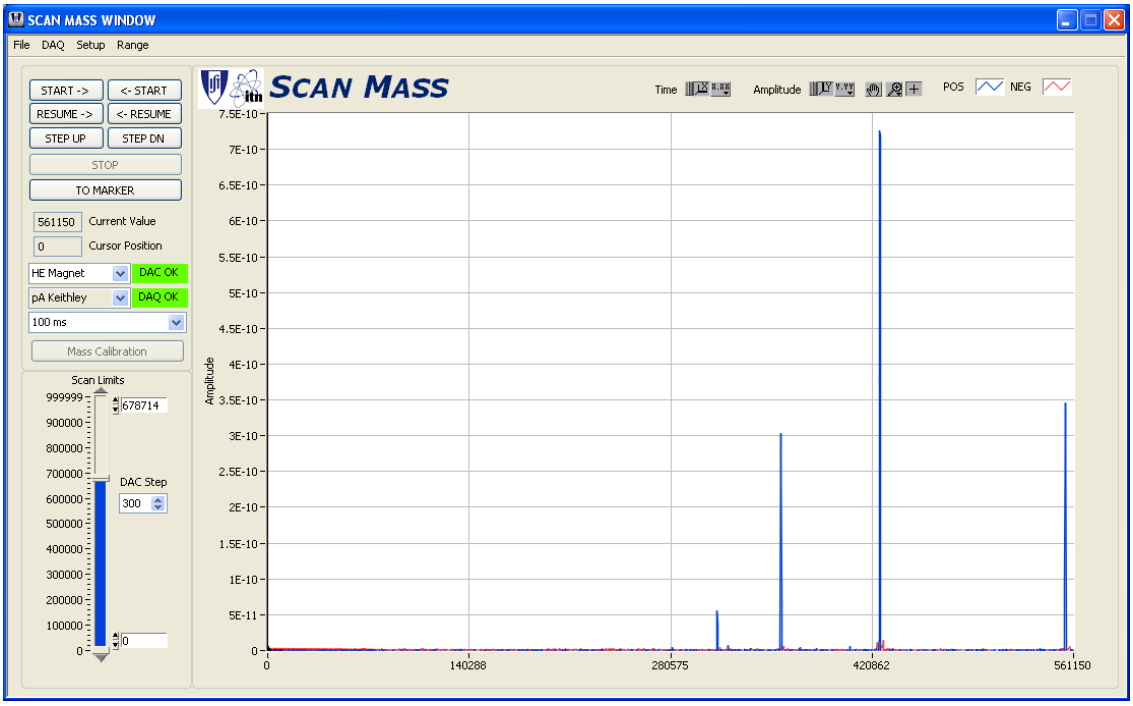

Figure 6.9: The injected beam is $^{35}Cl^{-}$, and the peaks here represented are respectively, $^{35}Cl^{2+}$, $^{35}Cl^{3+}$, $^{35}Cl^{4+}$ and $^{35}Cl^{5+}$ ions, measured at the on-axis FC after the HE magnet. The yy axis is in Ampere, the xx axis is in DAC values that correspond to magnetic field.

It is well known that the ionization efficiency has a dependence on the terminal voltage of the accelerator [16]. In figure 6.10 the different intensities of the peaks corresponding to the different charge states of ^{35}Cl after the HE magnet, are shown, for different accelerator terminal voltages. The ionization efficiency is also dependent on the stripper gas pressure. Unfortunately, there is not a great deal of range in the stripper control of the LATR tandem accelerator. From the experience gathered in this work, by the several stripper tests effectuated, the increase of pressure in the stripper channel invariably resulted in lower beams after the accelerator, independently of the charge state. This was not expected. The best explanation seems to be related to the stripper pumping system being disabled.

The tandem accelerator stripper system is equipped with a turbo pump that is supposed to help control the pressure of the gas in the stripper channel. Without it functioning, and having no way to measure the pressure directly in the tube, it is impossible to tune the stripper pressure efficiently. As it is, the

residual gas in the stripper channel seems to be the best pressure in terms of maximizing the transmission, and this pressure is the one used in all the work shown in this thesis.

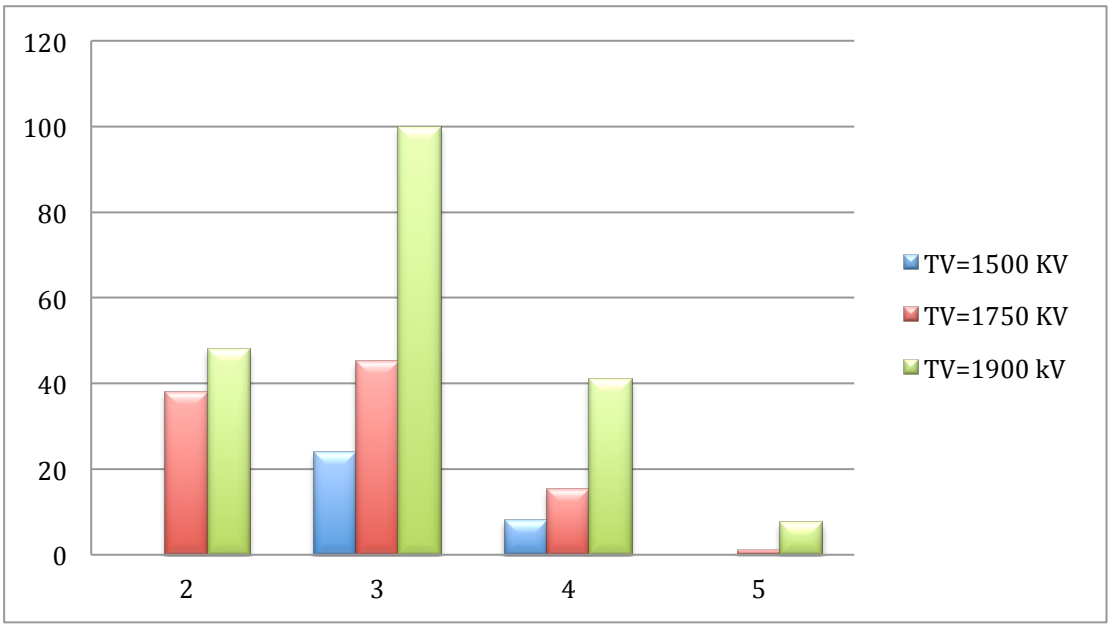

Figure 6.10: Charge state distribution dependence on terminal voltage of the accelerator for the same stripper gas pressure. The yy axis scale is in relative intensity and the xx axis represents the different charge states. The injected beam is $^{35}Cl^{-}$, and the relative intensities represented are a normalization of the currents of, respectively, $^{35}Cl^{2+}$, $^{35}Cl^{35}$, $^{35}Cl^{4+}$ and $^{35}Cl^{5+}$ ions, measured at the on-axis FC after the HE magnet.

The terminal voltage in the accelerator is usually set at 1.9 MV. This terminal voltage in the accelerator was chosen because no isobaric separation would be performed in the ionization chamber, as explained before. If separation was needed, a terminal voltage of at least 3 MV would be necessary along with a solid stripper [15].

Without the requirement of isobar separation, an even lower terminal voltage (than 1.9 MV) in the accelerator could be used in principle. However, as can be understood by figure 6.10, with higher terminal voltage, it is possible to achieve higher beam intensities in higher charge states.

In the case of the present work, charge 4+ was used. This choice seems to go against what is shown in figure 6.10, where it is clearly visible that the charge state 3+ is the most intense for every terminal voltage shown. The reason why charge state 3+ was not chosen was that when the beam transport conditions are set for it, a very intense peak will show up at the detector spectra. This peak corresponds to $^{18}O_2^{3+}$ molecules that can survive the stripper channel.

The reason for this choice was a compromise between the avoidance of lower charges states and a good transmission through the accelerator, as lower charge states may still be contaminated with unbroken molecules that may have survived the stripper channel. So the choice of terminal voltage is a compromise between getting a good transmission through the accelerator and therefore maximizing the current reaching the detector and the additional time per measurement that the conditioning of the accelerator takes, since higher terminal voltages require more time to set up the accelerator.

The choice of charge state 4+ and terminal voltage of 1.9 MV means that the beam entering the detector has an energy of 9.5 MeV.

After the $^{35}Cl^{4+}$ ion is chosen in the faraday cup after the HE magnet, this beam is used to setup the HE ESA's, using the FC inside the detector chamber. After this, a standard sample with a low ^{36}Cl content is put in front of the primary beam. After switching the detector chamber FC for the particle detector, and setting the LE and HE bouncer system for $^{36}Cl^-$ and $^{36}Cl^{4+}$ respectively, this beam will be used to fine tune the whole high energy beam transport system again. While injecting $^{36}Cl^-$ it is possible to measure simultaneously the $^{35}Cl^-$ and $^{37}Cl^-$ beams at the LE off-axis FCs described before. If the isotopic ratio of these isotopes is as expected, the $^{35}Cl^-$ beam will be injected and the HE bouncer will be scanned in the off-axis HE FC. The DAC value corresponding to the $^{35}Cl^{4+}$ peak will be stored in the Scan bouncer program along with the DAC values for the three peaks in the LE Bouncing system and the HE bouncing system. These values will then be loaded into the AMS program. In this program, the time per cycle and run will be chosen.

A cycle is subdivided into three sub-cycles, each with a time of 100 ms. In each of this cycles, the currents of $^{35}Cl^{4+}$, $^{36}Cl^{4+}$and $^{37}Cl^{4+}$ are measured. Usually

the number of cycles is around 1000, but it depends on the precision required. The AMS program will register the number of counts in each run for each of the isotopes (it automatically converts the currents measured in the FCs into number of particles) and produce a .txt file with these values.

Since a target holder takes four samples at a time (two unknown samples, a standard and a blank), these are measured alternately several times. The blank is useful to measure the background in the 36 mass channel. The count rate in the 36 channel is measured initially before the other samples are measured. This sets the detection limit. After this first measurement, the blank is useful to measure the memory effect after each of the samples containing ^{36}Cl is measured. After the count rate in channel 36 in the blank falls to the initial blank value, the next sample can be measured.

Special steps are taken to assure that the currents of the $^{35}Cl^-$ and $^{37}Cl^-$ in the LE FC are the same as the sample measured before, before proceeding to the measurement itself. It is important to assure this, because different beam intensities for different samples can result in different beam paths and therefore results that are not comparable. This is also true, as was mentioned before, for the sample surface and its position relative to the primary beam. In order to have reproducibility it is important that these conditions are met.

The txt file produced by the Scan AMS program will provide the count rate for each isotope in each cycle. Figure 6.11 and figure 6.12 shows plots of the information provided by the computer program after a measurement performed on a standard sample in figure 6.11 and on an irradiated sample in figure 6.12. It can be seen that there were some fluctuations in the beam intensity throughout the measurement but these fluctuations disappear in the isotopic ratio. These is only possible if the fluctuations affect both beams (^{35}Cl and ^{36}Cl) equally and this is only possible due to the fast switching of beams made possible by the bouncing system.

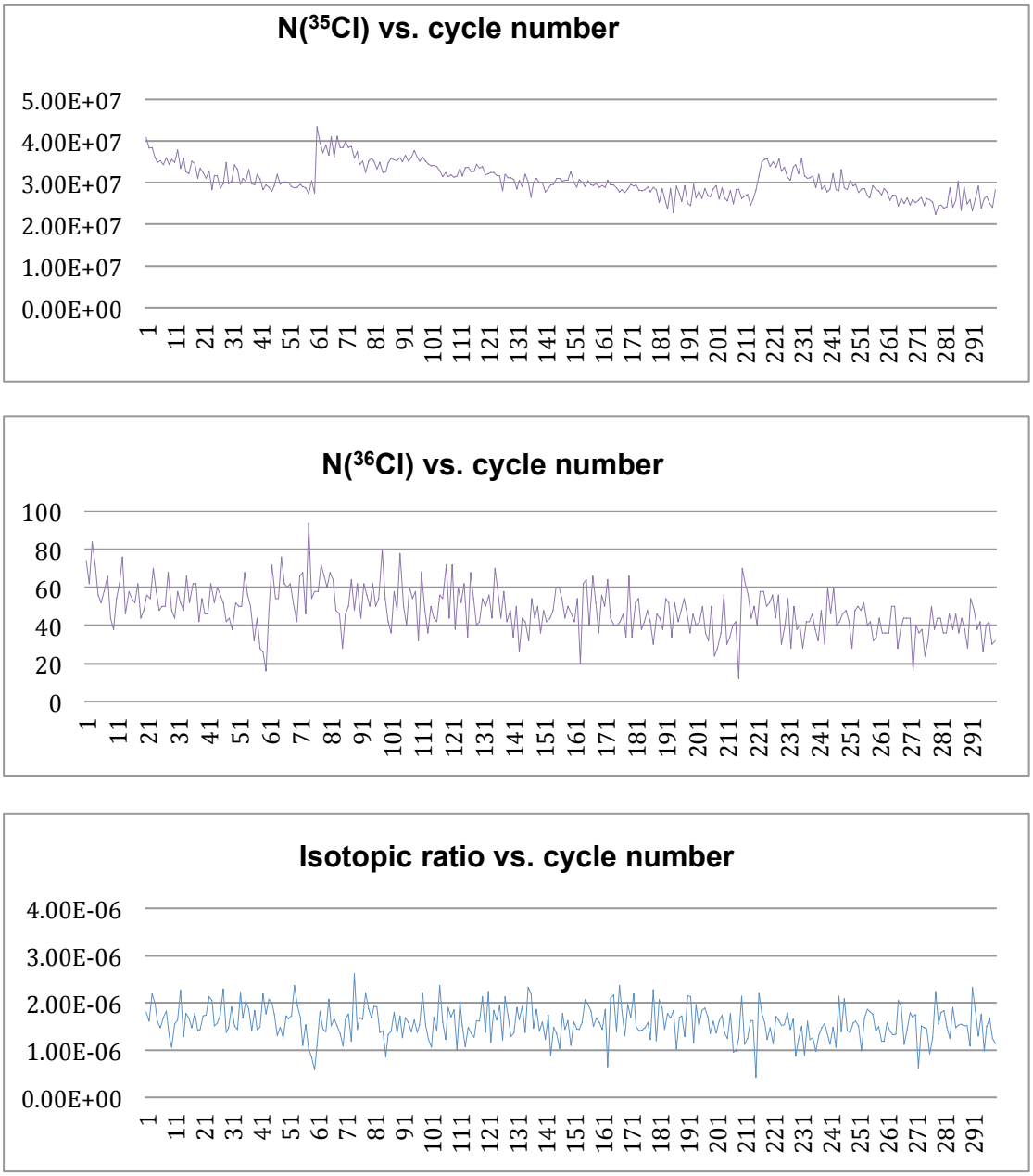

Figure 6.11: The three plots show the progression of a measurement of a standard AgCl target. Each of the cycles represents a 100 ms measurement time for each of the isotopes. In this particular measurement, the beam was not as stable as desired, as can be seen by the beam current increase around cycles 60 and 215, but still this variation in the beam intensity (related to some instability in the beam transport system or the ion source) did not affect the isotopic ratio due to the bouncing system.

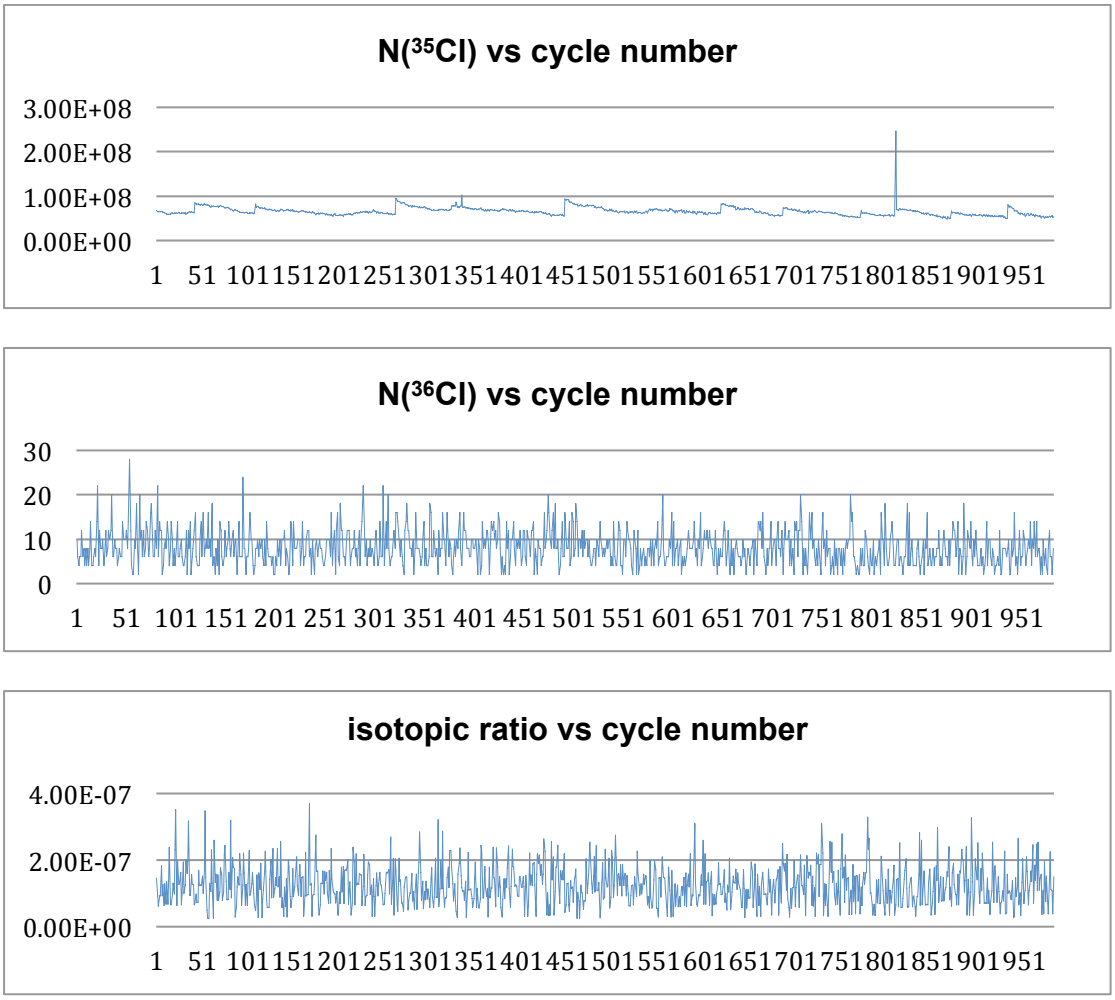

Figure 6.12: Same three plots as shown in the previous figure but for an irradiated sample with an isotopic ratio lower by about one order of magnitude.

The data collected by the computer will, as can be seen by the previous figures, provides the number of counts of ^{35}Cl and ^{36}Cl for each cycle. It is then necessary to calculate the final isotopic ratio value, which is an average of these values.

The mean values $\bar{x}$ will be calculated using the following:

$$\bar{x} = \frac{\sum_i \frac{x_i}{\sigma_i^2}}{\sum_i \frac{1}{\sigma_i^2}} \qquad \sigma_{int\bar{x}} = \frac{1}{\sqrt{\sum_i \frac{1}{\sigma_i^2}}} \qquad \sigma_{ext\bar{x}} = \sqrt{\frac{\sum_i \frac{(x_i - \bar{x})^2}{\sigma_i^2}}{(N-1).\sum_i \frac{1}{\sigma_i^2}}}$$

(6)

where σ_i is the individual uncertainty, that is, the statistical uncertainty of each value. The uncertainty of the weighted mean value $\sigma_{\bar{x}}$ is the maximum of the internal and external uncertainty. Having the mean value for $N(^{36}Cl)$ and $N(^{35}Cl)$ it is possible to calculate the isotopic ratio and its uncertainty using the propagation of errors formalism. Each of the isotopic ratios has then to be normalized to the isotopic ratio measured from the standard, as shown in chapter 4.

6.7 Results

The bulk of the measurements were performed on irradiated samples prepared with isotopic ratios in the 10^{-6} and 10^{-7} range, and only the results pertaining to sample number 2 are shown as this was the sample that was more consistently measured. The high content of ^{36}Cl in this sample made it easier to tune the system. The standards used in these measurements were prepared to have an isotopic ratio of $^{36}Cl/^{35}Cl = 1 \times 10^{-6}$.

Figure 6.13 shows three different normalized measurements on the same sample, sample number 2 as identified in table 6.7 (each of the measurements was succeeded by a standard measurement which was used for normalization); the first two in the same day but with somewhat different beam tunings and the last, two days after the first two. The largest error bar is in the 4% range.

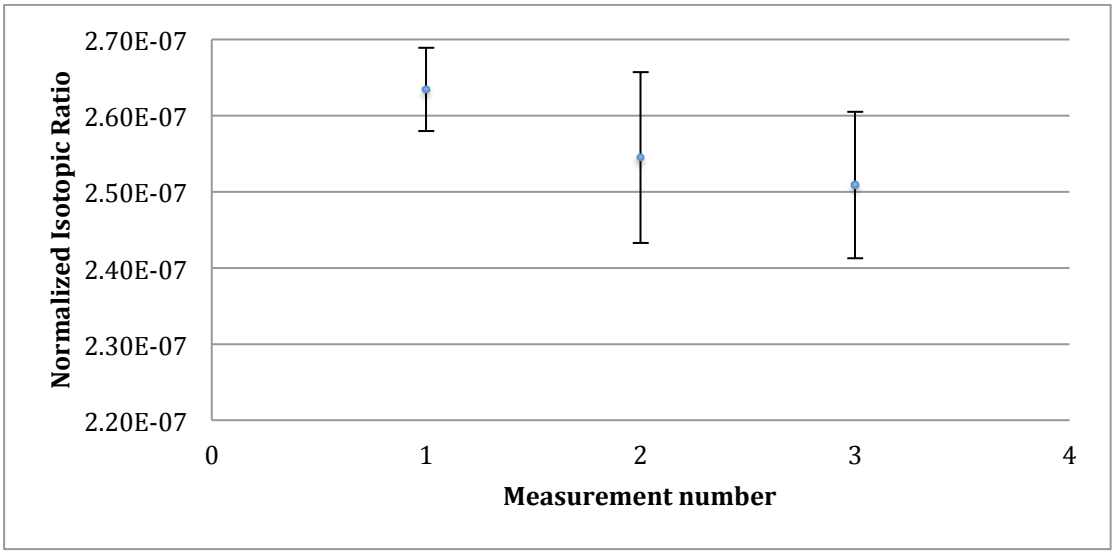

Figure 6.13: Isotopic ratios of an irradiated sample, sample number 2, normalized for the diluted standard. Measurement number 1 and 2 were performed on the same day. Measurement number 3 was performed two days later.

Using the three measurements shown in table 6.13, and applying (6), the mean value for the final isotopic ratio is:

$I_{Rsample2}$ ($^{36}Cl/^{35}Cl$)= (2.59 ± 0.04) x 10^{-7}

With this value it is possible to calculate the thermal neutron capture cross section for the $^{35}Cl(n,\gamma)^{36}Cl$ nuclear reaction, using the following:

$$\sigma_0 = \frac{I_{R.}}{\phi_R t_{irr}}$$

using the values of the real neutron flux calculated for sample 2 as well as its irradiation time, which yields the following result:

$$\sigma_0 = 39 \pm 1 \text{ b}$$

6.8 Discussion of results

Figure 6.13 shows the results for isotopic ratios measured for the same sample in two different days. They show a good reproducibility, which is an important result if the system's complexity is taken into account.

The value of $\sigma_0 = 39 \pm 1$ b for the $^{35}Cl(n,\gamma)^{36}Cl$ nuclear reaction is about 10% below the published value of $\sigma_0 = 43.55$ [23]. This discrepancy is reasonable.

It is important to refer that the real flux during this irradiation was calculated using the very well known $\sigma_0 = 98.8$ b [22] for the $^{197}Au(n,\gamma)^{198}Au$ reaction. The reason for using only the thermal neutron contribution had to do with the fact that, as can be seen by viewing figure 6.4 and 6.5 together, the contribution of the thermal neutrons is much larger than the rest of the neutron spectra. Nonetheless, steps are being taken to have an additional Cd monitor so that the contribution by the rest of the neutron spectra can be taken into account, when calculating the real neutron flux.

It would be important to have results, in terms of isotopic ratios, for samples number 1 and 3, however, it was not possible to measure the other two samples shown in table 6.6 due to technical problems with the ion source. It would be important also to have a good agreement between different samples with different amounts of ^{36}Cl. The work will be resumed as soon as the source is in operation.

The results confirm the neutron irradiation process as a valuable method for the production of standards, as well as the chemical procedures used for the production of standards and blank material. The production of ^{36}Cl standards in the CTN-IST nuclear reactor is an important step for the ^{36}Cl AMS for the CTN-IST laboratory as it reduces the price of the production of standards considerably.

However, the precision of the measurements (around 4%) is still not as good as expected. This is a problem as the goal of the future work (measuring of nuclear reactions producing ^{36}Cl using the CTN-IST Micro-AMS system) is to measure samples with less ^{36}Cl than the ones measured so far, which means an

even lower precision, as less ^{36}Cl means less counts per second in the particle detector. In order to achieve a better precision, steps are being taken to increase the primary beam intensity as well as decreasing the measurement cycle time, especially for the ^{35}Cl and ^{37}Cl beams, by connecting the Faraday cups to a faster current integrator.

References

[1] M. Gounelle New Astronomy Reviews 50 596–599 (2006)

[2] M. Chaussidon, M. Gounelle, C. R. Geoscience 339 (2007)

[3] Amelin et al. Earth and Planetary Science Letters, 300, 343 (2010)

[4] Bouvier, Wadhwa, Nature Geoscience, 3, 637 (2010)

[5] Jeffrey, Reynolds , J. Geophys. Res. **66**, 3582 3 (1961)

[6] M. Gounelle, EAS Publications Series, Vol. 51, (2011)

[7] M. Gounelle, A. Meibom, The Astrophysical Journal, 680:781–792, (2008)

[8] N. Dauphas and M. Chaussidon. Annu. Rev. Earth Planet. Sci. 39:351–86 (2011)

[9] A. Cameron, J. Truran, Icarus, 30, 447 (1977)

[10] Ouellette et al., San Francisco: ASP Conference Series 527 (2005)

[11] M. Gounelle, Les meteorites (2009)

[12] Jacobsen B et al. Proc. Lunar Planet. Sci. Conf., 40th, The Woodlands, Tex., 2553. Houston: Lunar Planet. Inst. (2009)

[13] Shu et al., The Astrophysical Journal, 548:1029È1050, (2001)

[14] J. V. Cizdziel et al, Journal of Radioanalytical and Nuclear Chemistry, Vol. 275, No.1 133–144 (2008)

[15] P. Steier et al. Nuclear Instruments and Methods in Physics Research B 268 744–747 (2010)

[16] P. Steier et al. Nuclear Instruments and Methods in Physics Research B 240 445–451 (2005)

[17] M. Martschini, Dissertation Thesis, Vienna (2012)

[18] Yuki Tosaki et al, *Water 3*, 64-78 (2011)

[19] A.C. Fernandes et al., Annals of Nuclear Energy 37 1139–1145 (2010)

[20] E. Moutinho, Activação de amostras nucleares CTN-ITN 1995

[21] Database of prompt gamma rays for slow neutron capture for elemental analysis, International Atomic Energy Agency, Vienna 2006

[22] S. Nakamura, Journal of Nuclear Science and Technology, Vol. 40, No. 3, p. 119–124 (2003)

[23] S.F. Mughabghab IAEA (2003)

7

Conclusions

In order to reach the final goal of this thesis (the measurement of Astrophysically relevant reactions using AMS) several obstacles had to be overcome due mainly to three reasons; a system that was not operating at full potential when it was installed, lack of experience with AMS of all involved in the process (which includes a lack of sample preparation skills and laboratorial conditions for the preparation of AMS standards, blanks and samples) and sometimes the unavailability of funds to readily substitute or upgrade damaged or obsolete parts, due to the high costs involved in some of the parts of the system.

However, the lack of means and experience that most top AMS laboratories in the world take for granted, forced the intervenients in this work to sometimes resolve problems with a more involved and hands-on approach, which inevitably lead to a better and more profound knowledge of the problems resolved and in the end a better understanding of the system.

As such, it is possible to affirm that, at the end of the process within which the present work was developed, the CTN-IST laboratory has a fully operational Micro-AMS system, tested with several different kinds of isotopes and samples, which allow it to be applied to a number of important applications relevant to several research groups developing work inside and outside the laboratory. It has also the possibility and know-how to produce

samples for AMS, namely for chlorine AMS. This represents a valuable addition to the CTN-IST laboratory and work is being developed to broaden the domain of applications of this system within the context of the laboratory, namely in terms of biomedical applications using iodine and calcium isotopes.

In terms of the Astrophysical goals, and taking into account the ongoing research project, funded by FCT, related to ^{36}Cl measurements, the work developed in this thesis established the technical basis, indicated below, that will permit the development of the goals advanced of that project. It was however impossible to include the more recent developments of these measurements in this thesis due to academic time limitations.

The technical basis referred above include:

- the system for very low isotopic ratio measurements ($<10^{-5}$), comprising the off-axis Faraday cups in the LE energy and HE sides, which performed as expected, allowing the simultaneous counting of ^{35}Cl and ^{36}Cl;
- the adaptations to the sample holder and sample mounting techniques, which led to a very important reduction of the ^{36}S background;
- the modifications of the computer control system, with consequent uncertainty decrease of the detected isotopic ratio;
- The acquired skills of standard and sample production that together with mastering the neutron irradiation technique translated into good reproducibility of the measuring techniques.

This thesis showed also the very good performance of the CTN-IST micro-AMS system in the determination of ratios related to isotopes of heavy elements as Pt and Pb.

References

Chapter 2

[1] Herzog, R. F. K., Viehboeck, F (1949). *Phys. Rev.* **76** (6): 855–856

[2] Honig, R. E. (1958). *J. Appl. Phys.* **29**: 549-555.

[3] Liebl, H. J (1967). *J. Appl. Phys.* **38** (13): 5277–5280

[4] Castaing, R. & Slodzian, G. J (1962). *Microscopie* **1**: 395–399.

[5] Magee, C. W. et al. (1978). *Rev. Scient. Instrum.* **49** (4): 477–485

[6] Benninghoven, A (1969). *Physica Status Solidi* **34** (2): K169–171.

[7] Honig, R. E. International Journal of Mass Spectrometry and Ion Processes Volume 66, Issue 1, 25 June 1985, Pages 31–54

[8] Alvarez L.W., Cornog R. Phys. Rev. 56, 613–613 (1939)

[9] Muller, R. A. (1977). Science **196** (4289): 489–494.

[10] Bennett C L, Beukens R P, Clover M R, Gove H E, Liebert R B, Litherland A E, Purser K H and Sondheim W E 1977

[11] Nelson D E, Korteling R G and Stott W R, 1977 Science 198 507

[12] Raisbeck, G. M.; Yiou; [et al.] Nature 1978

[13] Raisbeck, G. M.; Yiou, F.; Klein, J.; [et al.] Nature (1983)

[14] Elmore, D.; Fulton, B. R.; Clover, M. R.; Marsden, J. R.; Gove, H. E. Nature, Volume 277, Issue 5691, pp. 22-25 (1979).

[15] D. Elmore, H. E. GOVE et al. *Nature* 286, 138 - 140 (10 July 1980)

[16] Hotchkisa M. et al, Applied Radiation and Isotopes Volume 53, Issues 1–2, 15 July 2000, Pages 31–37

[17] Synal H.A. et al Nuclear Instruments and Methods in Physics Research Section B: Beam Interactions with Materials and Atoms Volume 259, Issue 1, June 2007, Pages 7–13

[18] Litherland A.E., Annual Review of Nuclear and Particle Science Vol. 30: 437-473 (December 1980)

[19] Akhmadaliev et al. ,Nuclear Instruments and Methods in Physics Research Section B 294 (2013) 5–10

[20] Hajdasa et al. , Nuclear Instruments and Methods in Physics Research Section B: Beam Interactions with Materials and Atoms, Volumes 223–224, August 2004, Pages 267–271

[21] Purser, K.H., 1977. U.S. Patent 4037100.

[22] Rucklidge, J.C., M.P. Gorton, G.C. Wilson, L.R. Kilius, A.E. Litherland, D. Elmore, and H.E. Gove, 1982. Canadian Mineralogist 20: 111-119.

[23] Matteson, S., J.L. Duggan, D. Marble, F.D. McDaniel, D.L. Weathers, D.K. Wilson, J.M. Anthony, and R.L. Beavers, 1990, Nucl. Instr. and Meth. B 52: 327-333.

[24] Sie, S. H.; Niklaus, T. R.; Suter, G. F. Nuclear Instruments and Methods in Physics Research Section B, v. 123, p. 112-121.

[25] Maden C., dissertation Swiss Federal Institute of Technnology, 2003

Chapter 3

[1] S.H. Sie , T.R. Niklaus, G.F. Suter , Nuclear Instruments and Methods in Physics Research B 123 (1997) 558-565

[2] S.H. Sie et al, Review of Scientific instruments Vol. 69, 3 1997

[3] S.H. Sie , T.R. Niklaus, G.F. Suter, Nuclear Instruments and Methods in Physics Research B 123 (1997) 112- I21

[4] Cockcroft, J.D. and Walton, E.T.S. (1932). Proc. R. Soc. London **A137**:229

[5] P. Steier et al., Nuclear Instruments and Methods in Physics Research B 240 (2005) 445–451

[6] G. Amsel, E. D'Artemare and E. Girard, Nucl. Instr. Meth. 205 (1983)5.

Chapter 4

[1] P. Sigmund, (2006). Particle penetration and radiation effects, Springer Series in Solid-State Sci-

ences, Vol. 151 (Springer, Berlin).

[2] P.Sigmund, PSP Review Volume 2011

[3] Benninghoven, A., F.G. Rüdenauer, and H.W. Werner, 1989. "Secondary Ion Mass Spectrometry", John Wiley & Sons.

[4] K. Wittmaack, Surface Science Volume 90, Issue 2, 2 December 1979, Pages 557–563

[5] N. Nieuwjaer et al., Surface and Interface Analysis Volume 41, Issue 1, pages 6–10, January 2009

[6] Deline, V.R., C.A. Evans, and P. Williams, 1978. "Unified Explanation for Secondary Ion Yields." Applied Physics Letters **33**(7): 578-580.

[7] Deline, V.R., W. Katz, and C.A. Evans, 1978. "Mechanism of Sims Matrix Effect." Applied Physics Letters **33**(9): 832-835.

[8] R. Middleton, "A Negative-Ion Cookbook" revised 1990

Chapter 5

[1] J.S. Stacey, J.D. Kramers, Earth and Planetary Science Letters Volume 26, Issue 2, June 1975, Pages 207–221

[2] Gale, N. H., and Stos-Gale, Z. A., 1982, Science, 216,11–19.

[3] Cui J., WU X., Archaeometry 53, 1 (2011) 205–214

[4] Brill, R. H., and Wampler, J. W., 1967, American Journal of Archaeology, 71, 63–77.

[5] Stos-Gale et al. Archeometry, 39, 1 1997, 83-123"

[6] Gale, N. H., and Stos-Gale, Z. A., 2000, 503–84, Chemical Analyses Series 155,

[7] Yeung C.S.L. et al, Surf. Interface Anal. 29, 487–491 (2000)

[8] S.H. Sie et al. Nuclear Instruments and Methods in Physics Research B 123 (1997) 112- I21

[9] M. L. W. Thewalt et al., Physica B 401-402 (2007) 587.

[10] A. Yang et al., Physica B 401-402 (2007) 593.

[11] M. Steger et al., Phys. Rev. Lett. 100, 177402 (2008).

Chapter 6

[1] M. Gounelle New Astronomy Reviews 50 596–599 (2006)

[2] M. Chaussidon, M. Gounelle, C. R. Geoscience 339 (2007)

[3] Amelin et al. Earth and Planetary Science Letters, 300, 343 (2010)

[4] Bouvier, Wadhwa, Nature Geoscience, 3, 637 (2010)

[5] Jeffrey, Reynolds , J. Geophys. Res. **66**, 3582 3 (1961)

[6] M. Gounelle, EAS Publications Series, Vol. 51, (2011)

[7] M. Gounelle, A. Meibom, The Astrophysical Journal, 680:781–792, (2008)

[8] N. Dauphas and M. Chaussidon. Annu. Rev. Earth Planet. Sci. 39:351–86 (2011)

[9] A. Cameron, J. Truran, Icarus, 30, 447 (1977)

[10] Ouellette et al., San Francisco: ASP Conference Series 527 (2005)

[11] M. Gounelle, Les meteorites (2009)

[12] Jacobsen B et al. Proc. Lunar Planet. Sci. Conf., 40th, The Woodlands, Tex., 2553. Houston: Lunar Planet. Inst. (2009)

[13] Shu et al., The Astrophysical Journal, 548:1029È1050, (2001)

[14] J. V. Cizdziel et al, Journal of Radioanalytical and Nuclear Chemistry, Vol. 275, No.1 133–144 (2008)

[15] P. Steier et al. Nuclear Instruments and Methods in Physics Research B 268 744–747 (2010)

[16] P. Steier et al. Nuclear Instruments and Methods in Physics Research B 240 445–451 (2005)

[17] M. Martschini, Dissertation Thesis, Vienna (2012)

[18] Yuki Tosaki et al, *Water 3*, 64-78 (2011)

[19] A.C. Fernandes et al., Annals of Nuclear Energy 37 1139–1145 (2010)

[20] E. Moutinho, Activação de amostras nucleares CTN-ITN 1995

[21] Database of prompt gamma rays for slow neutron capture for elemental analysis, International Atomic Energy Agency, Vienna 2006

[22] S. Nakamura, Journal of Nuclear Science and Technology, Vol. 40, No. 3, p. 119–124 (2003